NONLINEAR SYSTEMS WITH DISCRETE AND CONTINUOUS ELEMENTS

Carsten Nordstrøm Jensen

LYNGBY 1997
ATV Industrial ph.d. project ATV 551

IMM ES-Consult

Printed by IMM, DTU

Preface

This thesis is a product of an industrial ph.d. program involving ES-Consult, The Technical University of Denmark, and the Danish Academy of Technical Sciences. The ph.d. study has taken place from autumn 1994 to autumn 1997.

During the past three years I have received inspiration from a number of persons and learned from their experience. I would like here to send my thanks to some of them.

First of all I would like to express my gratefulness to my three supervisors Eilif Svensson, Hans True and Mads Peter Sørensen.

Eilif is always ready for a discussion and is always giving inspiration. From a professional point of view, he has a great talent and experience for making a description of some physical system balance, to both contain the complexity of theoretical interest, and remain sufficiently simple to be applicable for industrial purposes.

Hans has a huge amount of background knowledge. He exhibits a passionately love for everything concerned with railways, and he always knows the right person in the right place.

I would like to thank Mads for many fruitful discussions on wave propagation. Let me also mention that when I had used up half a years of the university department admission to a super computer, for one single computation, Mads was the one pulling the chestnuts out of the fire for me.

Especially I would like to mention Per Grove Thomsen at the department of mathematical modelling. He is apparently always able to find time to help a student. He also has a remarkable skill of always being able to give a useful answer to these various student questions.

I thank Jens Christian Jensen for giving access to the computer programs he developed during his ph.d. project and for discussions in that connection.

I would also like to mention Jakob Birkedal Nielsen, who has been a very nice ph.d. student colleague.

I thank Vagn Eriksen and Jens Outtrup for showing interest for my project, for spending time for meetings with me, and for inviting me to a test run on the Great Belt connection.

I also thank Finn Jensen for inviting me on a test ride where the capabilities of the ER4 trains running at 180 km/h were tested. We also had an agreement of making pantograph experiments; unfortunately time did not permit it.

I thank Steen Gravgaard at Siemens and Stefan Ravelli at Schunk Nordiska for supplying data for me.

During the time of the ph.d. study I have been on shorter and longer stays at universities abroad. In that connection I would especially like to mention Giorgio Diana, Frederico Cheli, Steffano Bruni, Andrea Collina and colleagues for making my short stay at the Politecnico di Milano very educating and inspiring — a very nice part of the past 3 years. With Andrea Collina I have had many discussions on modelling aspects and investigation results for pantograph overhead line systems.

I thank the employees in ES-Consult for patiently haven listened to my more or less wild ideas and for haven reflected on various partial differential equations. And not to forget, I especially thank them for being able to create the nice atmosphere in the company.

Finally I thank the Danish Academy of Technical Sciences for the financial support to the project.

October 1997 Carsten Nordstrøm Jensen

Contents

Chapter 1

Introduction

‘Nonlinear dynamical systems with discrete and continuous elements’ is a very broad formulation which covers a variety of different physical systems.

Two such physical systems form the base of this thesis and the ph.d. project behind it: The dynamics of a train running on a bridge and the dynamical interactions between a pantograph and an overhead line system.

Both of these systems have great actuality for the infrastructure situation in Denmark right now.

1.1 Train bridge interactions

Train bridge interactions (and interactions between a moving mass and a continous beam in general) have been subject of investigations for more than a century. For a general introduction to the subject of train bridge interaction see [9], [8], or [10]. The railway runnability on long future suspension bridges have been treated, [40], [11], [12], or [5].

Large Bridges for road and rail traffic have been built and are being built at Great Belt between Zealand and Fune, and at Øresund between Denmark and Sweden, and a connection over Fehmern Belt between Denmark and Germany is under dawning political considerations. Besides that there are of course a number of minor bridges, for which the desire for an increase of the train speeds puts focus on the train bridge interactions.

Train bridge considerations have two different viewpoints: that of the bridge concerning bridge loads, internal stresses, dynamical amplification factors, etc.; and that of the train concerning train passenger comfort and ride quality, derailment risks, wear, etc.

The tendency of bridge design goes towards lighter and more flexible constructions. With the rapid improvements of railway technology and the increasing train speeds, the impact from a train on a bridge and vice versa will increase in the future. Our angle of the investigations differs from other investigations by the inclusion of nonlinearities in the train models. In other areas of railway dynamics, these nonlinearities are crucial.

1.2 Pantograph catenary system interactions

Pantograph/catenary interactions have been the subject of a number of investigations in the last decades. Scott and Rothman describe their early suite of computer programs for such investigations, [38]. Hobbs and Ghostling describe their lumped mass approach for modelling of the cables and show very convincing comparisons with test results, [25] and [20]. Cook compares different catenary system-pantograph combinations and lists data for the mathematical models, [7]. Kiessling et.al. describes the newest German overhead line system, the Re 330, [30]. Harprecht et.al. describes the circumstances at the test that lead to the german short lasting world speed record on rail of 406.9 km/h, [22]. [23]. Becker et.al. compares differences when the cables are modelled as strings respectively beams, [4].

Jensen et.al. treats wave propagation and nonlinearities in the modelling of overhead line systems, [26]. Eppinger et.al. points out the from the modelling point of view important difference between a symmetric and an asymmetric pantograph, [13]. Lesser et.al. points out the importance of not just modelling the pantograph as planar, [32]. A huge amount of effort has been put in developing overhead line systems and inventing pantographs with improved dynamical behaviour, for example [3]. Pantographs with some sort of active control have been considered, [18] and [36], but so far all existing pantographs are purely passive devices. Zhai and Cai consider the effect on the catenary pantograph dynamics from the vibrations of the locomotive, [46]. Poetsch et.al. has a very nice state of the art paper on pantograph/catenary dynamics as of 1997 in [36].

Obviously, pantograph catenary system interactions are more violent the higher the train speeds are. With the recent increase of the maximal train operation speed in Denmark to 180 km/h, pantograph catenary dynamics has greater actuality in Denmark than ever before.

The danish state railways have had great success after the opening of the Great Belt connection for trains. From this has followed an expansion of the traffic load, and one way of achieving such an expansion is by using longer train sets, with increased number of pantographs. The dynamical pantograph overhead line system interactions worsen for trailing pantographs because the contact cable has already been excited by the pantograph(s) in front. Thus, also this puts focus on the subject of pantograph overhead line system interactions.

Finally the dawning international liberalisation of the railways rises a lot of new questions that will have to be addressed.

Fortunately the danish overhead line systems have been designed with a possible increase of the maximal train operation speed in mind. 180 km/h ought not be a problem by itself. However, increasing at the same time the number of pantographs in the train sets means that the systems are pushed closer to the performance limits.

The subject of overhead line system designs is very complex and hard to survey. Different concepts have developed in different national railway companies — and the different leading railway companies all claim that *they* have the best system. Denmark is not among the frontier countries in railway technology. When the first railway lines in Denmark were electrified, a presumingly thorough tested standard system design was bought for the purpose. This was the right choice at the time. The disadvantage of that approach is that later it is difficult to consider different design details or design changes, etc., without directing any such questions to those the system design was bought from. This would of course lead to additional costs and the result is that the original design concept is never seriously taken up to a renewed consideration. One of the purposes of this ph.d. project has exactly been to take (some of) the design parameters of the danish overhead line system up to renewed considerations.

Another aim of the project has been to investigate the importance of nonlinearities in overhead line systems. The only nonlinearity that is normally included in the modelling of such systems is the slackening effect of the droppers. This slackening is considered undesirable because the droppers are exposed to large stresses when they again become tensioned and there is a substantial risk that they will break.

Our investigations differ from other investigations in this field in that we consider the very weak nonlinearities of the cable motions and compare the importance of these with the importance of the bending stiffness of the cables in the overhead line systems, which is normally considered to be important, even though it is small.

1.3 Outline of the thesis

When writing this thesis it has been the intension that the chapters can be read separately.

Our reason for this is, that even though the train bridge system and the pantograph catenary system are rather similar from a mathematical point of view, they are in the 'real world' very different systems. Those readers interested in one of the subjects will typically have very little interest in the other subject. It is of course also the intension and the hope that the results of the project will be applied by the relevant engineers and decision makers — and these persons may not have too much interest in some of the theoretical considerations in the thesis. Finally it is our hope that other researchers in these fields will take notice of our results — in our opinion they *should*. The thesis therefore also contains investigation results that presently are only of theoretical interest, and readers only interested in the practical applications of the project here and now may find these investigations irrelevant.

In chapter 2 we make some considerations on the treatment of nonlinear systems with discrete and continuous elements in general based on our experiences from this project. Thus this chapter is also sort of introductory.

In chapter 3 we treat train bridge interactions. We give an account of the achievement of the system equations, some theoretical background, and some investigation results.

In chapter 4 we treat pantograph overhead line system dynamics. This is the main subject of the thesis. The chapter is divided into a section on pulse propagation on cables, sections on the design of overhead line systems and their equations of motion, sections on pantograph modelling and coupling of the pantograph and the catenary system, and a section containing results from our numerical investigations.

Finally the appendices contain different stuff that we think should not be omitted but that on the other hand is a little off track from the rest of the thesis.

Chapter 2

Nonlinear dynamical systems with discrete and continuous elements: General considerations and preferable tools

In this chapter we shall reflect on the title of the entire ph.d. project: *Nonlinear dynamical systems with discrete and continuous elements.*

First let us point out that the rather subtle 'systems with discrete and continuous elements' just indicates that we treat systems consisting of elements (or subsystems) with different timescales and very different spatial properties interacting with each other. The interest for precisely these types of systems is due to their frequent appearance — the difficulties are due to the coupling of the two (or more) physically and mathematically fundamentally different systems. Examples of such systems are: The wave flow around a small island, the wind flow around a flexible rod, a ball rolling on an elastic mem-

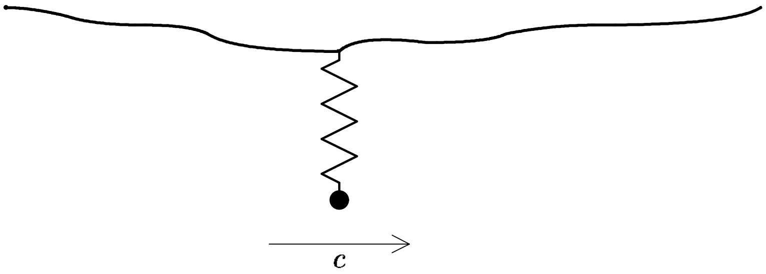

Figure 2.1: String sprung mass system.

brane, a moving sprung mass on a beam, etc. The most important examples with respect to this thesis are: A moving train interacting with a bridge, and the interaction between a pantograph on the roof of a moving electrical train and the overhead line system supplying the energy to the train. These two dynamical problems have been the main subjects of the ph.d. project and the most of this thesis is concerned with considerations and investigations on these systems.

However, in this chapter we will make some considerations, based on personal experience and correspondence with other researchers, on how to deal with systems with discrete and continuous elements in a general sense. We shall treat some aspects and difficulties that arise when treating such systems and we shall make some conclusions on choices of solution methods when dealing with such systems.

As an example we will analyse a system consisting of a string and a sprung mass. This is precisely an example of the type of systems we consider. The string is a continuous object with a certain spatial distribution, the mass is a discrete, localised object. See figure 2.1. Say $v = v(x,t)$ is a variable describing the vertical deflection of the string at position x and time t. Then the motion of the string can be described mathematically by a partial differential equation in the variable $v(x,t)$. If we assume that the motion of the string can be linearised around the static equilibrium configuration, it has the equation of motion:

$$\mu v_{tt} = P_0 v_{xx} - F_c \delta(x - x_m), \tag{2.1}$$

where μ and P_0 are the mass per length and the pretension force of the string, respectively. F_c is the coupling force between the string and the sprung mass. x_m is the position of the coupling to the sprung mass; x_m may be time dependent in which case we have a system with a continuous element and a moving discrete element. The boundary conditions of the string have to be posed as well; we set $v(0,t) = v(L,t) = 0$.

Say $y = y(t)$ describes the vertical motion of the mass. Then the vertical motion of the mass can be described mathematically by an ordinary differential equation in the variable $y(t)$:

$$m y_{tt} = -mg + F_c. \tag{2.2}$$

The continuous element is described mathematically by a partial differential equation whereas the discrete element is described by an ordinary differential equation. To couple the systems numerically, the partial differential equation has to be transformed to a system of ordinary differential equations — the partial differential equation has to be *discretised.*

We shall now consider different ways of discretising the partial differential equations and study the resulting approaches for investigating the string sprung mass system. In our examples we set the physical parameters to $\mu = 1\ kg/m$, $P_0 = 1000\ N$, $m = 1\ kg$ and $L = 100\ m$.

2.1 The Finite Difference Method

First we choose to perform the spatial discretisation of the string equation using a finite difference method with uniform step size h

such that v is approximated by w: $w(i,t) \approx v(i\,h,t)$. The finite difference method is chosen since this is a very flexible method. Small changes in the system equations only cause small changes in the discretised equations. Systems with higher order derivatives, nonlinearities, etc. are easily handled. Finally, a finite difference method for the spatial discretisation gives the possibility to use an explicit time integration scheme. This is easy to implement and if the system is so called nonstiff (roughly, if there is low damping) it makes the time integrations cheap in terms of cpu-time.

2.1.1 Statics of linear system

If we assume that the coupling can be described by a linear spring:

$$F_c(t) = -k\,(y(t) - v(x = x_m, t))\,, \tag{2.3}$$

we have the case of a linear system with discrete and continuous elements. (In the examples we set $k = 10000\ N/m$.) Let us assume that x_m is fixed and study the statics of the system. It turns out that this can be handled rather straight forward. The equations are (before discretisation):

$$\begin{aligned} 0 = &\quad v_{xx} + \tfrac{k}{P_0}\,(y - v(x = x_m))\,\delta\,(x - x_m) \\ 0 = &\quad -mg - k\,(y - v(x = x_m))\,. \end{aligned}$$

The position of the coupling to the sprung mass is assumed to coincide with one of the discretisation points, say the middle one. The finite difference discretised model is illustrated in figure 2.2.

The finite difference method yields:

$$\begin{aligned} v_{xx}(i\,h) &\approx \tfrac{w_{i+1} - 2w_i + w_{i-1}}{h^2} \\ \delta(x - x_m) &\approx \tfrac{\delta_{im}}{h} \quad . \end{aligned}$$

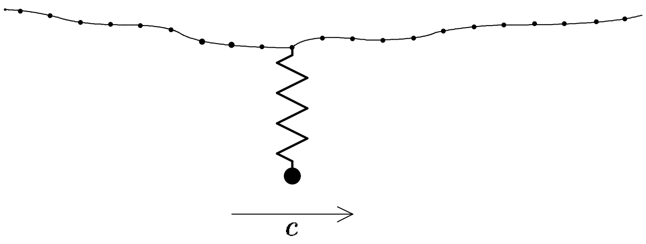

Figure 2.2: The discretised static string sprung mass system.

All together, solving the statical linear problem reduces to solving a linear system of equations on the form:

$$\begin{bmatrix} 1 & & & & & & & \\ & -2 & 1 & & & & & \\ & 1 & -2 & 1 & & & & \\ & & & & \cdots & & & \\ & & & & \cdots & & & \\ & -2-\frac{k}{P_0}h & & & & & & \frac{k}{P_0}h \\ & & & & \cdots & & & \\ & & & & \cdots & & & \\ & & & 1 & -2 & 1 & & \\ & & & & 1 & -2 & & \\ & & & & & & 1 & \\ & kh^2 & & & & & & -kh^2 \end{bmatrix} \begin{bmatrix} w_0 \\ w_1 \\ w_2 \\ w_3 \\ \cdots \\ w_m \\ \cdots \\ w_{n-3} \\ w_{n-2} \\ w_{n-1} \\ w_n \\ y \end{bmatrix} = \begin{bmatrix} 0 \\ 0 \\ 0 \\ 0 \\ 0 \\ 0 \\ 0 \\ 0 \\ 0 \\ 0 \\ 0 \\ mgh^2 \end{bmatrix}$$

which is a very easy task.

2.1.2 Statics of nonlinear system

Now let us assume that the system is no longer purely linear. For example the coupling spring could have a nonlinear characteristic:

$$F_c(t) = -k\left(y(t) - v(x_m,t)\right) - \epsilon\left(y(t) - v(x_m,t)\right)^3 . \tag{2.4}$$

Then we have the case of a nonlinear system with discrete and continuous elements. Let us again assume that x_m is fixed and study the statics of the system. We use the same technique as in the linear case and solving the nonlinear statical problem reduces to solving a nonlinear system of equations:

$$\begin{aligned}
w_0 \quad &= 0\\
-2w_1 + w_2 \quad &= 0\\
w_1 - 2w_2 + w_3 \quad &= 0\\
&\vdots\\
w_{m-1} - 2w_m + w_{m+1} + \tfrac{k}{P_0}h\,(y - w_m) + \tfrac{\epsilon}{P_0}h\,(y - w_m)^3 \quad &= 0\\
&\vdots\\
w_{n-3} - 2w_{n-2} + w_{n-1} \quad &= 0\\
w_{n-2} - 2w_{n-1} \quad &= 0\\
w_n \quad &= 0\\
kh^2 w_m + \epsilon h^2 w_m^3 - kh^2 y - \epsilon h^2 y^3 \quad &= -mgh^2
\end{aligned}$$

This is of course a harder task than the corresponding linear problem. But it is still relatively simple. A method for solving nonlinear equations, for example the well-known Newton-Raphson method or a modification of this, is a good suggestion for solving the nonlinear equation.

2.1.3 dynamical system

Until now we have concluded that handling the statics of the linear or the nonlinear system with continuous and discrete elements can be reduced to handling a linear or nonlinear equation respectively, if a finite difference method is used for the spatial discretisation. The statics do not pose serious trouble. Note that to come to this conclusion we have assumed that the discreteness in the system, the position of the coupling to the sprung mass, is located at one of the discretisation points. If the position of the coupling to the sprung

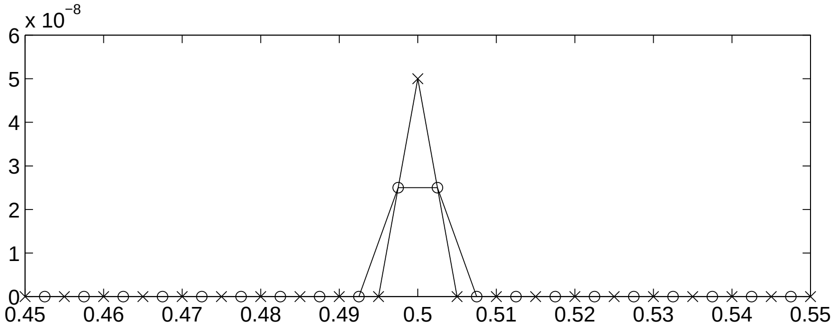

Figure 2.3: Deflection of the nodes of the discretised string excited with a concentrated force in one time step: 1) (×) force at node; 2) (○) force between two nodes.

mass is not coinciding with one of the discretisation points, the coupling has to be distributed to the adjacent discretisation points in the discretised equations. For the statics this does not pose serious trouble either. The numerical method converges and we can just refine the discretisation grid until there is a satisfactory preciseness in the numerical solution.

We shall now proceed to consider the *dynamical* string sprung mass system. We shall find that *now* all our trouble starts.

First let us consider the situation where x_m is fixed and let Fc be a constant force which means that the continuous and the discrete systems are decoupled. We can then solve the partial differential equation that describes the motion of the string. We compare the two situations

1. the location of the concentrated force coincides with a discretisation point
2. the location of the concentrated force is between two discretisation points.

The initial condition of the string is $v(x,0) = 0$. Figure 2.3 shows the deflection of the string around the concentrated force after a single time step. The crosses indicate the positions of the discretisation points in situation 1 whereas the circles indicate the positions of the discretisation points in situation 2. We note that the result looks plausible and is the best thing we could expect with a finite difference method. We can also show that the method converges spatially and we find that the solutions from situation 1 and 2 approach each other as we take more time steps. However, in situation 2, how shall we represent the deflection of the string at the position of the concentrated force? It is obvious that linear interpolation gives a wrong result. So do different higher order polynomial interpolations and spline approximations. We realise that we will have to modify our discretisation of the dirac delta function — the discreteness — to make any of the interpolations work. This already sounds like trouble since we would then use different spatial discretisations of the dirac delta function in the statical and dynamical systems respectively. Alternatively and much better, we can discretise using a nonuniform grid and *force* a grid point at the position of the concentrated force.

The problematic representation of the deflection of the string at the position of the concentrated force, if the force is located between two nodes, turns out to be crucial when the continuous system is coupled with the *moving* discrete system. Because now the contact force is no longer just a constant. It *depends* on the deflection of the string at the position of the concentrated force. We can not just make the grid nonuniform either, since the concentrated force is moving. The problem with representing the string deflection between grid points is then transferred directly to the evaluation of the concentrated force. For a very stiff spring, the spring force signal will contain large, purely numerical oscillations related to this problem. Lets illustrate it with our string sprung mass system. We now let the mass move horizontally $x_m(t) = c \cdot t$. (In all the following examples we set $c = 20\ m/s$.) In figure 2.4 we illustrate the force in the spring, coupling the continuous and the discrete systems, as a function of the travelled distance. The horizontal position of the discretisation points is illustrated by the grid in the figure. The deflection of the

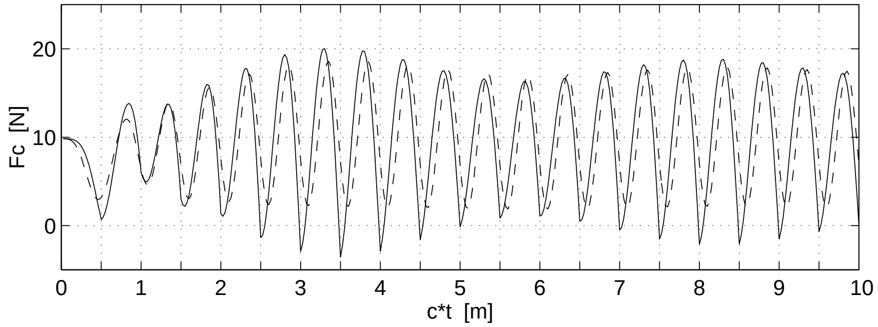

Figure 2.4: FDM, $h = 0.5\ m$. The contact force when: 1) (—) the string deflection is estimated with linear interpolation; 2) (- -) the string deflection is estimated with cubic spline interpolation.

string is estimated by linear interpolation (full line) and cubic spline interpolation (broken line). It is seen that large oscillations clearly connected to the spatial discretisation step size appear in the contact force signal. The problem can be solved by refining the discretisation grid drastically. This is illustrated in figure 2.5 in which we see the contact force signal for 4 different levels of discretisation fineness. The grids in the figure indicate the spatial step sizes. The string has been discretised with 201 grid points in the upper graph, 401 grid points in the next graph, 801 in the third graph and 1601 grid points in the bottom graph. Linear interpolation was used to represent the string deflection between grid points. It is seen that the signal converges but that the convergence is slow. For achieving numerical stability in the time integration, a constraint is put on the maximal time step size. Since this constraint is proportional to the spatial step size this obviously limits the refinement of the discretisation grid. In practice a sufficient discretisation fineness is often not attainable, both in terms of computer memory and in terms of cpu-time for the time integrations.

We conclude that often the finite difference method is not sufficiently convergent for this type of problem, the *dynamical* problem. This has

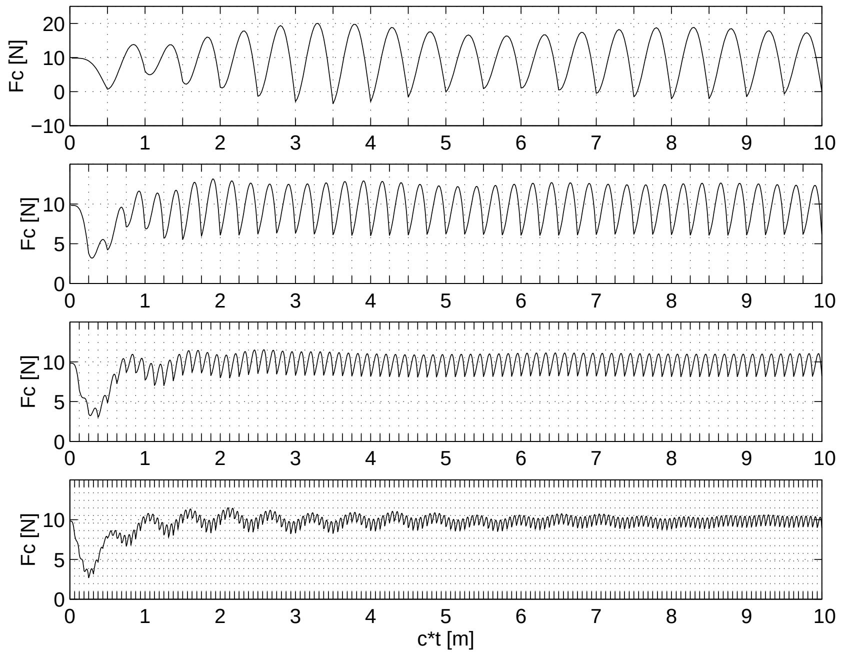

Figure 2.5: FDM, contact force signal as function of travelled distance with 4 different spatial step sizes: $h = 0.5\ m$, $h = 0.25\ m$, $h = 0.125\ m$, $h = 0.0625\ m$.

great relevance for pantograph overhead line system investigations such as those described later in this thesis. Some other research teams use the finite difference and similar methods to investigate the dynamics of pantograph overhead line systems ([35], [36], [37]). And they do obtain time series of the contact force from their simulations containing non-physical high frequent oscillations similar to the ones illustrated in figure 2.4. To get rid of the oscillations the contact force time series are filtered. The resulting low frequent time series for the contact force look plausible and the researcher teams claim they are in good agreement with reality. We must admit that we feel inconvenient with this approach. Filtering of an output signal can be a good and relevant idea if there is a reasonable proportion between the energy contained in the final (filtered) signal and the original (unfiltered) signal. But filtering an output signal to make a nonconverged numerical result converge is very unconvincing. And if the vast majority of the energy in some signal is contained at frequencies such that it for output purposes is discarded by filtering, but for feedback purposes within the simulation it is remained, the whole numerical procedure is discussable. Additionally it is not clear that there are no longtime misrepresentations of the contact force due to the difficulties with the representation of the cable deflection at the position of the pantograph. We find that the finite difference method is very ill suited to investigate the dynamics of systems with continuous and moving discrete elements, if the continuous system is a relatively flexible structure and the coupling is stiff — such as it is in the case of pantograph overhead line systems. For those reasons we choose to skip the finite difference method in my investigations.

2.2 Spectral Methods

Another discretisation method for partial differential equations is the so called spectral and pseudo-spectral methods. (Basically a spectral method is a method which changes variable: The unknown variable is approximated by a sum of known smooth functions. The coefficients of these functions are then the new variables. A system of ordinary differential equations for the spectral coefficients has to be solved and the result transformed back to physical space. The pseudo-spectral methods exploit some of the properties of the spectral methods, but stay in the physical space.) For smooth systems with smooth dynamics a very satisfactory preciseness can be obtained with relatively low computer memory demands when using these methods. Spectral and pseudo-spectral methods are also quite good suited for handling nonlinear systems. However, these methods are not very well suited for nonsmooth systems with nonsmooth dynamics. In systems with discontinuities a phenomenon called Gibbs phenomenon can be very disturbing when using spectral and pseudo-spectral methods. (Basically Gibbs phenomenon is a result of nonuniform convergence around a discontinuity). As is almost implicitly understood from the title of the ph.d. project, some sort of discontinuities are likely to be present in systems with discrete an continuous elements. The extent and order of the discontinuities will of course depend on the exact system and the physical parameters. Gibbs phenomenon will make the coupling procedure very difficult and unreliable. We have assessed that it was not worth the effort trying out a spectral or pseudo-spectral method to the investigations in this thesis.

2.3 Modal Analysis – Separation of Variables

A useful tool for investigating linear structural dynamics is modal analysis. And for linear systems with discrete and continuous elements modal analysis is a very strong approach. The coupling between the discrete and the continuous systems is easily handled as we will see in a moment. It is a drawback that the modal shapes and frequencies of the structure in consideration have to be calculated in advance. It makes the method more inflexible. But often these have already been calculated for other purposes and they are then easily accessible. This is for example often the case for bridges where modal shapes and frequencies are important design characteristics and thus have to be computed for this reason. With certain assumptions the case with a moving excitation on the bridge can advantageously be handled using a modal approach.

We will illustrate the method with the linear string sprung mass model given by (2.1), (2.2) and (2.3). The deflection of the string is discretised as:

$$v(x,t) = \sum_{i=1}^{\infty} A_i(t) \sin\left(\frac{i\pi x}{L}\right).$$

Note that in the test example we are able to write the modal shapes on closed form. For more complex systems the modal shapes may have to be computed numerically. The expansion gives

$$v_{tt} = \sum_{i=1}^{\infty} \ddot{A}_i \sin\left(\frac{i\pi x}{L}\right) \quad \text{and} \quad v_{xx} = -\sum_{i=1}^{\infty} \frac{i^2\pi^2}{L^2} A_i \sin\left(\frac{i\pi x}{L}\right).$$

Hence the partial differential equation (2.1) is rewritten as

$$\sum_{i=1}^{\infty} \left(\ddot{A}_i + \frac{i^2\pi^2 P_0}{\mu L^2} A_i\right) \sin\left(\frac{i\pi x}{L}\right) = -\frac{F_c}{\mu}\delta(x - x_m).$$

We now use the orthogonallity of the mode shapes. We multiply with $\sin\left(\frac{j\pi x}{L}\right)$ and integrate over the length of the string (Galerkins method):

$$\begin{aligned} \int_0^L \sum_{i=1}^{\infty} \left(\ddot{A}_i + \tfrac{i^2\pi^2 P_0}{\mu L^2} A_i\right) \sin\left(\tfrac{i\pi x}{L}\right) \sin\left(\tfrac{j\pi x}{L}\right)\, dx = \\ -\int_0^L \tfrac{F_c}{\mu}\delta(x - x_m) \sin\left(\tfrac{j\pi x}{L}\right)\, dx \end{aligned}$$

which yields the differential equations for the coefficients of the modal shapes:

$$\left(\ddot{A}_j + \frac{j^2\pi^2 P_0}{\mu L^2} A_j\right) \frac{L}{2} = -\frac{F_c}{\mu} \sin\left(\frac{j\pi x_m}{L}\right).$$

The differential equations show that in case of a moving force, $x_m = x_m(t)$, in principle all modes are excited. In numerical simulations

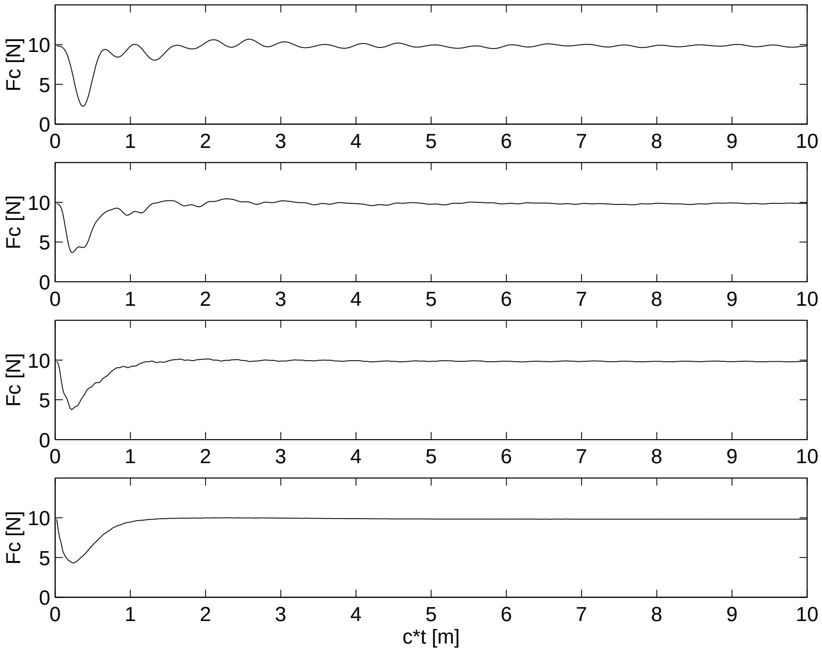

Figure 2.6: The contact force in modal approach simulations with the first 200, 400, 800 and 1600 modes of the string included.

the expansion will of course have to be cut off at some point and it is not clear how many modes should be included in the model. The more flexible the continuous system is compared to the discrete system, the more modes will have to be included. Some preliminary experiments will have to be performed to decide the number of modes that have to be included. In figure 2.6 we have used the modal approach to perform a simulation of the string sprung mass system corresponding to figure 2.5 (which was based on the finite difference method). We see that the convergence of the contact force signal is much faster than in figure 2.5.

The major drawbacks with the modal approach in my case is its lack of suitability to handle systems with discrete and continuous elements if the continuous elements contain nonlinearities. The method is very ill-suited for handling nonlinearities. It is not impossible to handle nonlinear systems using a modal approach but it is tedious and awkward and in addition leaves a very expensive time integration in means of computer power.

2.4 Finite Element Methods

Using the finite element or the finite difference methods for spatially discretisation of partial differential equations are rather similar processes. The discretised equations are similar. Both methods are flexible so that small changes in the system equations only cause small changes in the discretised equations. Higher order derivatives, nonlinearities etc. are most easily handled with the finite difference method. There is more preparatory work connected with the finite element method. And the finite element method leaves a so called implicit scheme for the time integrations which means that a system of equations has to be solved in each time step. In systems with discrete and continuous elements this is often a disadvantage: The discrete and the continuous subsystems often have different time scales and the possibility of using rather large time steps in the time integrations, allowed by the implicit integration scheme, is not fully exploited due to time step constraints from the discrete system. Different time steps for the discrete and the continuous system is then a possibility. It is rather awkward, though.

However, for systems with discrete and continuous elements, the finite element method is much preferable due to the straight forward coupling of the two subsystems. The coupling is handled analytically in the discretisation process. We will illustrate that with the string sprung mass model given by (2.1), (2.2) and (2.3). For that purpose (2.1) is rewritten in its weak form:

$$\int_0^L \mu v_{tt} W \, dx + \int_0^L P_0 v_x W_x \, dx = -\int_0^L F_c \delta(x - x_m) W \, dk \qquad (2.5)$$

where W is the test function and has to obey certain differentiability and boundary conditions.

2.4.1 Piecewise linear basis functions

The order of the partial differential equation is decisive for the choice of basis functions in the discretisation. Since the weak formulation of the partial differential equation for the string model contains derivatives of first order, all we must demand of the basis functions is that they are continuous. The simplest choice is to use piecewise linear functions as basis functions. Thus, the string is divided into elements of equal length h, and $v(x,t)$ is approximated by

$$v(x,t) = \sum_{i=0}^{n} b_i(t)\theta_i(x),$$

where θ_i is given as

$$\theta_i(x) = \begin{cases} \frac{1}{h}(x-x_i)+1 & , \quad x_{i-1} \le x \le x_i \\ -\frac{1}{h}(x-x_i)+1 & , \quad x_i \le x \le x_{i+1} \\ 0 & , \quad \text{otherwise.} \end{cases}$$

The near orthogonality of the basis functions is exploited. We let the test function W successively be $\theta_1, \theta_2, \ldots, \theta_{n-1}$ and perform the integrations, which then yield a system of ordinary differential equations for the coefficients b_i. The i'th equation reads:

$$\frac{h\mu}{6}\ddot{b}_{i-1} + \frac{2h\mu}{3}\ddot{b}_i + \frac{h\mu}{6}\ddot{b}_{i+1} - \frac{P_0}{h}b_{i-1} + \frac{2P_0}{h}b_i - \frac{P_0}{h}b_{i+1} = F_c\theta_i(x_m).$$

Note that as a contrast to the finite difference method there is not a problem with representing the string deflection. The string deflection at the position of the concentrated force is simply given as $v(x_m,t_0) = \sum_{i=0}^{n} b_i(t_0)\theta_i(x_m)$. In figure 2.7 we show the results of simulations with the string divided into 200, 400, 800 and 1600 elements respectively, corresponding to the discretisation fineness in

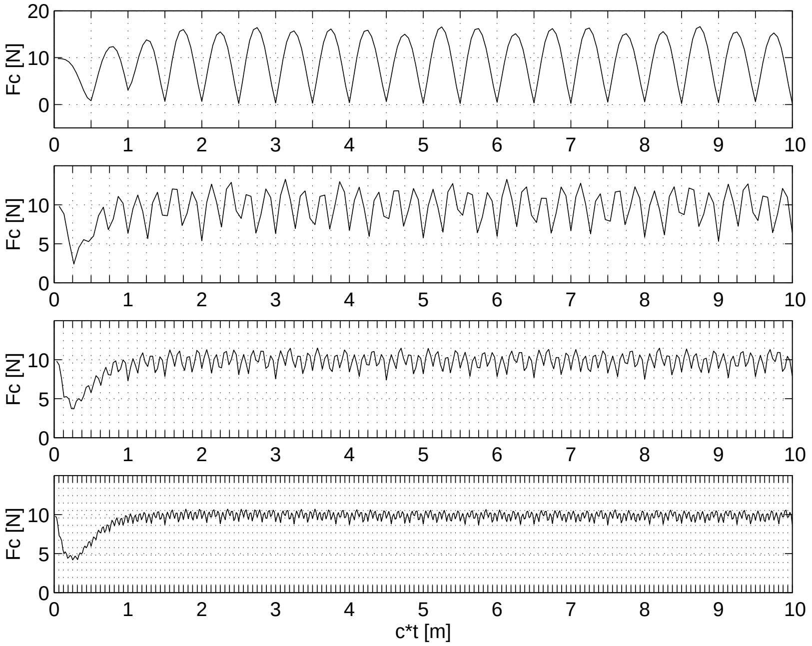

Figure 2.7: FEM, piecewise linear basis functions. Contact force signal as function of travelled distance with 4 different element sizes: $h = 0.5\ m$, $h = 0.25\ m$, $h = 0.125\ m$, $h = 0.0625\ m$.

figure 2.5 obtained with the finite difference method. Note that even though the process of coupling of the discrete with the continuous systems is much better and clearer with the finite element method than with the finite difference method, only slightly better convergence is obtained. The problems with the computer power limitations remain.

2.4.2 Piecewise cubic basis functions

We will therefore try to discretise with basis functions of higher order. We now demand of our basis functions that they are continuous and that their first derivatives are also continuous. (This is obtained by developing with two sets of basis functions as will be illustrated in a moment.) Note that in case of the string the last demand would normally be considered as a redundancy; mathematically it is not strictly nescessary that the basis functions have continuous first derivatives, so why do the extra work? We will find that the extra smoothness of the basis functions speeds up the convergence in the case of the coupling of the string and the sprung mass.

Two sets of constants are needed to secure continuity of both v and v_x. Thus $v(x,t)$ is approximated by

$$v(x,t) = \sum_{i=0}^{n} \left(b_i(t)\phi_i(x) + c_i(t)\psi_i(x)\right),$$

where the simplest choice of the ϕ and ψ functions are the piecewise cubic functions:

$$\phi_i(x) = \begin{cases} -\frac{2}{h^3}(x-x_i)^3 - \frac{3}{h^2}(x-x_i)^2 + 1 & , \quad x_{i-1} \le x \le x_i \\ \frac{2}{h^3}(x-x_i)^3 - \frac{3}{h^2}(x-x_i)^2 + 1 & , \quad x_i \le x \le x_{i+1} \\ 0 & , \quad \text{otherwise} \end{cases}$$

and

$$\psi_i(x) = \begin{cases} \frac{1}{h^2}(x-x_i)^3 + \frac{2}{h}(x-x_i)^2 + (x-x_i) & , \quad x_{i-1} \le x \le x_i \\ \frac{1}{h^2}(x-x_i)^3 - \frac{2}{h}(x-x_i)^2 + (x-x_i) & , \quad x_i \le x \le x_{i+1} \\ 0 & , \quad \text{otherwise.} \end{cases}$$

By then letting W run through $\phi_1, \phi_2, \ldots, \phi_{n-1}, \psi_0, \psi_1, \ldots, \psi_n$ and perform the integrations, we obtain a system of ordinary differential equations for the coefficients $b_i(t)$ and $c_i(t)$. The i'th equation for $1 \le i \le n-1$ is:

$$\begin{aligned} &\tfrac{9h\mu}{70}\ddot{b}_{i-1} + \tfrac{26h\mu}{35}\ddot{b}_i + \tfrac{9h\mu}{70}\ddot{b}_{i+1} + \tfrac{13h^2\mu}{420}\ddot{c}_{i-1} - \tfrac{13h^2\mu}{420}\ddot{c}_{i+1} - \\ &\tfrac{6P_0}{5h}b_{i-1} + \tfrac{12P_0}{5h}b_i - \tfrac{6P_0}{5h}b_{i+1} - \tfrac{P_0}{10}c_{i-1} + \tfrac{P_0}{10}c_{i+1} = -F_c\phi_i(x_m) \end{aligned}$$

and the i'th equation for $n \le i \le 2n$:

$$\begin{aligned} &\tfrac{13h^2\mu}{420}\ddot{b}_{i-1} - \tfrac{13h^2\mu}{420}\ddot{b}_{i+1} - \tfrac{h^3\mu}{140}\ddot{c}_{i-1} + \tfrac{2h^3\mu}{105}\ddot{c}_i - \tfrac{h^3\mu}{140}\ddot{c}_{i+1} + \\ &\tfrac{P_0}{10}b_{i-1} - \tfrac{P_0}{10}b_{i+1} - \tfrac{hP_0}{30}c_{i-1} + \tfrac{4hP_0}{15}c_i - \tfrac{hP_0}{30}c_{i+1} = -F_c\psi_i(x_m). \end{aligned}$$

In figure 2.8 we show the results of simulations with the string divided into 100, 200, 400 and 800 elements respectively, corresponding to the discretisation orders in figures 2.5 and 2.7 obtained with the finite difference method and the finite element method with piecewise linear basis functions respectively. It is seen that the convergence is faster due to the extra smoothness in basis functions. Even faster convergence would probably be obtained by increasing the order of the basis functions further. However, we have not tried it out since there is quite some work connected with the discretisation itself.

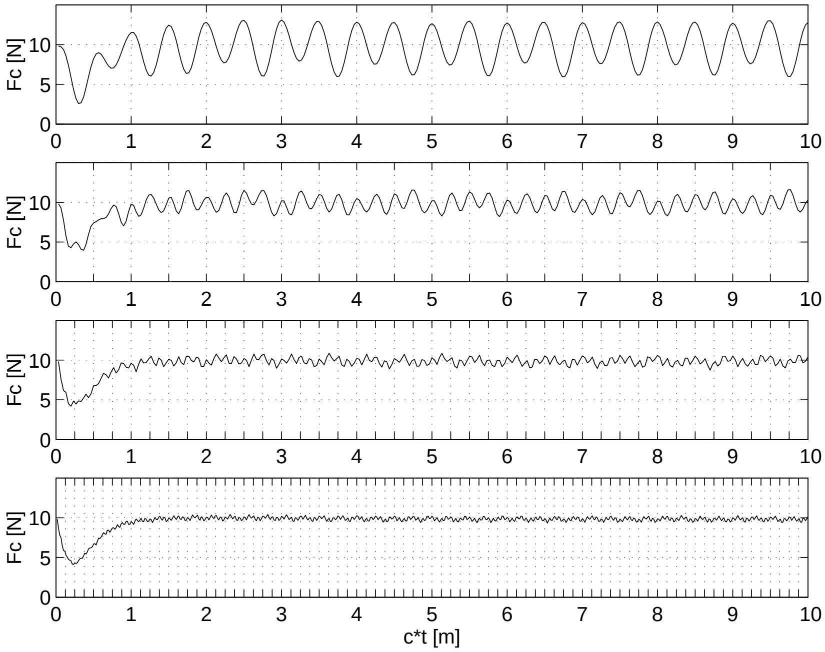

Figure 2.8: FEM, piecewise cubic basis functions. Contact force signal as function of travelled distance with 4 different element sizes: $h = 1\ m$, $h = 0.5\ m$, $h = 0.25\ m$, $h = 0.125\ m$.

2.5 My preferable tools for the spatial discretisation of nonlinear systems with discrete and continuous elements

We have gone through some of the considerations made during the time of the ph.d. study. We have considered different approaches for the spatial discretisation of the continuous part of the nonlinear systems with discrete and continuous elements. In the test example we found that since there is no ambiguisy in the coupling process of the discrete and continuous subsystems — the deflection of the string is defined everywhere — discretising the string with a finite element method with piecewise cubic basis functions is preferable to discretisation with for example the finite difference method. This is also my experience from the investigations of the pantograph overhead line systems.

We have found the finite element method with piecewise cubic basis functions to be the overall most convenient approach. In special cases, e.g. if the continuous element is linear and/or only few modes are needed for a satisfactory description, and the two subsystems couple quasistatically, then the modal approach may be a strong alternative.

Later in this thesis we shall see that we have used the modal approach for the train bridge system and the finite element approach for the pantograph overhead line system.

Chapter 3

Train bridge interaction

In this chapter we shall consider one of the two main examples of 'dynamical systems with continuous and discrete elements', the train bridge system. A bridge obviously is a continuous system with a spatial distribution. In this thesis we will only consider the trains as discrete systems. By this we mean that we will only consider multi body motion of the trains. We neglect effects connected to elastic deformations of bogies, wheel sets, car bodies, etc. Our train models will of course have a spatial distribution: A disturbance (for example a displacement) at the front end of the train can propagate along the train according to the dynamics of the multi body system. However, in the coupling of the train and bridge models, the excitation on the bridge from the train will appear at discrete points — namely given by the positions of the wheel sets.

We shall also assume that the rails follow the bridge closely and neglect the substructure between the bridge and the rails.

These are of course approximations — some would say crude approximations — of physical trains and bridges interacting. It has had to be this way to limit the level of complexity. Besides, the effect of introducing these approximations may be assessed and it will be found, that in most cases they are justified. For a general introduction to the subject of train bridge interaction see [9] and [8].

The complexity of the train bridge model comes from the inclusion of the geometrical and the frictional nonlinearities in the wheel rail contact surface. The wheels and rails are modelled with realistic profiles. Investigations of train models including such nonlinearities have shed light on a number of dynamical features for trains: Hunting of bogies, linear and nonlinear critical speeds, chaotic motion of the bogies, etc. See [28] and [41] for a thorough description of many of these subjects.

The aims of the train bridge investigations in this project have been

- to develop a program for train bridge simulations for industrial use, with a relatively complex train model.
- To investigate if there are any special dynamical effects connected to the combination of the nonlinear train model and the flexible superstructure.

First we will follow the methodology of setting up the equations for the train bridge interaction investigations as it has been done in this project. We shall then study a few results from some of the simulations.

3.1 Modelling the Dynamics of the Bridge

We have been interested in global effects of the dynamical interaction between the flexible bridge model and the nonlinear train model. A bridge is designed such that the bridge deck only exhibits small deflections when excited. This means that for global investigations the bridge can be assumed to behave in a linear way. For local effects near expansion joints, etc. this is not necessarily true. However, this is not the subject of the train bridge investigations in this thesis. See for instance [15].

Since we only consider global effects, and since the characteristic time scales for the motion of a bridge and the motion of a train respectively most often are very different for realistic train speeds, the bridge dynamics and the train dynamics can be considered separately. The bridge model and the train model can be discretized in time separately and then coupled also between the time steps. As described in chapter 2 the modal approach is then a good suggestion for numerical investigations of the system.

We will now describe the modal analysis of a bridge model and set up the equations of motion of the bridge excited by time dependent concentrated forces.

3.1.1 Modal Description of the Bridge Motion

One of the strong points of adopting a modal description of the motion of a bridge is, that often the huge work load connected with making the exact modelling of the bridge has already been carried out for other purposes. For instance the modal frequencies and shapes of a bridge are computed in the design stadium to prevent the so-called flutter problems, to asses wind induced forces, the impact of earthquakes, simple load amplification factors, etc. Thus, the modal frequencies and shapes of the bridge may be already available for the investigations of the dynamics of the bridge excited by a moving train.

The program developed during this ph.d. study has been used for commercial train-bridge interaction investigations [16], where the modelled bridges were projected for the future bridges connecting Denmark and Sweden. The modal frequencies and modal shapes of the bridges were computed with the commercial finite element program, ALGOR [1].

In this section I will set up a simple bridge model and compute the modal shapes and frequencies and I will then derive the equations of motion for the modal coefficients. Such a simple bridge model is

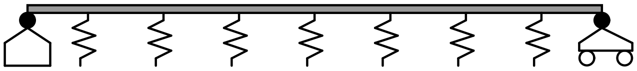

Figure 3.1: Simple bridge model: Simply supported beam with intermediate supports modelling the piers.

convenient (and necessary) for investigations of the bridge parameter dependence on the train bridge interactions. A finite element model of a real bridge may have thousands of degrees of freedom, and a computation of even the first few modes can be a very cpu-expensive task. For the simple bridge model in this section, however, the computation of the modal shapes and frequencies is no big deal.

The simple bridge model is illustrated in figure 3.1. It consists of a beam, simply supported at the ends and supported intermediately by springs. By making the springs very stiff they will in the limit model the piers. The eigenmodes and eigenshapes can not be calculated analytically for this bridge model. We estimate them using the Rayleigh-Ritz method, [42]. We let the deflection of the beam be described by the variable $v(x,t)$. The motion of the unforced beam is described by the partial differential equation

$$\mu v_{tt} = -EI v_{xxxx} - \sum_{r=1}^{p} k\, v(x_r, t) \tag{3.1}$$

where μ is the mass per length and EI is the bending stiffness of the beam, p is the number of intermediate supports, k is the value of the spring constants, and x_r is the position of spring number r.

We search for harmonic motion solutions of the beam:

$$v(x,t) = f_l(x)\sin(\omega_l t)$$

where ω_l is the l'th cyclic modal frequency and f_l is the associated modal shape. We write $f_l(x)$ as a linear combination of N functions

$$f_l(x) = \sum_{i=1}^{N} a_{l,i}\phi_i(x)$$

where $\phi_1, \phi_2, \ldots, \phi_N$ are fixed and linearly independent.

By energy considerations, choosing the linearly independent functions as $\phi_i = \sin(\frac{i\pi x}{L})$ and exploiting their orthogonality, approximations to the squared cyclic frequencies can be found as the eigenvalues of the system:

$$\left(\underline{\underline{A}} - \omega_l^2 \underline{\underline{B}}\right) \underline{a_l} \tag{3.2}$$

where $\underline{a_l} = (a_{l,1}, a_{l,2}, \ldots, a_{l,N})^T$, the components in $\underline{\underline{A}}$, are given by

$$A_{ij} = \frac{EI\pi^4 i^4}{2L^3}\delta_{ij} + \sum_{r=1}^{p} k \sin\left(\frac{i\pi x_r}{L}\right) \sin\left(\frac{j\pi x_r}{L}\right)$$

and $\underline{\underline{B}}$ is the diagonal matrix given by the components

$$B_{ij} = \frac{\mu L}{2}\delta_{ij}.$$

The accuracy of the highest order approximated modal frequencies decreases with the order. Therefore the number of linearly independent functions N should be much larger than the number of modal frequencies N_m, which we want to approximate. A rule of thumb says $N > 3N_m$.

In figure 3.2 we have illustrated the first 4 mode shapes of the bridge model illustrated in figure 3.1. The mode shapes have been computed with the parameters set as $\mu = 40000\ kg/m$, $EI = 7.2 \cdot 10^{12}\ Nm^2$, $k = 10^{10}\ N/m$ and the positions of the springs are the grid points in the figure.

3.1.2 Equations of motion for the excited bridge

Now we consider the motion of the bridge as it is excited with a time dependent load. We consider the piers as inflexible; this gives extra

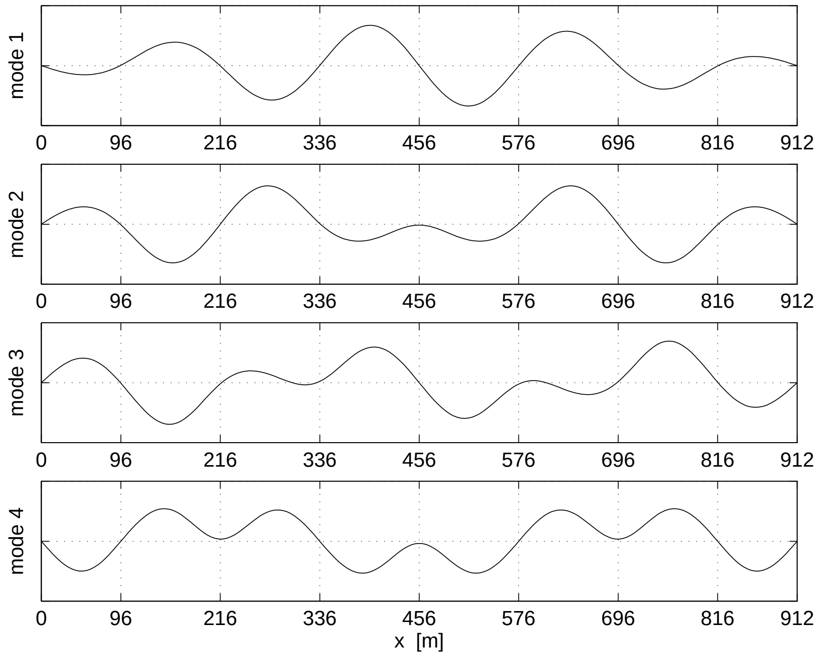

Figure 3.2: The first 4 mode shapes of the simple bridge model. The corresponding modal frequencies are $f_1 = 1.52\ Hz$, $f_2 = 1.69\ Hz$, $f_3 = 1.94\ Hz$, and $f_4. = 2.25\ Hz$.

boundary conditions and the modal shapes are as found above for $k \to \infty$. Thus the motion of the bridge is given as

$$v(x,t) = \sum_{i=1}^{N_m} \Gamma_i(t) f_i(x), \tag{3.3}$$

where f_i is a set of orthonormal functions, normalized by (3.5). The equation of motion is

$$\mu v_{tt} + EI v_{xxxx} = Q(x,t) \tag{3.4}$$

where Q is the load. Inserting (3.3) in (3.4) yields

$$\sum_{i=1}^{N_m} \left(\mu \ddot{\Gamma}_i f_i + EI\, \Gamma_i f_i'''' \right) = Q(x,t).$$

From the modal development we have that

$$EI f_i'''' = \mu \omega_i^2 f_i$$

and assuming we have normalised the modal shapes with the mass per length as weight:

$$\int_0^L f_i(x) \mu(x) f_j(x)\, dx = \delta_{ij}. \tag{3.5}$$

A Galerkin procedure leads to the equation of motion for the i'th modal coefficient:

$$\ddot{\Gamma}_i + \omega_i^2 \Gamma_i = \int_0^L Q\, f_i\, dx. \tag{3.6}$$

We now assume that the time dependent excitation is a sum of n_f time dependent concentrated forces (for instance at the positions of the wheel sets), $Q(x,t) = \sum_{j=1}^{n_f} F_j(t)\delta(x - x_j(t))$. By also including a term for the modal damping, the equation of motion of the i'th modal coefficient finally becomes

$$\ddot{\Gamma}_i + \eta \dot{\Gamma}_i + \omega_i^2 \Gamma_i = \sum_{j=1}^{n_f} F_j\, f_i(x_j(t)). \tag{3.7}$$

3.2 Obtaining the equations of motion for the train model

We will now proceed to the modelling of the train. We have used two different train models in our investigations. The first one is the so-called cooperrider bogie with inclusion of realistic wheel and rail profiles, vertical motion, and an additional mass modelling half a car body. Only the dynamics of the suspended bogie and half the car body mass is modelled. The rest of the train appears as constant forces exciting the bridge motion, located at the positions of the wheels. The assumed location of the cooperrider bogie is in the rear end of the train where the most violent impact from the bridge dynamics is expected. A description of the cooperrider bogie can be found in [27].

The second train model is a 3 dimensional multi body model of the danish intercity train, the Adtranz IC3 train. This train is a so-called flexliner, which means that the train is designed so that units with a length of 3 cars are easily coupled and decoupled and the design can easily be modified for use as EMUs, DMUs, Intercity or regional trains. In this way the train capacity can be adjusted along the route and the separate units can go in different directions after uncoupling. We only adopt a single IC3 unit in the train model.

The modelling of the IC3 train can be divided into two parts: Modelling of the multi-body dynamics (remember that we neglect the effects of structural flexibility etc.) and modelling of the contact dynamics. As to the last part, we have adopted the railway contact mechanics subroutines developed by Jens Christian Jensen, [28]. We will now outline the procedure for setting up the equations for the multi-body dynamics of the IC3 train. Afterwards we shall describe the basic principles for the contact mechanics.

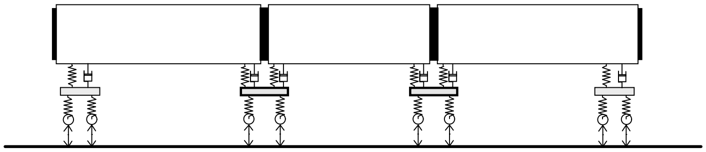

Figure 3.3: The IC3 model consists of 15 rigid bodies: 3 car bodies, 4 bogie frames and 8 wheel sets.

3.2.1 Multi-body Modelling of the IC3 train

Modelling multi body dynamics by hand is not difficult in principle. It is, however, a tedious and tiresome task, and there is a severe risk of making errors when the equations are formulated and when they are implemented in a computer program. Instead I have chosen to use the commercial multi-body dynamics program AUTOSIM for the modelling of the multi-body dynamics part of the train model. See [43].

The train model consists of 3 car bodies supported by 4 bogies. The bogies at the ends of the train that only attach to one car body (each) are called end bogies. The mid bogies that are suspended to two car bodies (each) are called Jacobs bogies. Each bogie consists of a frame and 2 wheel sets. All together we end up with a multi body system of 15 rigid bodies. See figure 3.3.

In a moving coordinate frame the car bodies and bogie frames have 5 degrees of freedom: Displacement in vertical and lateral directions and rotation around 3 axes. The wheel sets have 4 degrees of freedom: displacements in vertical and lateral directions and rotations around the longitudinal and the vertical axes. This all adds up to 67 degrees of freedom for the IC3 train.

Modelling the bogies is the key to modelling the whole multi body-system. The wheels and the car bodies interact via the bogies and all the suspensions are contained in the bogies. All the suspensions are assumed to have linear characteristics. In figure 3.4 we illustrate our model of one of the Jacobs bogies.

Once the physical parameters for the rigid bodies and the suspensions are determined — spring and damper constants, masses and moments of inertia, centre of gravity for each body, geometrical data for dimensions and attachment points — all these informations have to be plugged into AUTOSIM. A global reference coordinate system and local coordinate systems for each body are defined. The attachment points are defined within each local coordinate system and named (globally). This is illustrated in figure 3.5 where the centre of gravity plus all the enumerated defined points within each rigid body are seen. The points on the wheel sets defining the attack points of the forces from the rails are fixed to their static equilibrium positions. For a real wheel set the positions of the contact points on the wheels are dependent of the displacement of the wheel set. See [28].

Finally a force relation is defined for each suspension element, including the informations about which points the force relates to. The wheel rail contact forces are stated as undefined.

AUTOSIM can be told to deliver the output results for the dynamics of the multi-body system as FORTRAN subroutines as well as MATLAB functions. Thus the difficult job of implementing the equations of motion of the system is already taken care of.

After AUTOSIM is done, the wheel rail contact forces have to be applied to the multi body system.

3.2.2 Wheel Rail Contact Mechanics

Modelling the wheel rail contact for realistic wheel and rail profiles is by no means a trivial task. It involves a kinematic, geometric problem, and a contact mechanical problem. The execution of this modelling procedure entails a considerable time consumption. In his ph.d. work, Jens Christian Jensen modelled and analysed the wheel

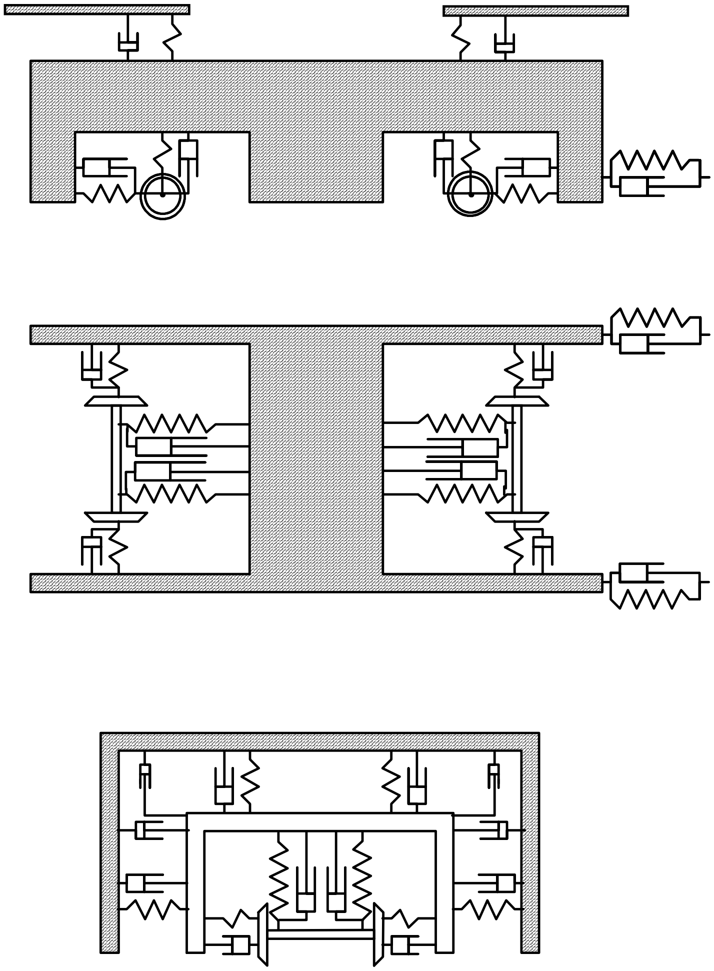

Figure 3.4: The model of a Jacobs bogie.

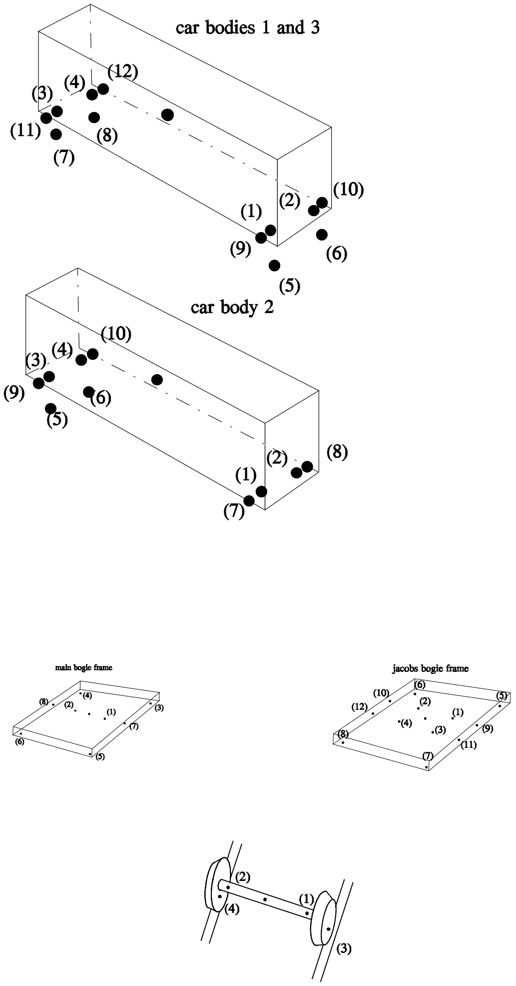

Figure 3.5: Definition of attachment points in each rigid body.

and rail contact problem, in connection with vehicle dynamics investigations, [28]. With his permission I have adapted the subroutines he developed and modified them for my model. In this section a very short introduction to the subject of wheel rail contact will be given. For a more thorough description of the subject we refer to [28] or [29].

The wheel-rail contact is responsible for making the whole train bridge system nonlinear. The nonlinearities stem from the geometry of the bodies in contact (the wheelsets and the rails), as well as from the frictional forces between wheels and rails, the so called creep forces.

The kinematic contact problem can be handled by describing the motions of the two bodies with differential algebraic equations, which express the constraints for the bodies in contact. We use an alternative approach, namely the more realistic flexible method which permits deformation of the two bodies, describing their finite elasticity. (The flexibility is described by allowing the bodies in the model to penetrate eachother.) The motions of the two bodies are now described by coupled ordinary differential equations. The flexible approach is preferable for the rail-wheel contact problem, since the handling of multiple point contact situations is easier.

In figure 3.6 the contact point determination is illustrated for the single point and the multiple point situations. The geometries of the rails and the wheels are approximated from large tables with cubic spline interpolations. For some positions of the wheel set in contact with the rails, the positions of the contact points are computed (possibly for multiple contacts on each wheel). Given these, the ‘penetration’ of the bodies, and a number of other variables are computed: rolling radii, geometrical parameters of the contact points such as curvatures, contact angles, etc. The stiffness between wheel and rail is then defined as being perpendicular to the contact plane, see figure 3.7.

Note that we have until now used the phrase ‘contact *points*’. This

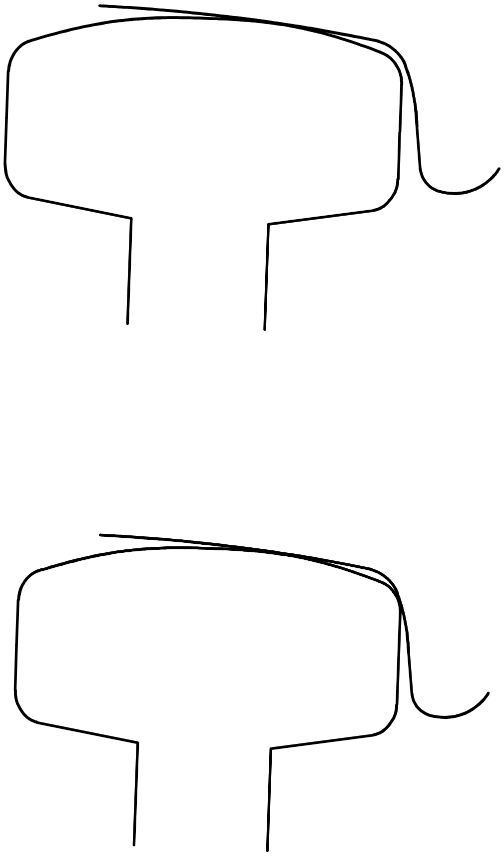

Figure 3.6: Sectional view of a rail and a wheel. Determination of the contact point; single point contact and multiple point contact.

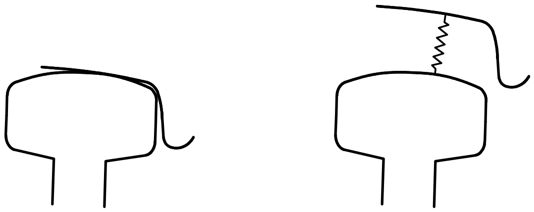

Figure 3.7: Sectional view of a rail and a wheel. The stiffness between wheel and rail is defined as being perpendicular to the contact plane.

is of course a simplification. Let us consider the situation where an infinitely stiff ball performs pure rolling (no sliding) on the surface of an infinitely stiff body. The ball and the body will only touch each other in a point (or in points) and the contact force will thus be a point force (or be point forces). A similar description is not sufficient for modelling the wheel rail contact mechanics. It must be modified. If the assumption of infinite stiffnesses is weakened, the ball and the body will touch each other in a finite area (or in finite areas for multiple 'point' contacts). Hertz studied the static contact problem of two bodies forced together, [24]. Under certain assumptions, he found analytically that the shape of the contact area is elliptical, and that the semi axes are determined by the normal force between the bodies and their curvatures at the 'point of contact'. Hertz's solution can be used to approximate the contact area of a railway wheel on a rail.

However, in contrast to Hertz's problem, the contact problem of a railway wheel and rail is not static. To study the contact forces, a nonlinear three dimensional contact theory is necessary. A lot of effort has been given to this subject. Kalker [29] succeeded in formulating such a theory. It is the general opinion that his contact theory is very good. Unfortunately it would be too complicated to use in dynamic computer simulations. We use an approximation of the theory by Shen, Hedrick and Elkins [39], which we shall now survey. Basically the Shen, Hedrick, Elkins approach modifies the

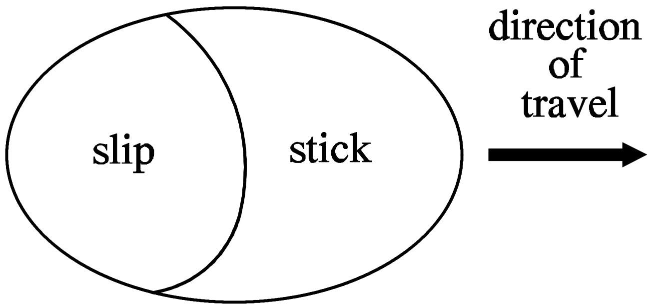

Figure 3.8: The contact area is divided into a slip and a stick region.

linearisation of Kalker's theory by a cubic function such that the resulting frictional force never exceeds the coulomb friction force, μN, where μ is the coefficient of adhesion and N is the normal force.

The contact ellipse is divided into a stick region at the front end with respect to the direction of travel, and a slip region at the rear end with respect to the direction of travel. See figure 3.8. In the stick region the relative velocity between the rail and the wheel is zero; in the slip region there is a finite relative velocity between them. The *creepage*, defined as the relative velocity between the wheel and the rail, normalised with the speed of travel, is introduced. The creepage gives rise to a frictional force, the so called creep force. The creep forces are *very* important for railway dynamics.

Thus we define the longitudinal, the lateral, and the spin creepages, ξ_x, ξ_y and ξ_{sp}. The spin creepage is the projection of the rotation of the wheel on the contact plane, normalised with the speed of travel. The *linear* creep forces in longitudinal and lateral directions, τ_x and τ_y, and the creep torque around the normal of the contact plane, M_x, are then given by the linearisation of Kalker's theory as

$$\begin{bmatrix} \tau_x \\ \tau_y \\ M_z \end{bmatrix} = -G\,c^2 \begin{bmatrix} C_{11} & 0 & 0 \\ 0 & C_{22} & c\ C_{23} \\ 0 & c\,C_{32} & c^2\,C_{33} \end{bmatrix} \begin{bmatrix} \xi_x \\ \xi_y \\ \xi_{sp} \end{bmatrix}. \tag{3.8}$$

G is the shear modulus; c is the geometrical average of the semi axes of the contact ellipse, and $C_{11}, C_{22}, C_{23}, C_{32}$ and C_{33} are parameter dependent coefficients from Kalker's contact theory. The resulting linear creep force is given as

$$\tau_R = \sqrt{\tau_x^2 + \tau_y^2}$$

and the resulting *nonlinear* creep force, T_R, is found by modifying with a cubic function:

$$\frac{T_R}{\mu N} = \begin{cases} u - \frac{1}{3}u^2 + \frac{1}{27}u^3 & \text{for } u < 3 \\ 1 & \text{for } u \geq 3 \end{cases}, \quad u = \frac{\tau_R}{\mu N}. \tag{3.9}$$

Hence, the nonlinear longitudinal and lateral creep forces are given as:

$$T_x = \frac{\tau_x}{\tau_R} T_R \quad \text{and} \quad T_y = \frac{\tau_y}{\tau_R} T_R.$$

These creep forces as well as the normal forces, calculated from the penetrations, are plugged into the equations of the train model. Note that the creep force depends on the normal force. The bridge dynamics enter in the calculation of the normal forces. The vertical deflection of the bridge is taken into account in a straight forward way when the geometrical problem is solved. This, the easiness of including the variation of the track altitude in the model, is another advantage of the flexible model of the wheel-rail contact geometry.

3.3 Train bridge investigation results

3.3.1 Comfort investigations

As mentioned above, one of the aims of the development of the train bridge interaction simulation program in this work, is to use the program for commercial applications. The program has been used

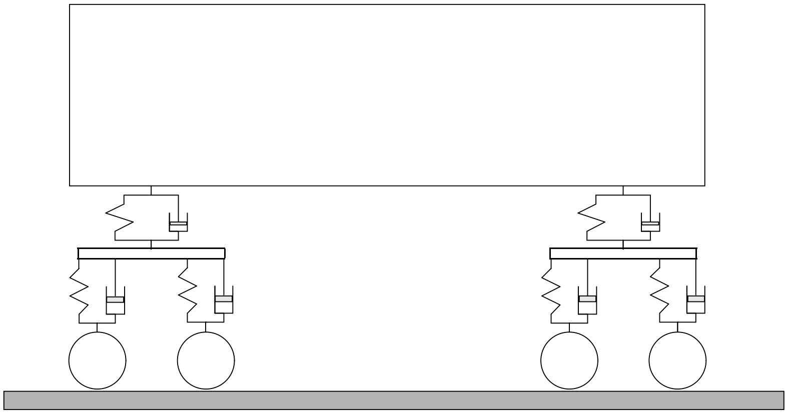

Figure 3.9: The 6 degrees of freedom IC3 car model for comparison with the full 3 dimensional nonlinear IC3 train model.

for investigations of train passenger comfort in trains crossing the future Øresund Link coast to coast connection, [16].

The technique for investigating train passenger comfort under influence of bridge dynamics is rather similar to the technique for investigating train passenger comfort under influence of track irregularities.

For the latter, we have compared the comfort assessment of such investigations, carried out with the full 3 dimensional IC3 train model from subsection 3.2.1 and the much simpler IC3 car model seen in figure 3.9. The single IC3 car is modelled as a 6 degrees of freedom rigid body system, where the 6 degrees of freedom are the vertical displacements of the bogie frames and the car body, and the rotations in the vertical longitudinal plane (pitch motion) of the bogie frames and the car body. The couplings between the wheels and the rails are assumed infinitely stiff — thus the inertia of the wheels is not included in the model. In figures 3.10 and 3.11 comfort simulations from the two approaches are compared. The vertical accelerations of the three car bodies are shown in figure 3.10, and the

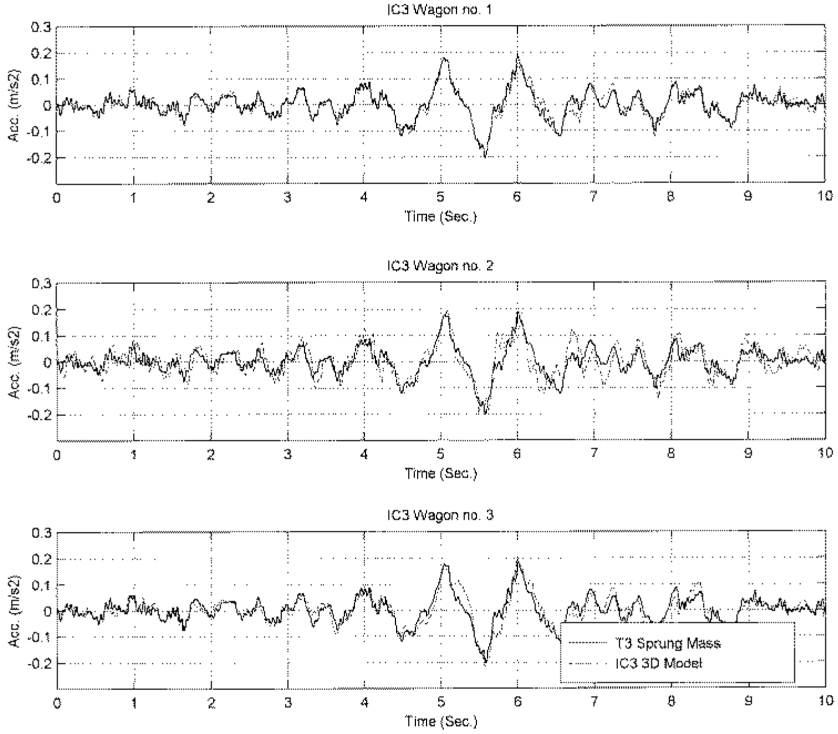

Figure 3.10: Comparison of the vertical accelerations. (- -) 3 dimensional model of IC3 train set; (—) 6DOF model of IC3 vehicle.

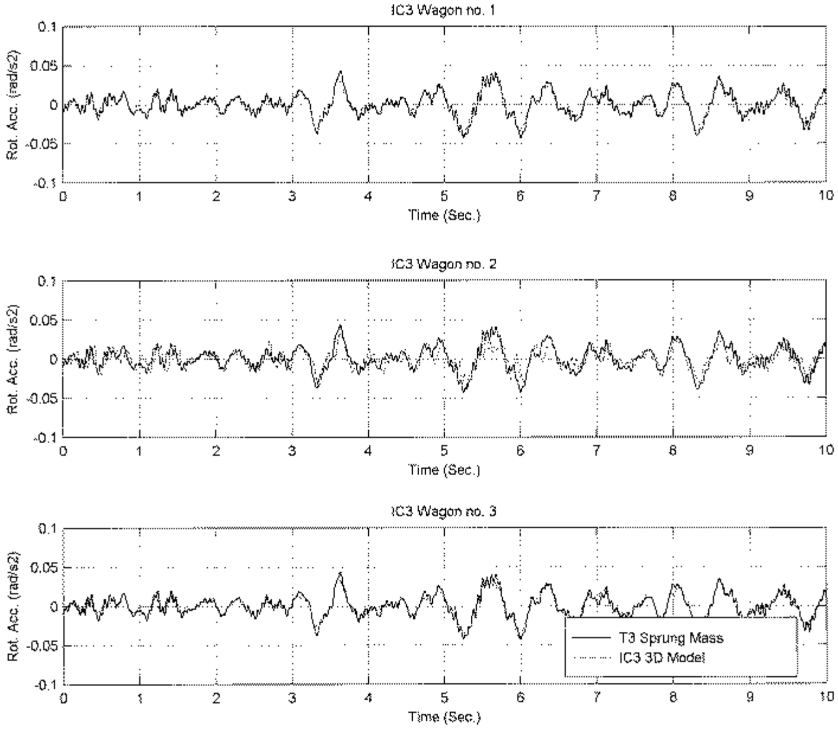

Figure 3.11: Comparison of the rotational acceleration (- -) 3 dimensional model of IC3 train set; (—) 6DOF model of IC3 vehicle.

pitch accelerations of the three car bodies are shown in figure 3.11. The full lines correspond to the results from the investigations with the relatively simple model from figure 3.9, whereas the stabled lines correspond to the results from the investigations with the full 3 dimensional train model. The track irregularities were modelled with a stochastic process represented by a Fröhling spectrum with a rms value of 0.0016 meters and a rms ratio of 2 for the band 40-80 meters to the band 3-40 meters, [17], [16]. It is seen that there is very good agreement between the results from the two different models. There is a bit more discrepancy for car number 2 than for number 1 and 3, which can be explained by the fact that the dynamic characteristics for this wagon differ from those of the simple train model. The investigations showed that the horizontal track irregularities tend to imply greater accelerations of the car bodies than vertical track irregularities. Uncorrelated horizontal track irregularities gave larger car body accelerations than correlated horizontal track irregularities. For vertical track irregularities the picture was opposite: Correlated vertical track irregularities gave larger car body accelerations than uncorrelated vertical track irregularities. Thus the necessity of using the full 3 dimensional IC3 train model instead of the much simpler 6 degrees of freedom model, depends on the objective of the investigation. In our train bridge investigations, the track irregularities are ignored. If only the vertical motion of the bridge deck is considered (i.e. effects due to wind load, earthquakes, etc. on the bridge are not considered), the conclusion of our investigations is that the train passenger comfort investigations can be carried out with the relatively simple train model in figure 3.9. It should be noted that this is an empirical result — we have not proved this conclusion — it may not be valid for higher train speeds, where the nonlinearities of the wheel rail contact become more important. It is our impression, that the discrepancies between the results from the simple and the complex model have *very little* to do with the nonlinearities in the complex model. We would also like to mention that even simpler train models than the one in figure 3.9 have been used although with less satisfactory results. Finally we again mention that we have neglected the flexibility of the car bodies in our investigations. The design of trains goes towards lighter and more flexible car bodies, so we expect that the flexibility must be included in future investigations.

3.3.2 Bridge flexibility and train nonlinearities

Another aim with the train bridge investigations has been to look for phenomena connected to the flexibility of the bridge and the nonlinearities of the train. For this purpose we adopted the cooperrider bogie with realistic rail and wheel profiles.

We have not found particularly interesting effects of the combination of flexibility and nonlinearities. It is our belief, though, that more detailed investigations would reveal train speed and bridge parameter regimes where the bridge dynamics would lead to chaotic or transient chaotic motion of the bogie. However investigations hereof lies beyond the scope of this thesis.

In figure 3.12 we show an example of a comparison of the dynamics of the cooperrider bogie when running on an ideal track and running on a bridge. The graph illustrates the lateral displacement of the rear wheel set as a function of the time. The speed of the simulation is 60 m/s. The initial conditions and the speed is chosen such that the vehiche is running in a hunting motion, a very undesireble state above a certain critical speed of the train. The dashed line is the result of the simulation with the train running on a straight track and the full line is the result of the simulation with the train running on the bridge. It is seen that there is a slight change of the dynamics mainly consisting of a phase shift. However, the general picture of the motion of the wheel set has not changed as an effect of the bridge flexibility in this simulation.

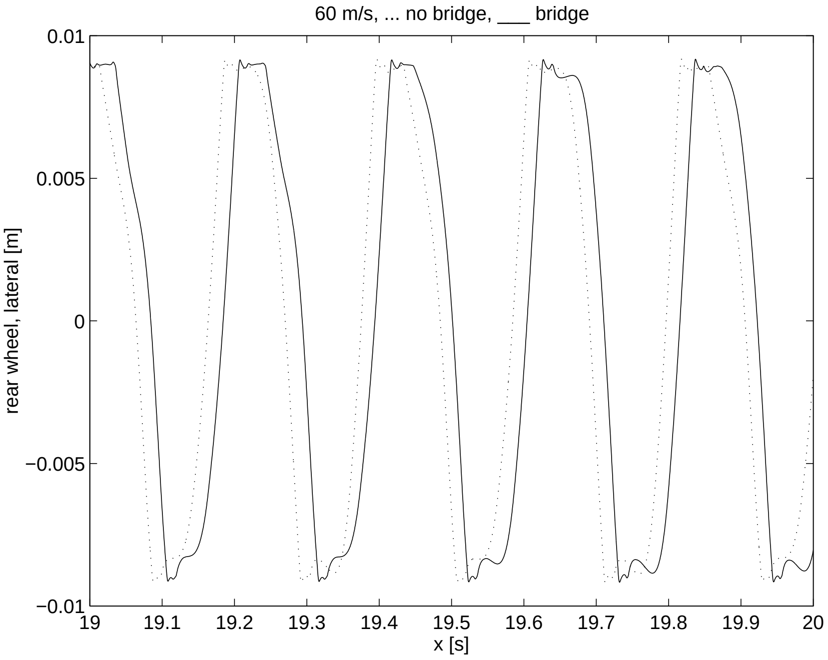

Figure 3.12: Comparison of the lateral motion of the cooperrider bogie: (- -) train running on an ideal straight track; (—) train running on a bridge. It should be noted that the situation described in the figure is the hypothetical and undesirable case of a bogie running in a hunting motion (flutter type instability).

Chapter 4

Pantograph catenary dynamics

The topic of this chapter is the study of the dynamical interaction between pantographs and overhead line systems (or catenary systems). This is by far the example of a 'nonlinear system with discrete and continuous elements' that has taken most of the time and effort of the phd. study during the last 3 years.

An overhead line system is the complex arrangement of cables with support above a railway track, which supplies electrical energy to the traction vehicles in electrical trains. The electrical energy is collected via the pantographs, which are the mechanical devices placed on the roofs of the traction vehicles.

It has become increasingly important to understand and predict the behaviour of an electrical overhead line system interacting with one or more pantographs on a moving train as the train speeds have grown. The problems concerned with this interaction are among the major limitations against further increase of the train speeds. The appearance of contact losses between pantographs and catenary systems is responsible for a considerable amount of wear on both the pantographs and the contact cables. Additionally, the contact losses can result in traction problems, and they may cause electrical disturbances interfering with the runability of other operating trains.

Traditionally, the overhead line systems and the pantographs are designed jointly and are optimised for each other. Different railway companies have had their own design. Concerning the overhead line systems, there basically are the 3 mechanically different systems: the so called simple configuration, the stitched configuration (or Y-configuration), and the compound configuration. Electrically there are the DC overhead line systems, typically with a 3 kV voltage; and there are the AC overhead line systems, typically a 25 kV 50 Hz system, or a 15 kV $16\frac{2}{3}$ Hz system. This scenario with the various catenary system concepts has developed into the situation where the railway companies have sometimes had an almost religious believe in the superiority of precisely *their* system.

With the improvement of the high-speed line network internationally, situations with pantographs optimised for one type of system but operating on another type of system is no longer just of theoretical interest. Now some trains have even had to be designed so that they can operate on 4 electrically different overhead line systems.

The international linking up of railway lines, in particular high speed lines, has increased the importance of being able to understand and predict the dynamics of pantograph overhead line systems.

In this thesis we will only consider the mechanics and the mechanical, dynamical properties of pantograph catenary systems. We shall first be concerned with different traditional modelling approaches and derive our equations of motion of cables. We will study the propagation of pulses in single cable models and compare the importance of the 'small terms' in the cable equations. We will then take a closer look at the different choices of overhead line system configurations and consider some of the design parameters. We will pin out some design details that we find to be important — or that we find *not* to be important after haven studied it. We will give an account of our discretisation of the equations of motion. Afterwards we shall consider the modelling of the pantograph dynamics and the coupling of the pantograph and the catenary system. Finally we will come to the results from our simulations and the conclusions we draw from them.

4.1 Cable equations

The cables in overhead line systems have traditionally been modelled as strings, yielding the linear wave-equation as the equation of motion:

$$\mu v_{tt} = P_0 v_{xx}. \tag{4.1}$$

(4.1) is solved by the so called D'Alembert solution

$$v(x,t) = f\left(x - \sqrt{\frac{P_0}{\mu}}\,t\right) + g\left(x + \sqrt{\frac{P_0}{\mu}}\,t\right), \tag{4.2}$$

if $(f + g)$ fulfils the boundary and the initial conditions. (4.2) describes waves travelling towards right and left without changing shape, with propagation speed(s) $c = \pm\sqrt{\frac{P_0}{\mu}}$. Hereafter we will refer to this speed as the *critical speed.* When the train speed is well below the critical speed, good results are achieved when modelling the cables by the linear string model. For train speeds near and over the critical speed, the string model is believed to give results in poor agreement with reality.

In order to simulate pantograph overhead line dynamics for near-critical and supercritical speeds, the usual approach has then been to include the bending stiffness of the cables in the models, and thus model the cables as Bernoulli-Euler beams. The equations of motion of the cables are then 4th order partial differential equations:

$$\mu v_{tt} = P_0 v_{xx} - EI v_{xxxx}. \tag{4.3}$$

(Sometimes the cables are even modelled as Timoshenko beams, which means that also shear deformations are included.) The results of the simulations with the beam model are in much better agreement with field observations for train speeds approaching the critical speed, [4].

By the nature of the equations of motion for the beam models, longitudinal and transversal motions are decoupled. Furthermore, due to the strong prestress of the cables in overhead line systems, geometrical nonlinearities are normally considered to be negligible.

However, the bending stiffness of a cable *is* very small. To our knowledge, this is the only application of cable dynamics in which the bending stiffness is not believed to be negligible. Remarkably, to our knowledge it is *also* the only application of cable dynamics in which the geometrical nonlinearities are *not* believed to be important to include in the modelling.

We wanted to formulate a model that takes into account the very weak nonlinearities in overhead line systems. Our first approach was to adopt a lumped mass approach for the modelling of the catenary systems, inspired by Scott and Rothman, [38], and by Gostling and Hobbs, [20], where we allowed the lumped masses to move in the vertical plane instead of just vertically as in the above cited papers. A close analysis shows that the continuous limit of the equations of motion of one cable modelled this way is the system of nonlinear equations of motion of a string in 2 dimensions.

However instead of this rather nasty course of action, we will deduce the equations with a Lagrange procedure. We will consider a cable that is nearly horizontal, such that we can assume that the independent spatial variable x and the arc length of the cable s are close to being equal. Then let $v(x,t)$ and $u(x,t)$ be the variables describing the vertical and the longitudinal deflections of the cable. Let μ, P_0, EI and EA be the mass per length, the prestress force, the bending stiffness and the flexural stiffness of the cable, and let the cable have length L. Let ϵ and κ be the strain and the curvature

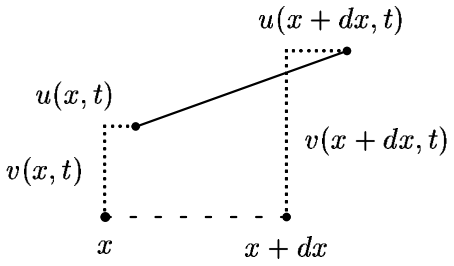

Figure 4.1: An infinitesimal piece of the cable.

of the cable. The potential energy of the cable can then be written as

$$U = \int_0^L \frac{EI}{2}\kappa^2\, dx + \int_0^L \left(P_0\epsilon + \frac{EA}{2}\epsilon^2\right)\, dx. \tag{4.4}$$

The strain, ϵ, of the cable is found from figure 4.1 as:

$$\epsilon(x,t) = \frac{\sqrt{(dx+u(x+dx,t)-u(x,t))^2+(v(x+dx,t)-v(x,t))^2}-dx}{dx} \approx$$
$$\sqrt{\left(1+\frac{\partial u}{\partial x}\right)^2+\left(\frac{\partial v}{\partial x}\right)^2}-1 \approx \frac{\partial u}{\partial x}+\frac{1}{2}\left(\frac{\partial v}{\partial x}\right)^2,$$

and since the curvature can be approximated by

$$\kappa \approx \frac{\partial^2 v}{\partial x^2}$$

we rewrite the potential energy as

$$\begin{aligned} U = \int_0^L \tfrac{EI}{2}\left(\tfrac{\partial^2 v}{\partial x^2}\right)^2 dx + \int_0^L P_0\left(\tfrac{\partial u}{\partial x}+\tfrac{1}{2}\left(\tfrac{\partial v}{\partial x}\right)^2\right) dx+ \\ \int_0^L \tfrac{EA}{2}\left(\tfrac{\partial u}{\partial x}+\tfrac{1}{2}\left(\tfrac{\partial v}{\partial x}\right)^2\right)^2 dx. \end{aligned} \tag{4.5}$$

The kinetic energy is given as

$$T = \int_0^L \frac{1}{2}\mu\left(\left(\frac{\partial u}{\partial t}\right)^2+\left(\frac{\partial v}{\partial t}\right)^2\right)\, dx. \tag{4.6}$$

We define the lagrangian density as

$$\mathcal{L} = \frac{\mu}{2}\left(u_t^2 + v_t^2\right) - \frac{EI}{2}v_{xx}^2 - P_0\left(u_x + \frac{1}{2}v_x^2\right) - \frac{EA}{2}\left(u_x + \frac{1}{2}v_x^2\right)^2,$$

where we have changed the notation a little for the convenience. Lagrange's equations, see [21] or [19], state that we by variation can get the equations of motion as the equations found by evaluating:

$$\begin{aligned} -\tfrac{d}{dt}\tfrac{\partial\mathcal{L}}{\partial v_t} - \tfrac{d}{dx}\tfrac{\partial\mathcal{L}}{\partial v_x} + \tfrac{d^2}{dx^2}\tfrac{\partial\mathcal{L}}{\partial v_{xx}} &= 0 \\ -\tfrac{d}{dt}\tfrac{\partial\mathcal{L}}{\partial u_t} - \tfrac{d}{dx}\tfrac{\partial\mathcal{L}}{\partial u_x} &= 0. \end{aligned}$$

Doing this, our equations of motion for the cable becomes

$$\begin{aligned} \mu v_{tt} &= P0 v_{xx} - EI v_{xxxx} + EA\left(v_x u_{xx} + v_{xx}u_x + \tfrac{3}{2}v_x^2 v_{xx}\right) \\ \mu u_{tt} &= EA u_{xx} + EA v_x v_{xx}. \end{aligned} \tag{4.7}$$

Please note that (4.7) differs from (4.3) by the inclusion of the longitudinal motion (the second equation in (4.7)), the terms for the nonlinear coupling of the vertical motion to the longitudinal motion, $v_x u_{xx}$ and $v_{xx} u_x$, and the geometrical nonlinearity term, $\frac{3}{2}v_x^2 v_{xx}$.

Given the physical parameters and general behaviour of cables, considering only vertical excitation, and noting that, in the equation for the longitudinal motion, the coupling term to the vertical motion is $v_x v_{xx}$, a qualified guess is that the longitudinal motion is of order 2 in the vertical motion, $u = \mathcal{O}(v^2)$. However, since we are dealing with *differential* equations with terms containing *derivatives* of v and u, their mutual ratio is not quite clear. We shall reflect on this in section 4.2.2, where we deal with the numerical pulse propagation results.

If we assume that the longitudinal motion *is* of order 2 in the vertical motion, we find that — apart for the inclusion of a term for the bending stiffness — (4.7) is the Taylor expansion to third order of the 2 dimensional nonlinear string equation, [34]. (4.7) will be our basic equations for the cable motions.

Compared to the linear prestress term, $P_0 v_{xx}$, the bending term, $-EIv_{xxxx}$, the nonlinear coupling terms, $EA(v_x u_{xx} + v_{xx} u_x)$, and the geometrical nonlinearity term $\frac{3}{2}EAv_x^2 v_{xx}$, are all small terms. We will refer to these as the 'small terms' in the remainder of this chapter.

4.2 Wave propagation investigations

We want to study the influence on propagation of waves of the 'small terms' in the cable equations (4.7), i.e. the influence of the bending stiffness, the nonlinear coupling of the vertical to the longitudinal motions, and the geometrical nonlinearity. For that purpose we adopt 2 alternatives to (4.7): First we assume that the bending stiffness can be neglected, $EI = 0$, and that the longitudinal motion is of order 3 in the vertical motion, $u = \mathcal{O}(v^3)$. Note that according to our remarks above, the latter assumption is rather critical. Anyway, by making these assumptions and expanding (4.7) to third order in v, the equations for the vertical and longitudinal motions decouple, and the equation for the vertical motion becomes:

$$\mu v_{tt} = P0 v_{xx} + \frac{3}{2}EAv_x^2 v_{xx}. \tag{4.8}$$

The second alternative to equation (4.7) is as (4.8), but with the bending stiffness taken into account:

$$\mu v_{tt} = P0 v_{xx} - EIv_{xxxx} + \frac{3}{2}EAv_x^2 v_{xx}. \tag{4.9}$$

We shall perform investigations of propagation of pulses in the three cable equations (4.7), (4.8) and (4.9).

Note that all our wave propagation investigations neglect the effect of damping.

4.2.1 The method of characteristics

Equation (4.8) can be solved analytically by the method of characteristics, see [44]. We define the new variables $u1 = v_x$ and $u2 = v_t$, and the new constants $\gamma_1^2 = \frac{P_0}{\mu}$ and $\gamma_2^2 = \frac{EA}{\mu}$. (4.8) can now be rewritten as 2 coupled first order partial differential equations:

$$\begin{bmatrix} u1_t \\ u2_t \end{bmatrix} + \begin{bmatrix} 0 & -1 \\ -(\gamma_1^2 + \frac{3}{2}\gamma_2^2 u1^2) & 0 \end{bmatrix} \begin{bmatrix} u1_x \\ u2_x \end{bmatrix} = \begin{bmatrix} 0 \\ 0 \end{bmatrix}$$

We can manipulate these to their characteristic form:

$$\begin{aligned} &u1_t + \sqrt{\gamma_1^2 + \tfrac{3}{2}\gamma_2^2 u1^2}\,u1_x - \\ &\qquad \frac{1}{\sqrt{\gamma_1^2 + \frac{3}{2}\gamma_2^2 u1^2}}\left(u2_t + \sqrt{\gamma_1^2 + \tfrac{3}{2}\gamma_2^2 u1^2}\,u2_x\right) = 0 \\ &u1_t - \sqrt{\gamma_1^2 + \tfrac{3}{2}\gamma_2^2 u1^2}\,u1_x + \\ &\qquad \frac{1}{\sqrt{\gamma_1^2 + \frac{3}{2}\gamma_2^2 u1^2}}\left(u2_t - \sqrt{\gamma_1^2 + \tfrac{3}{2}\gamma_2^2 u1^2}\,u2_x\right) = 0. \end{aligned} \tag{4.10}$$

In the x-t-plane we define the *characteristics* C^+ and C^-:

$$\begin{aligned} C^+ : \quad \tfrac{dx}{dt} &= \sqrt{\gamma_1^2 + \tfrac{3}{2}\gamma_2^2 u1^2} \\ C^- : \quad \tfrac{dx}{dt} &= -\sqrt{\gamma_1^2 + \tfrac{3}{2}\gamma_2^2 u1^2}. \end{aligned} \tag{4.11}$$

We denote them as positive respectively negative characteristics, referring to their slope in the x-t-plane. We have:
Along C^+

$$\begin{aligned} \tfrac{du1}{dt} &= \tfrac{\partial u1}{\partial t} + \tfrac{\partial u1}{\partial x}\tfrac{dx}{dt} = u1_t + \sqrt{\gamma_1^2 + \tfrac{3}{2}\gamma_2^2 u1^2}\,u1_x \\ \tfrac{du2}{dt} &= \tfrac{\partial u2}{\partial t} + \tfrac{\partial u2}{\partial x}\tfrac{dx}{dt} = u2_t + \sqrt{\gamma_1^2 + \tfrac{3}{2}\gamma_2^2 u1^2}\,u2_x \end{aligned}$$

and
Along C^-:

$$\begin{aligned} \tfrac{du1}{dt} &= \tfrac{\partial u1}{\partial t} + \tfrac{\partial u1}{\partial x}\tfrac{dx}{dt} = u1_t - \sqrt{\gamma_1^2 + \tfrac{3}{2}\gamma_2^2 u1^2}\,u1_x \\ \tfrac{du2}{dt} &= \tfrac{\partial u2}{\partial t} + \tfrac{\partial u2}{\partial x}\tfrac{dx}{dt} = u2_t - \sqrt{\gamma_1^2 + \tfrac{3}{2}\gamma_2^2 u1^2}\,u2_x. \end{aligned}$$

Thus, on the positive characteristics, the first partial differential equation in (4.10) reduces to the ordinary differential equation:

$$\frac{du1}{dt} - \frac{1}{\sqrt{\gamma_1^2 + \frac{3}{2}\gamma_2^2 u1^2}} \frac{du2}{dt} = 0, \tag{4.12}$$

and on the negative characteristics, the second partial differential equation in 4.10 reduces to the ordinary differential equation:

$$\frac{du1}{dt} + \frac{1}{\sqrt{\gamma_1^2 + \frac{3}{2}\gamma_2^2 u1^2}} \frac{du2}{dt} = 0. \tag{4.13}$$

Simple manipulations with (4.12) and (4.13) yield

$$\sqrt{\gamma_1^2 + \frac{3}{2}\gamma_2^2 u1^2} du1 - du2 = 0 \tag{4.14}$$

along C^+, and

$$\sqrt{\gamma_1^2 + \frac{3}{2}\gamma_2^2 u1^2} du1 + du2 = 0 \tag{4.15}$$

along C^-. By integration we achieve the *Riemann invariants*:

$$\frac{u1\sqrt{\gamma_1^2 + \frac{3}{2}\gamma_2^2 u1^2}}{2} + \frac{\sqrt{6}\gamma_1^2}{6\gamma_2} \ln\left(\sqrt{\frac{3}{2}}\gamma_2 u1 + \sqrt{\gamma_1^2 + \frac{3}{2}\gamma_2^2 u1^2}\right) - u2 = J_+ \tag{4.16}$$

along C^+ and

$$\frac{u1\sqrt{\gamma_1^2 + \frac{3}{2}\gamma_2^2 u1^2}}{2} + \frac{\sqrt{6}\gamma_1^2}{6\gamma_2} \ln\left(\sqrt{\frac{3}{2}}\gamma_2 u1 + \sqrt{\gamma_1^2 + \frac{3}{2}\gamma_2^2 u1^2}\right) + u2 = J_- \tag{4.17}$$

along C^-. Thus, along a positive characteristic, the rather nasty looking expression on the left hand side in (4.16) is constant. Similarly, along a negative characteristic, the (equally nasty) expression on the left hand side in (4.17) is constant. We refer to these constants as the positive respectively the negative Riemann invariants

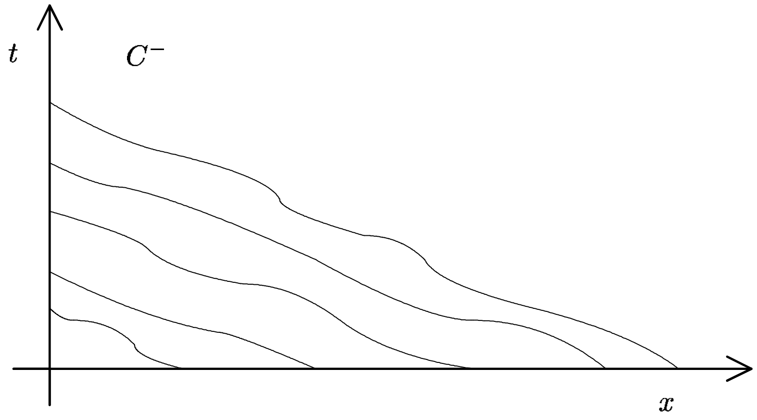

Figure 4.2: All negative characteristics will cross the x-axis.

(with the obvious origin of the distinction). Note that *each* positive (negative) characteristic attaches to a positive (negative) Riemann invariant.

Let us consider a system given by $x \geq 0, t \geq 0$, and where $u1 = 0$, $u2 = 0$ at $t = 0$. The trick is that since the negative characteristics have negative slope in the x-t-plane, they will all cross the x-axis (at which t=0). See figure 4.2. By inserting $u1 = u2 = 0$ in (4.17) we find that *all the negative Riemann invariants have the same value*, i.e. they are all equal to the constant

$$\frac{\sqrt{6}\gamma_1^2}{6\gamma_2}\ln(\gamma_1) = J_-. \tag{4.18}$$

We can therefore rewrite (4.17):

$$\frac{u1\sqrt{\gamma_1^2+\frac{3}{2}\gamma_2^2 u1^2}}{2} + \left(\frac{\sqrt{6}\gamma_1^2}{6\gamma_2}\ln\left(\sqrt{\frac{3}{2}}\gamma_2 u1 + \sqrt{\gamma_1^2+\frac{3}{2}\gamma_2^2 u1^2}\right) - \ln(\gamma_1)\right) + u2 = 0 \tag{4.19}$$

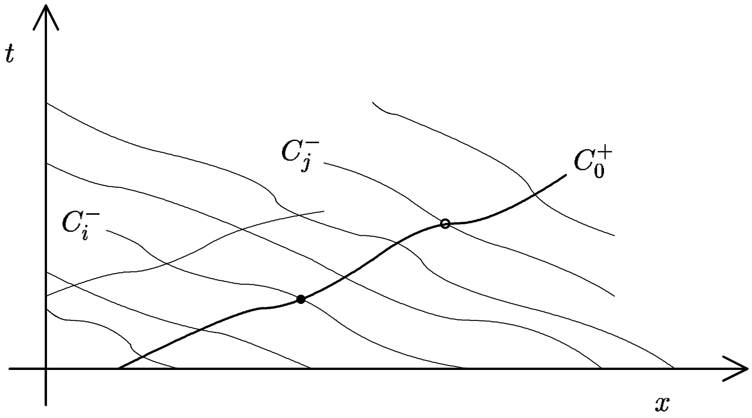

Figure 4.3: We study the behaviour along a specific positive characteristic, C_0^+. C_i^- and C_j^- are negative characteristics crossing C_0^+.

which is valid along C^-.

Now look at the behaviour along a specific positive characteristic, C_0^+. We study a point where this characteristic crosses a specific negative characteristic, C_i^-. See figure 4.3. In this point, we can get an expression for the positive Riemann invariable $J_{+,0i}$ by adding (4.16) and (4.19); we get:

$$\begin{gathered}u1\sqrt{\gamma_1^2+\tfrac{3}{2}\gamma_2^2 u1^2}+\\ \tfrac{\sqrt{6}\gamma_1^2}{6\gamma_2}\left(2\ln\left(\sqrt{\tfrac{3}{2}}\gamma_2 u1+\sqrt{\gamma_1^2+\tfrac{3}{2}\gamma_2^2 u1^2}\right)-\ln(\gamma_1)\right)=J_{+,0i}.\end{gathered} \tag{4.20}$$

At a point where C_0^+ crosses *another* negative characteristic, say C_j^-, we can the same way get an expression for $J_{+,0j}$. But since all the negative Riemann invariants are equal, the expressions for $J_{+,0i}$ and $J_{+,0j}$ are identical. In fact, we will find the *same* expression for the positive Riemann invariant $J_{+,0}$ every time it crosses a negative characteristic — which is all the time. $J_{+,0}$ is equal to this expression all the way along C_0^+. Studying this expression, (4.20), we see that the only variable appearing in it is $u1$. The only way this expression can then be constant along C_0^+ is for $u1 = constant$. We conclude that $u1$ is constant along a positive characteristic.

Lets again study the point where C_0^+ crosses the negative characteristic C_i^-, figure 4.3. Instead of adding, we subtract (4.19) from (4.16). We get the expression

$$-2u2 + \frac{\sqrt{6}\gamma_1^2}{6\gamma_2}\ln(\gamma_1) = J_{+,0i}. \tag{4.21}$$

Corresponding to the arguments above, we realise that we will get the same expression in all the points where C_0^+ crosses a negative characteristic. Since the only variable in (4.21) is $u2$, we conclude that $u2 = constant$ along C_0^+.

From the definition of the positive characteristics (4.11) we see that — since $u1$ is constant along the positive characteristics — *the positive characteristics ar straight lines.*

Lets summarize: We know that the positive characteristics are straight lines and that $u1$ and $u2$ are constant along the positive characteristics. This means that, for the assumed initial values $u1 = u2 = 0$, we have solved (4.8) once and for all. Because if we know the boundary values for $x = 0$, we can simply use the positive characteristics to prescribe the values of $u1$ and $u2$ along these straight lines in the x-t-plane. See figure 4.4. Note that another initial condition would complicate the argumentation but not change the essence of the analysis.

We will illustrate the analytical solution by letting a pulse propagate on a cable described by the equation (4.8). We choose the physical parameters according to the typical data for a contact cable in the overhead line systems in Denmark, i.e.$\mu = 0.91\ kg/m$, $P_0 = 12000\ N$, and $EA = 1.24 \cdot 10^7\ N$. (However we will consider the cable as infinitely long. This is just for convenience, a finite length would not change the essence of the result.)

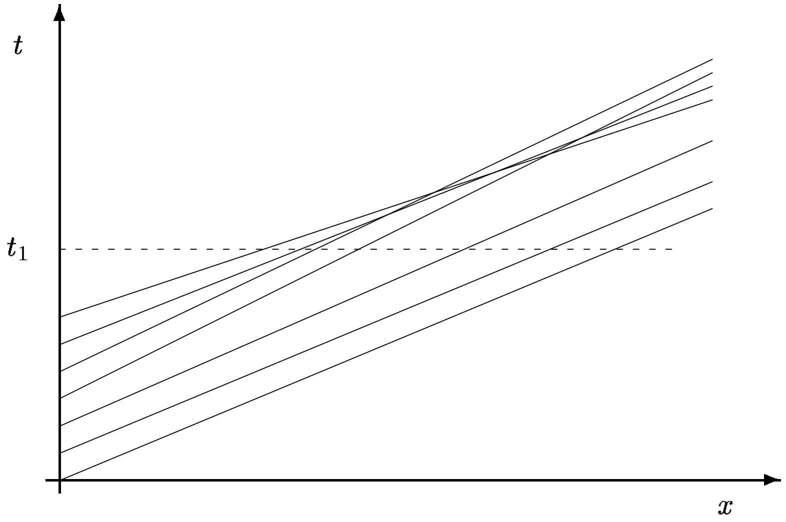

Figure 4.4: Positive characteristics. Knowing the boundary conditions at $x = 0$, these can be used to prescribe the solution at some time t_1, by utilizing that the positive characteristics are straight lines, and that $u1$ and $u2$ are constant on the positive characteristics.

We will study a pulse that initially is a solution to the linearisation of (4.8) (which is just the linear string equation (4.1)) given by

$$v(x,t) = 0.1\text{sech}^4\left(\frac{x+100-\sqrt{\frac{P_0}{\mu}}t}{30}\right).$$

This is a nice, smooth, low amplitude pulse with relatively long length. The pulse is chosen this way because these dimensions are conjectured to be realistic and relevant for pantograph overhead line systems. We have also carried out investigations with other pulses without finding important differences. Therefore we will not illustrate any results from the investigations of pulses with other dimensions.

$u1$ is then initially given by differentiating, ($u1 = v_x$):

$$u1(x,t) = \frac{4\cdot 0.1}{30}\text{sech}^4\left(\frac{x+100-\sqrt{\frac{P_0}{\mu}}t}{30}\right)\tanh\left(\frac{x+100-\sqrt{\frac{P_0}{\mu}}t}{30}\right).$$

The boundary condition at $x = 0$ is given by inserting $x = 0$:

$$v(0,t) = 0.1\text{sech}^4\left(\frac{100-\sqrt{\frac{P_0}{\mu}}t}{30}\right) \tag{4.22}$$

thus

$$u1(0,t) = \frac{1}{75}\text{sech}^4\left(\frac{100-\sqrt{\frac{P_0}{\mu}}t}{30}\right)\tanh\left(\frac{100-\sqrt{\frac{P_0}{\mu}}t}{30}\right). \tag{4.23}$$

The analytical solution found above is now used to prescribe the values of u1 along the positive characteristics given by (4.11) and the boundary condition (4.23). In figure 4.5 we illustrate the analytical solution of $u1$ for $t = 3$ s, $t = 13$ s, $t = 24$ s, $t = 34$ s, and $t = 44$ s. We see that after short time of propagation of the pulse (or rather:

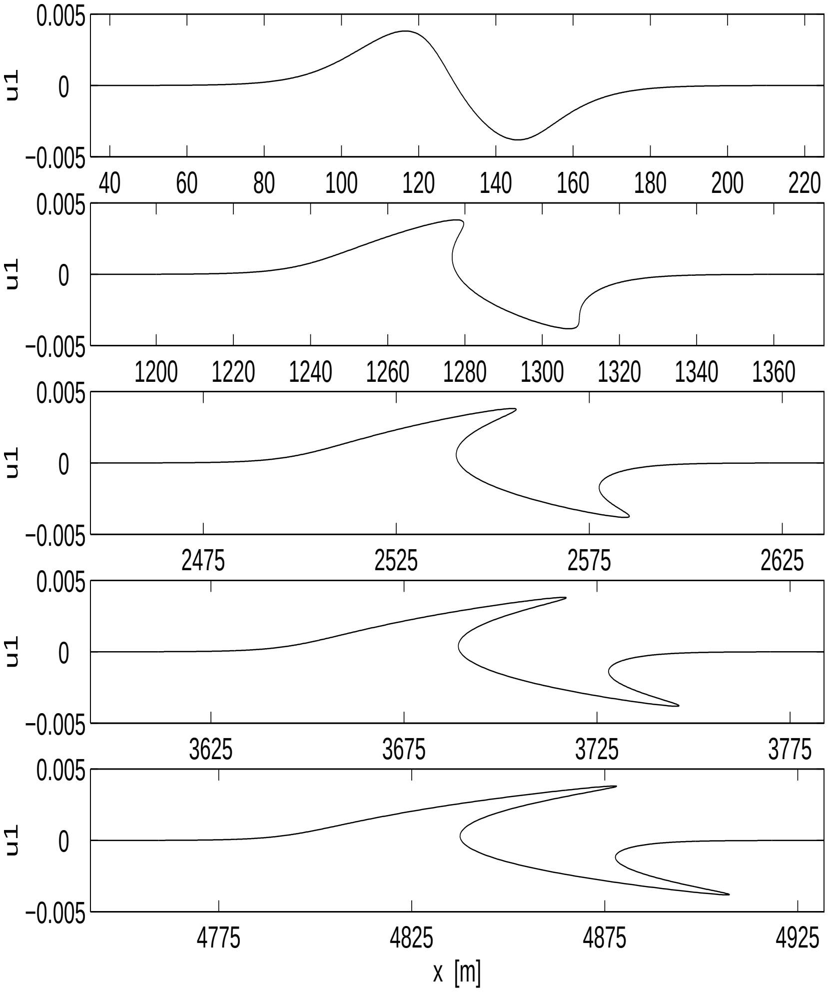

Figure 4.5: The analytical solution of (4.10) with the initial condition $u1 = u2 = 0$, and the boundary condition (4.23) for $t = 3\ s$, $t = 13\ s$, $t = 24\ s$, $t = 34\ s$, and $t = 44\ s$.

of propagation of the derivative of the pulse), a multiple solution situation occurs; i.e. for some x-values, three $u1$-values are prescribed simultaneously. In the second graph ($t = 13\ s$) there is one such multiple solution situation — in the third, fourth, and fifth graphs ($t = 23\ s$, $t = 34\ s$, and $t = 44\ s$) there are two such multiple solution situations. These are examples of so called *shocks*. A shock is a nonlinear wave phenomenon. Loosely speaking, the development of a shock is caused by the fact that, due to the nonlinearities, waves with different wave lengths travel with different speeds (and a pulse can be expanded in a sum of cosine waves with different wave lengths).

In figure 4.4 we already indicated the development of a shock; in the figure it is seen that the characteristics cross at some point. This is exactly what happens when a shock appears.

Note that the first shock develops within a realistic length of a contact cable in an overhead line system. I.e. the shock appears already in the second graph, centred at approximately $x = 1280\ m$. In Denmark the typical length of a contact cable in an overhead line system is $1600\ m$.

Of course the multiple solution situation does not make sense from a physical point of view. A cable can not in some interval have more than one slope at the same time. However, a proper interpretation of the multiple solution situation may lead to important conclusions about the physics. The most obvious way to handle the multiple solution situation is by introducing a discontinuity. This is illustrated in figure 4.6 for our example at $t = 13\ s$. The location of the discontinuity should be chosen so that the two coated areas (limited by the full line and the dashed line) in figure 4.6 have the same size.

Performing such a 'discontinuisation' of our analytical solution, we obtain figure 4.7, which shows $u1$ for $t = 3\ s$, $t = 13\ s$, $t = 24\ s$, $t = 34\ s$, and $t = 44\ s$. Compare with figure 4.5.

We obtain the analytical solution of (4.8) for the given boundary condition, (4.22), and initial condition, $u(x, 0) = 0$, by simply integrating the corresponding result for $u1$. The result is illustrated

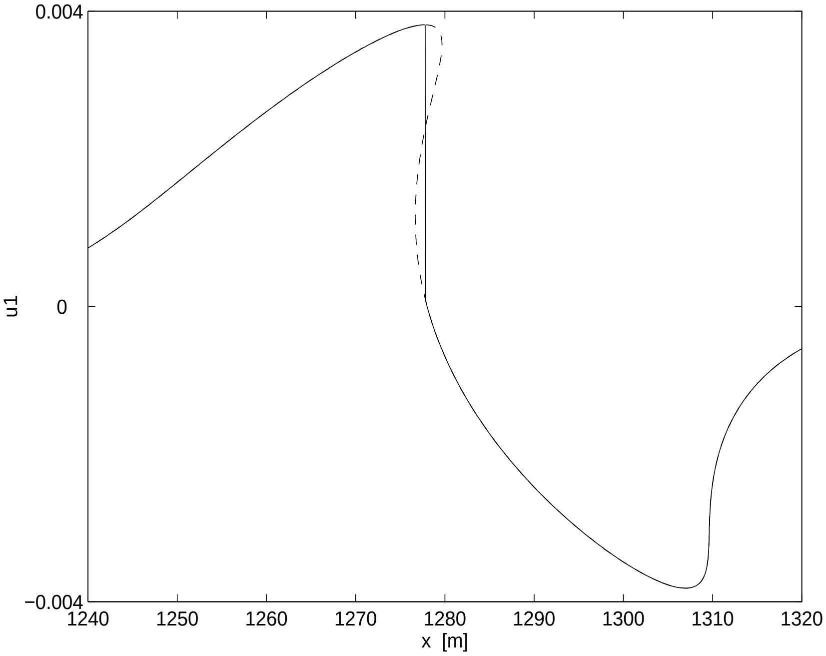

Figure 4.6: Introduction of a discontinuity as a proper way of dealing with the multiple solution situation.

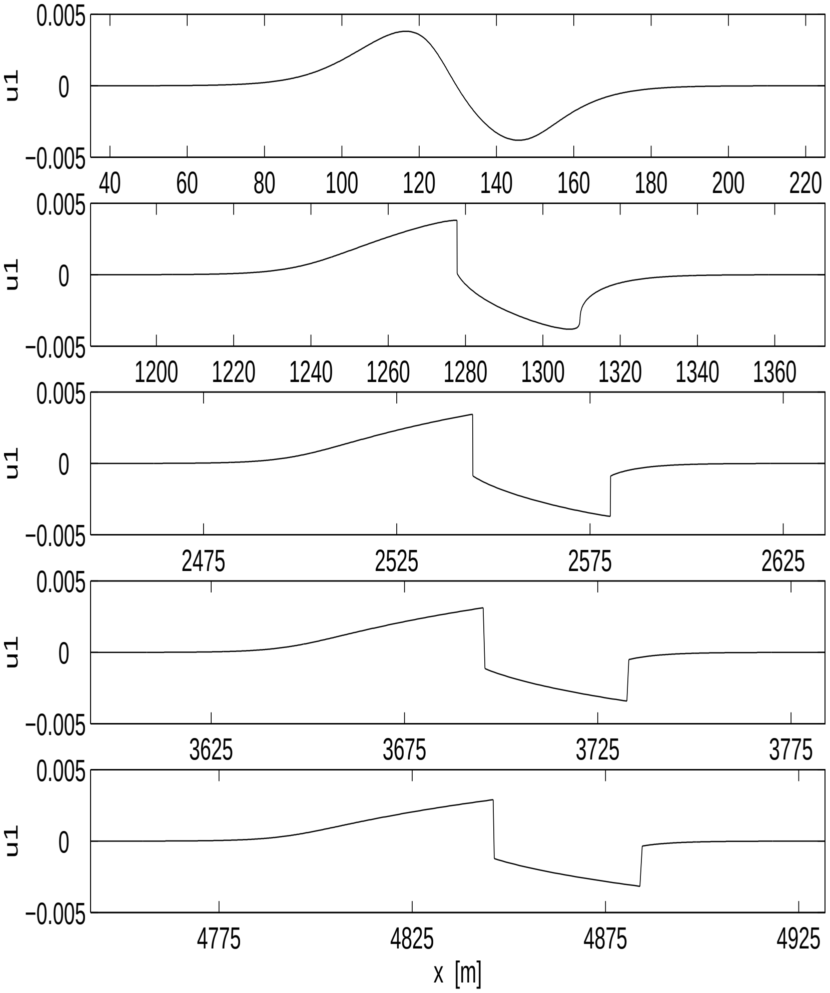

Figure 4.7: The 'discontinuised' analytical solution of (4.10) with the initial condition $u1 = u2 = 0$, and the boundary condition (4.23) for $t = 3\ s$, $t = 13\ s$, $t = 24\ s$, $t = 34\ s$, and $t = 44\ s$. Compare with fig 4.5.

in figure 4.8. Note that the shocks appear as discontinuities in the slope of the cable.

In figure 4.9 we compare the analytical solution of (4.8) with the corresponding (analytical) solution of the linearisation of (4.8), which is just the translated initial pulse (the D'Alembert solution of the linear wave equation).

One of our assumptions to achieve the cable equation (4.8) was that the bending stiffness can be neglected. However, our analytical result reveals the development of shocks, where the shocks appear as discontinuities in in the slope of the cable. Certainly the assumption of zero bending stiffness is not valid in the vicinity of such shocks. We will study the propagation of a pulse with (4.9) as cable equation, where the bending stiffness has a finite value.

Before proceeding to this, let us refer to appendix A in which we derive a nonlinear dispersion relation for (4.8).

4.2.2 Numerical pulse propagation investigations

As mentioned above we would like to proceed now with numerical investigations. The simplified cable equation (4.8) was nice because we were able to use analytical tools to investigate it. However, those analyses gave results that were not consistent with the assumptions for the equation. The zero bending stiffness assumption was not in harmony with the appearance of the discontinuities in the slope of the cable; or rather, with the appearance of the discontinuities in the slope, the assumption of negligible bending stiffness certainly was not valid anymore. Unfortunately, one of the effects of including the bending stiffness in the description is that the equation can no longer be solved analytically; i.e. we turn to numerics.

All our numerical pulse propagation investigations have been performed with finite difference methods. We have investigated the importance of the spatial discretisation fineness to get hand of the numerical errors in the simulations. The cable data are the same as

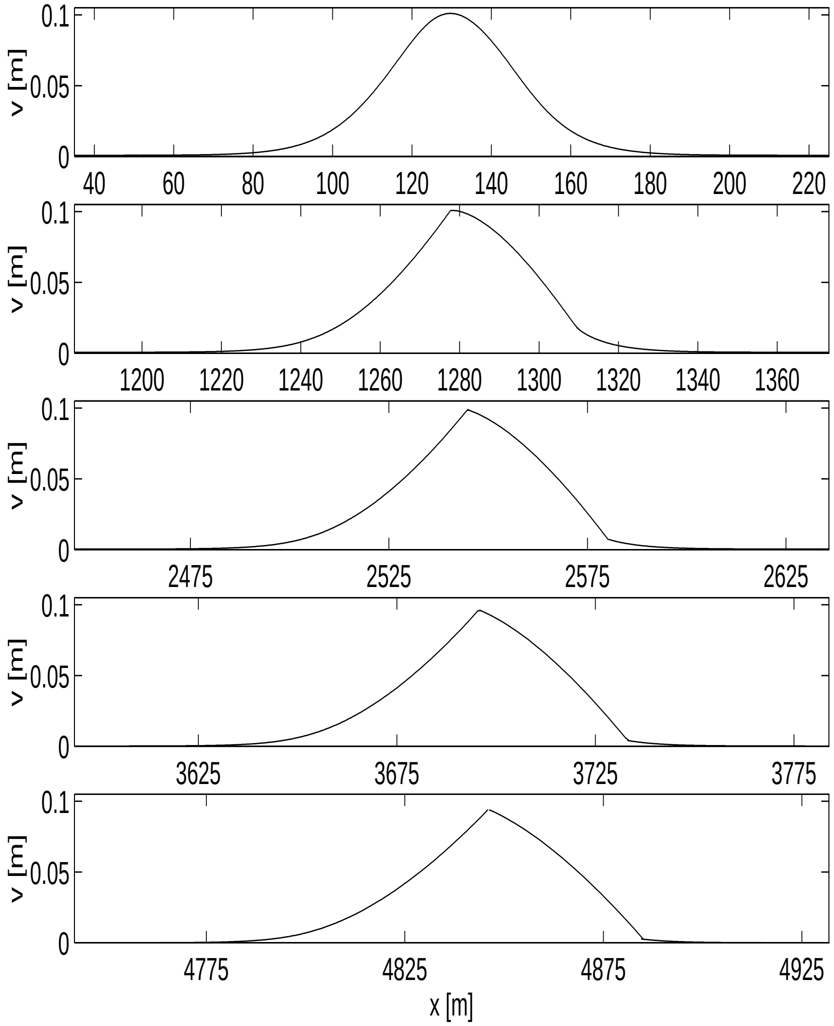

Figure 4.8: The development of shocks in the analytical solution of (4.8) with initial condition $u(x, 0) = 0$ and boundary condition given by (4.22), for $t = 3\ s$, $t = 13\ s$, $t = 24\ s$, $t = 34\ s$, and $t = 44\ s$, corresponding to fig 4.7 after an integration.

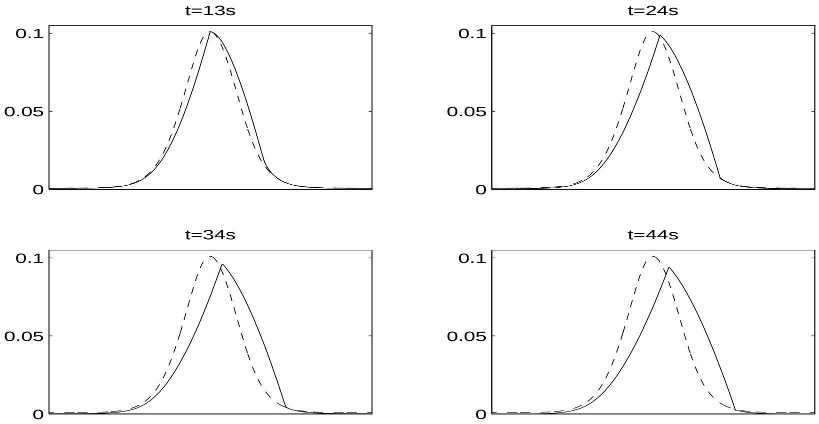

Figure 4.9: Comparison of the development of a pulse propagating according to (4.8) (full line), and propagating according to the linearisation of (4.8) (dashed line).

listed in section 4.2.1, repeated here for completeness: $P_0 = 12000\ N$, $\mu = 0.91\ kg/m$, and $EA = 1.24 \cdot 10^7\ N$. Of course the length of the cable has to be finite in numerical investigations. In some investigations we have used a simply supported cable with the length $L = 1560\ m$, but in those investigations where a very fine discretisation grid was necessary, we have adopted a cable of length $L = 200\ m$ and periodic boundary conditions, $v(0,t) = v(L,t)$, $v_x(0,t) = v_x(L,t)$, $v_{xx}(0,t) = v_{xx}(L,t)$, $u(0,t) = u(L,t)$, and $u_x(0,t) = u_x(L,t)$.

First we will illustrate the numerical investigation corresponding to the analytical result from last section. Figure 4.10 shows the numerical simulation of the propagating pulse at $t = 3\ s$, $t = 13\ s$, $t = 24\ s$, $t = 34\ s$, and $t = 44\ s$. (Compare with the analytical result in figure 4.8.) This is one of the simulations where a cable length of $L = 200\ m$ and periodic boundary conditions have been used. Since (4.8) is hyperbolic, and all disturbances thus propagate with a finite velocity, we believe this is a proper procedure. Note that we in the illustration have adjusted for the finite length of the simulated cable, to be able to compare with figure 4.8. Note also that there is great correspondence between the numerical and the analytical result. In the analytical analysis we had to deal with the multiple solution situation. We found that a proper handling of these situations revealed the shocks as discontinuities in the slope of the cable. In the numerical simulation, the discretisation introduces numerical dispersion by which multiple solution situations are avoided. This may however introduce other errors and a very fine discretisation grid has had to be used in the simulation. Therefore the cable length of just $L = 200\ m$. Note that with the discretisation fineness we have used, the discontinuities in the slope of the cables also appear in the numerical simulation.

We now proceed to perform a numerical investigation of the propagation of a pulse on a cable described by (4.9), in which the bending stiffness is also included. The result of this simulation turned out to be very sensitive to the discretisation fineness. To be able to control the numerical dispersion it was necessary to go to so extreme discretisation fineness that a cray computer was necessary to perfom the simulation. Due to the fine discretisation grid, we also in this investigation used a cable length of $L = 200\ m$ and periodic boundary conditions (except when initiating the pulse, which was initiated by varying $v(0, t)$. During this initiation, simple boundary conditions were applied). We have chosen to neglect that (4.9) is not hyperbolic and any effects this might have. In figure 4.11 the propagation of the pulse on a cable described by equation (4.9) is illustrated for $t = 3\ s$, $t = 13\ s$, $t = 24\ s$, $t = 34\ s$, and $t = 44\ s$. It is seen that the discontinuities in the slope, appearing in figure 4.10, in figure 4.11 have been smoothed somewhat out. However, the *overall* picture is unchanged. The basic deformation of the pulse shape is only slightly dependent on the inclusion of the bending stiffness. Note the small oscillations in front of the pulse and in the front end of the pulse. These persist for decreasing spatial step sizes. We tend to believe that these oscillations are physical and not just some numerical discrepancy.

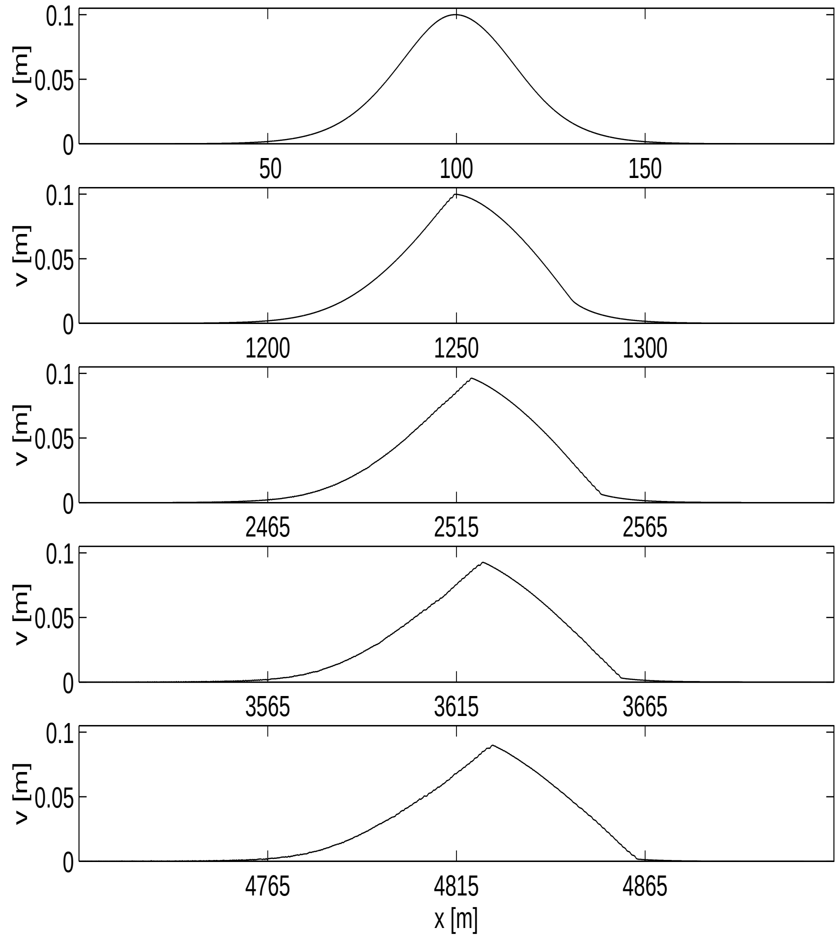

Figure 4.10: The development of shocks in the numerical solution of (4.8). The initial condition is $u(x, 0) = 0$; the boundary condition is given by (4.22) supplied by $v_{xx}(0, t) = v(L, t) = v_{xx}(L, t) = 0$ for $t \leq 200\sqrt{\frac{\mu}{P_0}}$, and is periodic for $t > 200\sqrt{\frac{\mu}{P_0}}$. Snapshots at $t = 3$ s, $t = 13$ s, $t = 24$ s, $t = 34$ s, and $t = 44$ s, corresponding to the analytical result in fig 4.8.

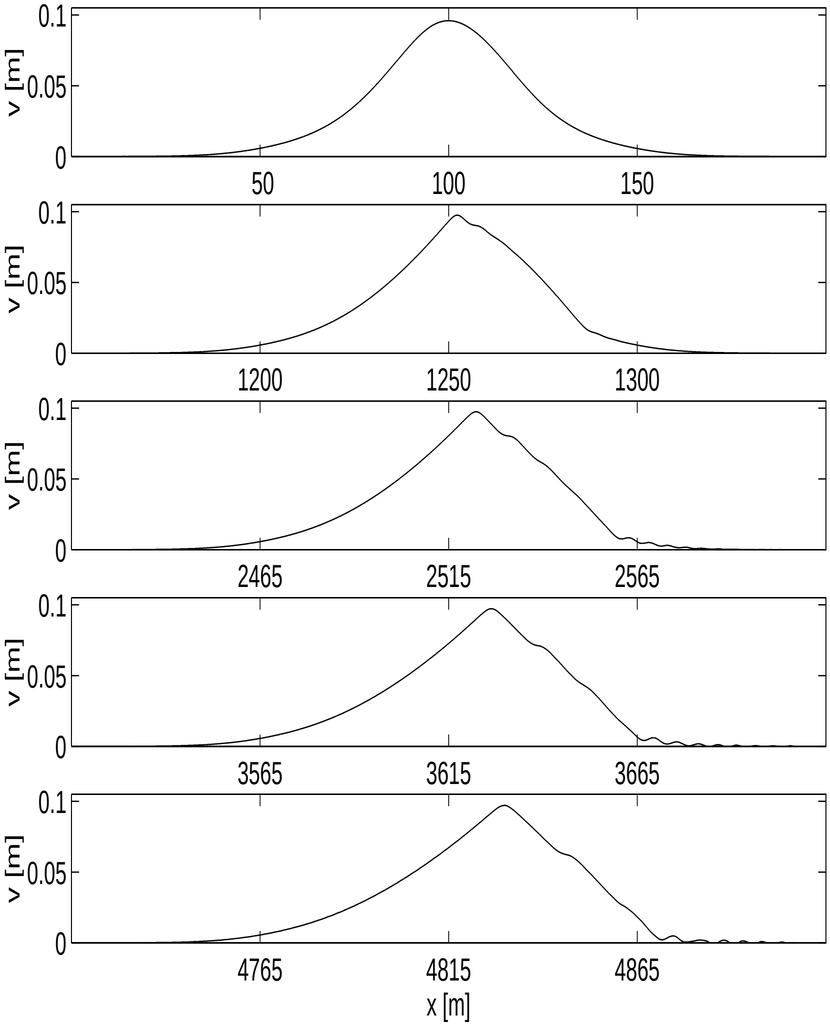

Figure 4.11: Numerical simulation of the propagation of a pulse on cable described by (4.9) with initial condition $u(x, 0) = 0$ and boundary condition given by (4.22), for $t = 3\ s$, $t = 13\ s$, $t = 24\ s$, $t = 34\ s$, and $t = 44\ s$. Compare with figures 4.10 and 4.8 in which the bending stiffness is not included.

In the rest of the section we will deal with the full cable equations, (4.7). Thus now also the longitudinal motion is included in the description.

The characteristic time scale of the longitudinal motion is much smaller than that of the vertical motion. This has two important consequences: The first is that achievement of numerical stability demands much smaller time steps in the time integrations when the longitudinal motion is included in the description. The second is that the effects from the boundary can no longer be ignored. We have modelled the cable in its full length, $L = 1560\ m$, and simply supported at the ends.

These two consequences both put practical limitations on the fineness of the spatial discretisation grid. There is no way we can use as fine discretisations as in the above investigations.

The pulse is initiated with the same boundary condition as above, i.e. (4.22) for $t \leq 300\sqrt{\frac{\mu}{P_0}}$ and $v(0, L) = 0$ otherwise, together with $v(L,t) = v_{xx}(0,t) = v_{xx}(L,t) = u(0,t) = u(L,t) = 0$. Thus the longitudinal motion is excited only by the coupling to the vertical motion as given in (4.7).

In figure 4.12 we have shown snapshots of the propagation of the pulse at $t = 6\ s$, $t = 60\ s$, and $t = 278\ s$. Note that there is practically no deformation of the pulse shape. From the top to the bottom graph, the pulse has travelled a distance of more than 31 *km*. (As a contrary to figures 4.10 and 4.11 we have in figure 4.12 *not* compensated for the finite length of the cable, since the pulse in the simulation actually has travelled back and forward on this finite length cable.) It is barely visible in the bottom graph, that small oscillations of the cable appear *away* from the pulse itself. To search for the origin of these oscillations, we have performed a simulation identical to that of figure 4.12, except for the bending stiffness which was set to zero, $EI = 0$. This simulation is illustrated in figure 4.13. We note that the small oscillations persist for $EI = 0$. Thus the oscillations are not caused by dispersion due to the bending stiffness. (We see

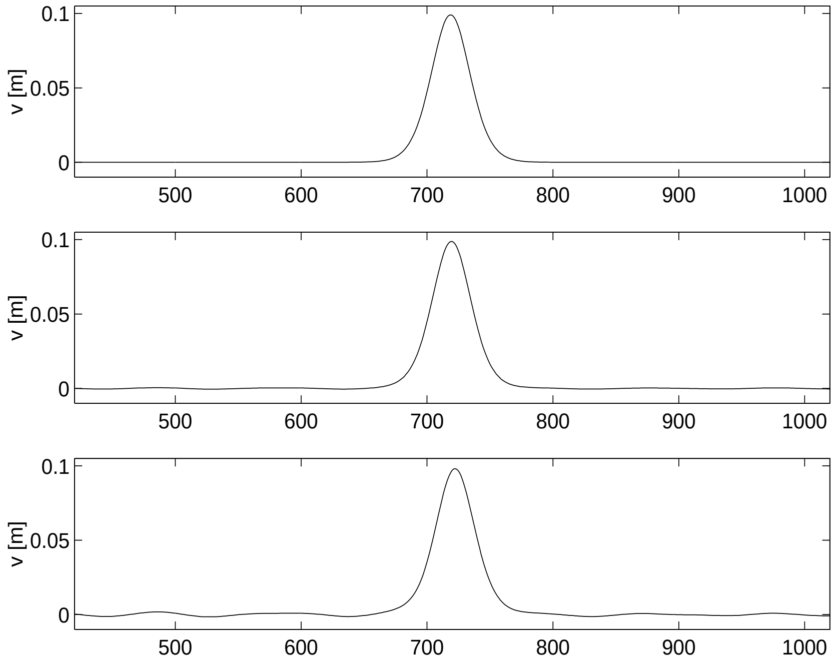

Figure 4.12: Numerical simulation of the propagation of a pulse on cable described by (4.7), for $t = 6\ s$, $t = 60\ s$, and $t = 278\ s$. The pulse travels almost undisturbed. Compare with figures 4.10 and 4.11.

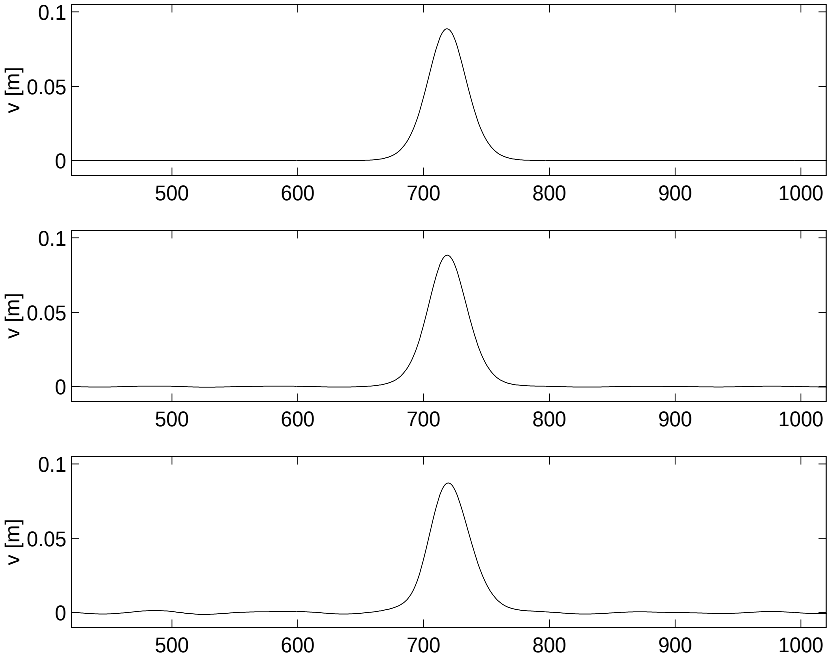

Figure 4.13: Numerical simulation of the propagation of a pulse on cable described by (4.7) with the bending stiffness set to zero, $EI = 0$, for $t = 6$ s, $t = 60$ s, and $t = 278$ s. Compare with figure 4.12.

no effect of the bending stiffness in these simulations, in so far as our discretisation can fully resolve the effect of it.) Unfortunately (but not very important) we can not fully investigate what then causes the small oscillations. They may be caused by *numerical* dispersion (due to the discretisation) or may be an effect of the nonlinearities. But, as mentioned above, due to computer power limitations we can not just refine our discretisation grid to outrule or confirm the numerical dispersion alternative. We can not change the nonlinearities either, without changing the whole system. We are content to realize that propagation of a pulse with the given dimensions on a cable described by (4.7), reveals behaviour very close to the D'Alembert solution of the linearised equation, i.e. a pulse travelling almost without changing shape. (Remark: This conclusion goes for the pulses and cables with the given dimensions and parameters, which are conjectured to be relevant for overhead line systems.)

We have been investigating the importance of the 'small terms' in the equation for the vertical motion in (4.7) by switching on and off the different terms. It seems that none of these terms have significance for the behaviour of the travelling pulse. Lets study the appearance of the different terms in the case of the propagating pulse. We define the 'linear term' lt, the bending term bt, the nonlinear coupling terms $nlt1$ and $nlt2$, and the geometrical nonlinearity term $nlt3$:

$$lt = P_0 v_{xx},$$

$$bt = -EI v_{xxxx},$$

$$nlt1 = EA v_x u_{xx},$$

$$nlt2 = EA v_{xx} u_x,$$

and

$$nlt3 = \frac{3}{2} EA v_x^2 v_{xx}.$$

In figure 4.14 we illustrate the appearance of the different terms at $t = 8.5$ s. We depict the vertical deflection of the cable, v, in the upper graph, the distribution of the linear term, lt, around the pulse in the second graph, the distribution of the bending term, bt, around the pulse in the third graph, and the distribution of the nonlinear terms, $nlt1$ (- -), $nlt2$ (– –) and $nlt3$ (—), around the pulse in the fourth graph. Not surprising it is noted that the linear term is by far the largest term. For the travelling pulse with the given dimensions, the linear term is 2 orders of magnitude larger than the the nonlinear terms, and 4 orders of magnitude larger than the bending term. Thus, apparently the nonlinear terms are much more important than the bending term. Looking closer, however, it

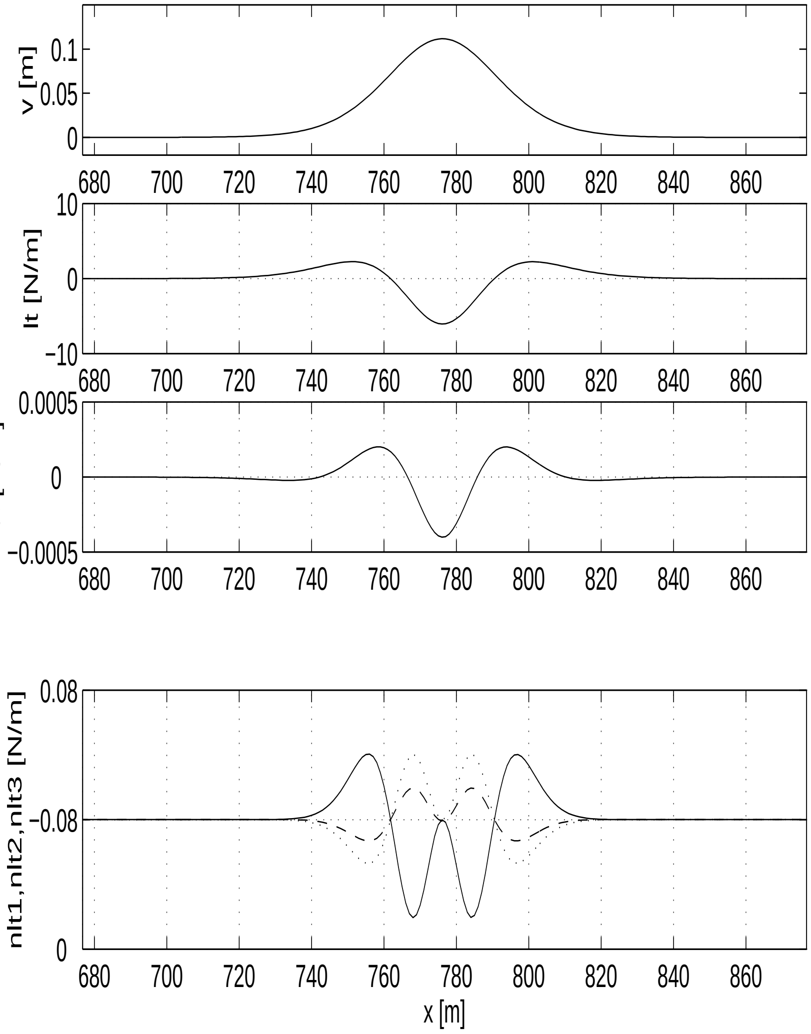

Figure 4.14: Comparison of the appearance of the different terms in the equation for the vertical motion in (4.7) for the travelling pulse at $t = 8.5$ s. First graph: Location of pulse. Second graph: linear stress term, lt. Third graph: bending term, bt. Fourth: Nonlinear terms; $nlt1$ (- -), $nlt2$ (– –), and $nlt3$ (—).

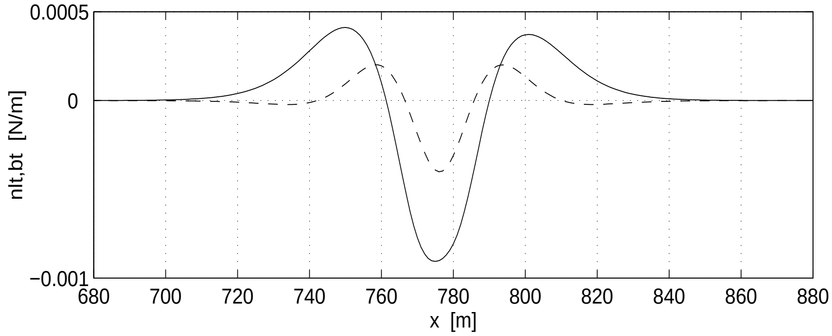

Figure 4.15: Comparison of the sum of the nonlinear terms, $nlt1 + nlt2 + nlt3$ (full line), with the bending term, bt (stabled line). Note that the sum of the nonlinear terms have same order of magnitude as the bending term.

is seen that the two nonlinear coupling terms have sizes and signs so that their sum apparently balances the geometrical nonlinearity term. This is illustrated in figure 4.15 where we have depicted the sum of the nonlinear terms (—) as well as the bending term (- -). It is seen that the sum of the nonlinear terms has same order of magnitude as the bending term for the given pulse.

Let us investigate it further by studying the distribution of the energy on the different contributions. We define the energy per length contributions Ep, Eb, and Enl. Ep describes the potential linear stress energy per length

$$Ep = P_0 \left(u_x + \frac{1}{2} v_x^2 \right) ,$$

Eb describes the bending energy per length

$$Eb = \frac{EI}{2} v_{xx}^2 ,$$

and Enl describes the nonlinear energy per length

$$Enl = \frac{EA}{2}\left(u_x^2 + u_x v_x^2 + \frac{1}{4}v_x^4\right).$$

These are recognized from the derivation of the cable equation in (4.5). In figures 4.16, 4.17, and 4.18 we illustrate the energy distribution for $t = 8.5\ s$, $t = 8.75\ s$, and $t = 9\ s$. The top graphs show the vertical deflection of the cable — the pulse. The second graphs show how the longitudinal motion behaves. It is seen that the longitudinal motion can be thought of as divided into a global oscillating part and a local part centred around the location of the (vertical) pulse. Heuristically it can be seen that the 'local part' of the longitudinal deformation behaves in a way so that it distributes the stress energy to all the cable, instead of having all the stress concentrated around the pulse. The cable is stretched into the pulse. This is supported by the appearance of the linear stress energy and the nonlinear energy in the third and fifth graphs in the figures. Most of the energies in those contributions is global and only small discrepancies are seen around the location of the pulse. Not surprising the bending energy is found to be a local contribution. Note the mutual ratios between the different energy contributions. For the given pulse, the linear stress energy is 3 orders of magnitude larger than the bending energy, and 4 orders of magnitude larger than the nonlinear stress energy.

Referring to our derivation of alternative cable equations in section 4.1, let us study figure 4.14 and figures 4.16-4.18 again. A bit surprising we find $u = \mathcal{O}(v^4) - \mathcal{O}(v^3)$. But $u_x = \mathcal{O}(v_x^3) - \mathcal{O}(v_x^2)$ and $u_{xx} = \mathcal{O}(v_{xx}^2) - \mathcal{O}(v_{xx})$, and studying the nonlinear terms in the equation for the vertical motion *does* yield that the geometrical nonlinearity term, $\frac{3}{2}v_x^2 v_{xx}$, is larger than the other ones, but *also* that the two nonlinear coupling terms are not negligible, especially not since their sum seemingly balances the geometrical nonlinearity term.

Lets develop the idea of the longitudinal motion consisting of a global

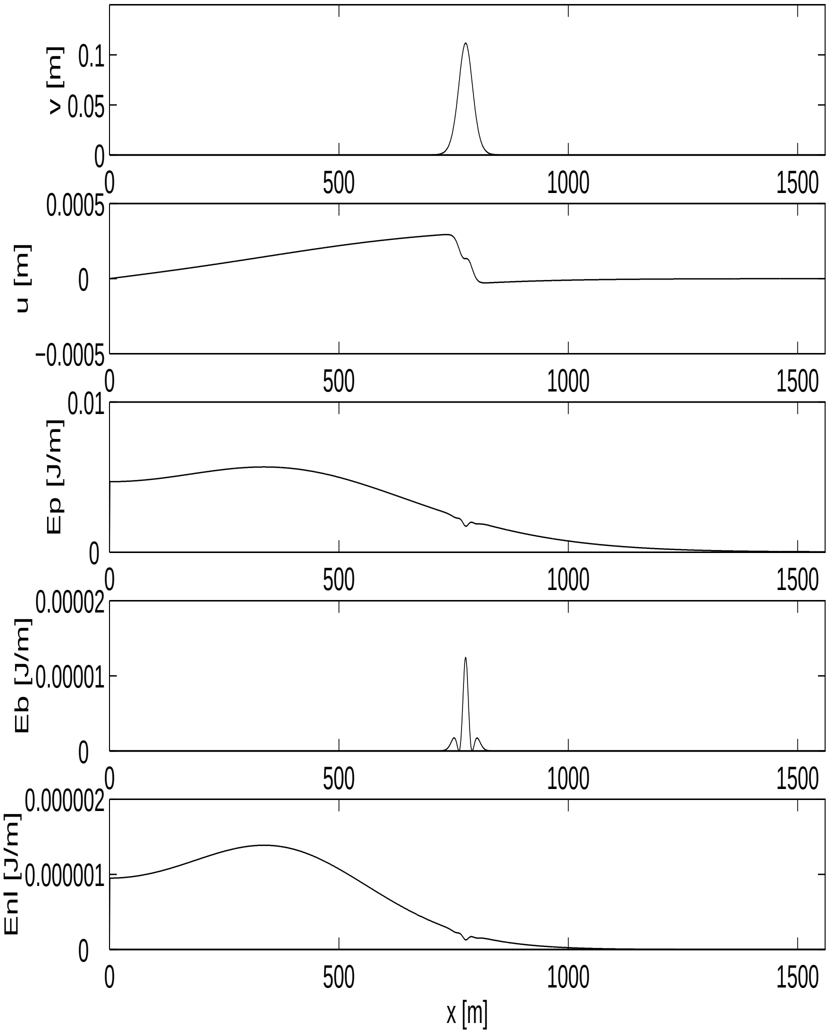

Figure 4.16: Vertical and longitudinal deflection of propagating pulse at $t = 8.5\ s$. Distribution of energy on the contributions: linear stress energy per length Ep, bending energy per length Eb, and nonlinear stress energy per length Enl.

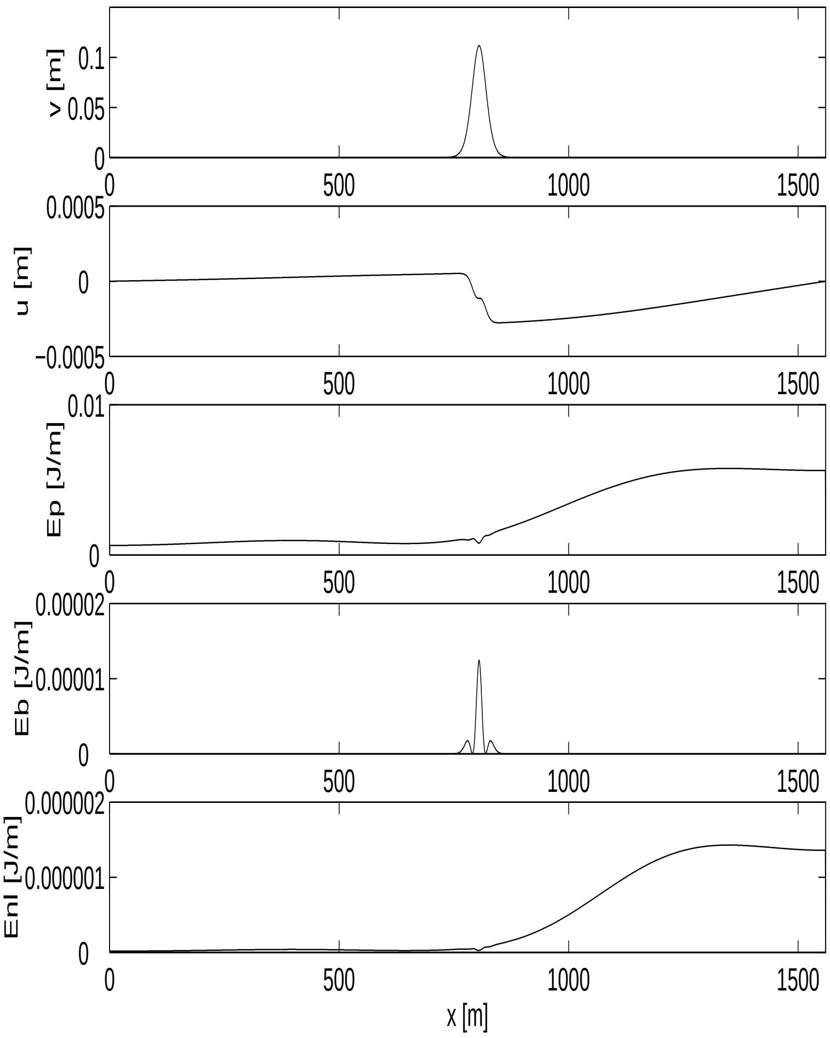

Figure 4.17: Vertical and longitudinal deflection of propagating pulse at $t = 8.75$ s. Distribution of energy on the contributions: linear stress energy per length *Ep*, bending energy per length *Eb*, and nonlinear stress energy per length *Enl*.

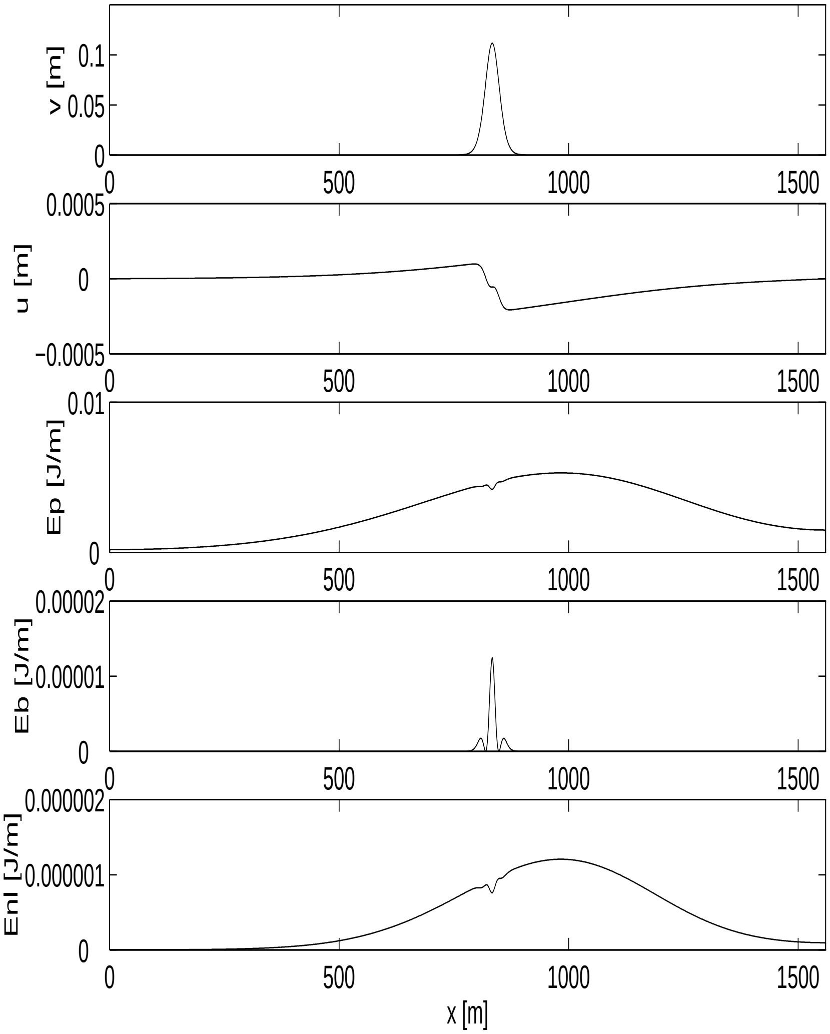

Figure 4.18: Vertical and longitudinal deflection of propagating pulse at $t = 9$ s. Distribution of energy on the contributions: linear stress energy per length Ep, bending energy per length Eb, and nonlinear stress energy per length Enl.

and a local part. We exploit that the local part has a much larger characteristic time scale than the global part. Thus we write

$$u(x,t) = u^{(0)}(x,\epsilon t) + \epsilon^2 u^{(2)}(x,T_0) = u^{(0)}(x,T_1) + \epsilon^2 u^{(2)}(x,t) \quad (4.24)$$

with $|\epsilon| << 1$. Thus, $u^{(0)}$ describes the slow part and $u^{(2)}$ describes the fast part. The equation for the longitudinal motion becomes

$$\begin{gathered} \mu u_{tt} = EAu_{xx} + EAv_x v_{xx} \\ \Longleftrightarrow \\ \mu\epsilon^2 u^{(0)}_{T_1T_1} + \mu\epsilon^2 u^{(2)}_{T_0T_0} = EAu^{(0)}_{xx} + \epsilon^2 EAu^{(2)}_{xx} + EAv_x v_{xx}. \end{gathered} \quad (4.25)$$

We then find the equations

$$0^\circ \qquad 0 = EAu^{(0)}_{xx} + EAv_x v_{xx} \quad (4.26)$$

and

$$2^\circ \qquad \mu u^{(2)}_{T_0T_0} = EAu^{(2)}_{xx} - \mu u^{(0)}_{T_1T_1}. \quad (4.27)$$

Integration of (4.26) with respect to x yields

$$\int \left(u^{(0)}_{xx} + v_x v_{xx}\right) dx = u^{(0)}_x + \frac{1}{2}v_x^2 = C(T_1) \quad (4.28)$$

and

$$\begin{gathered} \textstyle\int_0^x \left(u^{(0)}_{x'} + \frac{1}{2}v^2_{x'}\right) dx' = u^{(0)}(x) - u^{(0)}(0) + \frac{1}{2}\int_0^x v^2_{x'}\, dx' = \\ u^{(0)}(x) + \textstyle\frac{1}{2}\int_0^x v^2_{x'}\, dx' = \int_0^x C(T_1) dx' = C(T_1)x. \end{gathered} \quad (4.29)$$

By inserting $x = L$ in (4.29) and exploiting $u^{(0)}(L) = 0$ we have

$$\begin{gathered} u^{(0)}(L) + \frac{1}{2}\int_0^L v^2_{x'}\, dx' = C(T_1)\cdot L \qquad \Longleftrightarrow \\ C(T_1) = \frac{1}{2L}\int_0^L v^2_{x'}\, dx', \end{gathered} \quad (4.30)$$

and $u^{(0)}$ is found by inserting (4.30) in (4.29):

$$u^{(0)}(x) = \frac{x}{2L}\int_0^L v^2_{x'}\, dx' - \frac{1}{2}\int_0^x v^2_{x'}\, dx'. \quad (4.31)$$

Lets illustrate that $\frac{\partial^2}{\partial T_1^2}u^{(0)}$ can be seen as an excitation of $u^{(2)}$. In the case of the travelling pulse, we have seen that there is only very little deformation of the pulse shape. This means that we can approximate

$$\frac{\partial^2}{\partial T_1^2}u^{(0)} \approx -\frac{1}{2}\frac{\partial^2}{\partial T_1^2}\int_0^x v_{x'}^2\,dx'$$

and (4.27) becomes

$$\mu u_{T_0T_0}^{(2)} = EAu_{xx}^{(2)} + \frac{\mu}{2}\frac{\partial^2}{\partial T_1^2}\int_0^x v_{x'}^2\,dx'. \tag{4.32}$$

In figure 4.19 we have illustrated $\frac{\partial^2}{\partial t^2}\int_0^x v_{x'}^2\,dx'$ in the case of the travelling pulse. The pulse is travelling towards right. From top to bottom the figure illustrates v, v_x, v_x^2, $\int_0^x v_{x'}^2\,dx'$, $\frac{\partial}{\partial t}\int_0^x v_{x'}^2\,dx'$, and $\frac{\partial^2}{\partial t^2}\int_0^x v_{x'}^2\,dx'$. The figure shows that $\frac{\mu}{2}\frac{\partial^2}{\partial t^2}\int_0^x v_{x'}^2\,dx'$ is located around the centre of the travelling pulse. Thus, equation (4.32) will experience the term as a local excitation.

Since the pulse travels very slowly compared to the propagation velocity for $u^{(2)}$, lets assume that only the first (linear) mode of $u^{(2)}$ is excited. We then have

$$\begin{aligned} u^{(2)} &= f_1(t)\cdot\sin\left(\tfrac{\pi x}{L}\right)\\ u_x^{(2)} &= \tfrac{\pi}{L}f_1(t)\cdot\cos\left(\tfrac{\pi x}{L}\right)\\ u_{xx}^{(2)} &= -\tfrac{\pi^2}{L^2}f_1(t)\cdot\sin\left(\tfrac{\pi x}{L}\right). \end{aligned}$$

For $u = u^{(0)} + \epsilon^2 u^{(2)}$ we have

$$\begin{aligned} u &= \tfrac{x}{2L}\textstyle\int_0^L v_{x'}^2\,dx' - \tfrac{1}{2}\int_0^x v_{x'}^2\,dx' + f_1(t)\cdot\sin\left(\tfrac{\pi x}{L}\right)\\ u_x &= \tfrac{1}{2L}\textstyle\int_0^L v_{x'}^2\,dx' - \tfrac{1}{2}v_x^2 + \tfrac{\pi}{L}f_1(t)\cdot\cos\left(\tfrac{\pi x}{L}\right)\\ u_{xx} &= -v_x v_{xx} - \tfrac{\pi^2}{L^2}f_1(t)\cdot\sin\left(\tfrac{\pi x}{L}\right). \end{aligned} \tag{4.33}$$

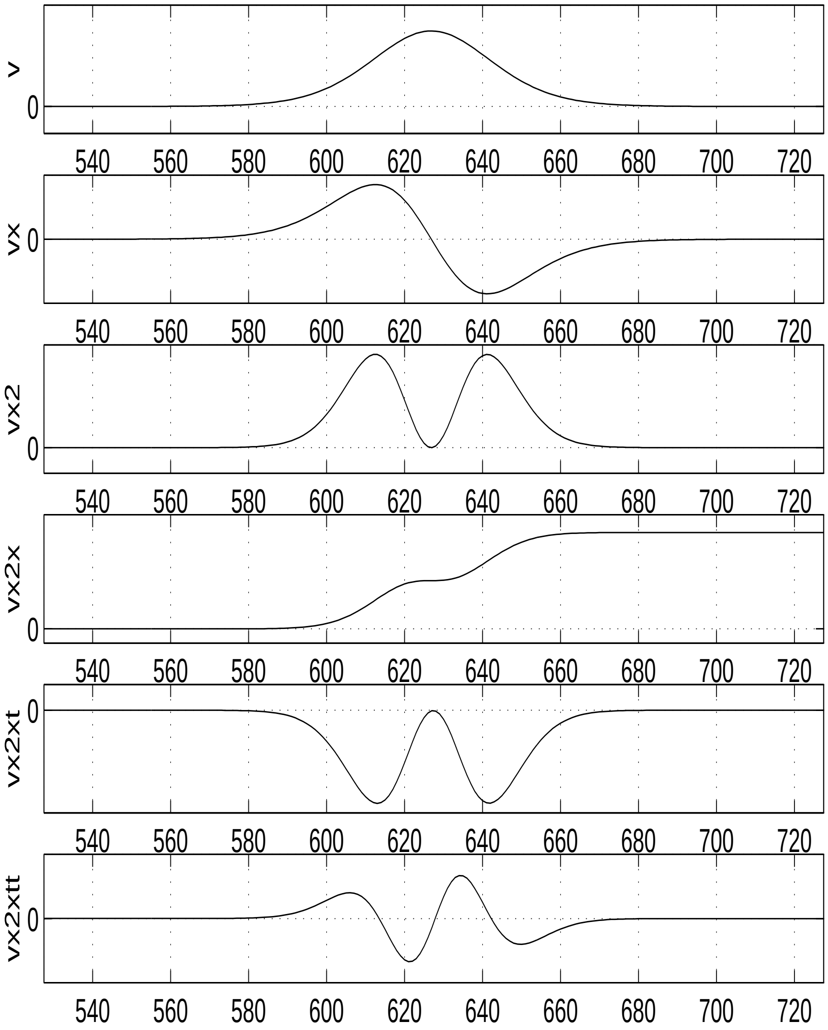

Figure 4.19: Illustration of the excitation in the $u^{(2)}$-equation, (4.32). From top to bottom: v, v_x, v_x^2, $\int_0^x v_{x'}^2\,dx'$, $\frac{\partial}{\partial t}\int_0^x v_{x'}^2\,dx'$, and $\frac{\partial^2}{\partial t^2}\int_0^x v_{x'}^2\,dx'$. Note that $\frac{\partial^2}{\partial t^2}\int_0^x v_{x'}^2\,dx'$, which goes into (4.32), behaves like a localised excitation.

We insert (4.33) in the equation for the vertical motion. The nonlinear terms then become

$$\begin{aligned}
&EA\left(v_{xx}u_x + v_x u_{xx} + \tfrac{3}{2}v_x v_{xx}\right) = \\
&EA\left(v_{xx}\left(\tfrac{1}{2L}\int_0^L v_{x'}^2\,dx' - \tfrac{1}{2}v_x^2 + \tfrac{\pi}{L}f_1(t)\cdot\cos\left(\tfrac{\pi x}{L}\right)\right) + \right.\\
&\left. v_x\left(-v_x v_{xx} - \tfrac{\pi^2}{L^2}f_1(t)\cdot\sin\left(\tfrac{\pi x}{L}\right)\right) + \tfrac{3}{2}v_x v_{xx}\right) = \\
&EA\left(\left(\tfrac{1}{2L}\int_0^L v_{x'}^2\,dx' + \tfrac{\pi}{L}f_1(t)\cdot\cos\left(\tfrac{\pi x}{L}\right)\right)v_{xx} - \right.\\
&\qquad\qquad \left.\left(\tfrac{\pi^2}{L^2}f_1(t)\cdot\sin\left(\tfrac{\pi x}{L}\right)\right)v_x\right) = \\
&\qquad\qquad (K + K_1(t))\,v_{xx} + K_2(t)v_x.
\end{aligned} \tag{4.34}$$

We remark that

- $\frac{1}{2L}\int_0^L v_{x'}^2\,dx'$ is close to being a constant in the case of the travelling pulse, since, as we have discussed above, the shape of the pulse is almost unchanged under the propagation. If the assumption $u_{tt} = 0$ is made (no axial inertia forces), the sum of the nonlinear terms in the equation for the vertical motion would yield $\frac{1}{2L}\int_0^L v_{x'}^2\,dx'$. We will refer to this term as the *bias-*v_{xx} term in the following.
- we expect the time modulation of the v_{xx}-term in the sum, $K_1(t)$, to be oscillatory with a period equal to that of the lowest (linear) mode of the longitudinal motion. This can be found as $T_0 = 2L\sqrt{\frac{\mu}{EA}}$. With the given cable data we get $T_0 \approx 0.85\ s$.
- the time modulation of the v_x-term in the sum, $K_2(t)$, looks like that of the v_{xx}-term except for the factor $-\frac{\pi}{L}$, which for the given cable data yields $\frac{\pi}{L} \approx 0.002$.

Thus from these considerations we expect to find that the sum of the nonlinear terms consists of a bias v_{xx}-term, an oscillating v_{xx}-term, and a small oscillating v_x-term.

Let us depict how it *does* look in the simulation (which of course is performed with the full equations, (4.7)). In figure 4.20 we have made a small cartoon depicting the sum of the nonlinear terms $nlt1+nlt2+nlt3$ (full line) around the pulse, and the bias-v_{xx} term from the above analysis, $\frac{1}{2L}\int_0^L v_{x'}^2\,dx'\;v_{xx}$ (stabled line). In figure 4.21 there is a similar cartoon, depicting the sum of the nonlinear terms minus the bias-v_{xx} term, $nlt1+nlt2+nlt3-\frac{1}{2L}\int_0^L v_{x'}^2\,dx'\;v_{xx}$ (full line), and the bias-v_{xx} term (stabled line). Two things are noted from the figures: The first thing is that the sum of the nonlinear terms actually does look like what we expected from the above analysis. The sum of the nonlinear terms is basically an oscillating v_{xx} signal superponed with the bias-v_{xx} signal. The second thing to notice is, as is seen from the cartoons, that the period of the oscillation is in the interval $0.8\ s \leq T_{per} \leq 0.9\ s$ corresponding to the period of the first longitudinal mode, $T_0 \approx 0.85\ s$ — as expected from the above analysis.

4.2.3 Conclusions on pulse propagation

We derived the equations of motion of a near horizontal cable, (4.7). These equations contain a term for the bending stiffness of the cable, as well as nonlinear coupling terms of the longitudinal and the vertical motions, and a geometrical nonlinearity term.

Neglecting the bending stiffness and assuming $u = \mathcal{O}(v^3)$, the equation for the vertical and the longitudinal motion in (4.7) decoupled, and (4.8) became the equation for the vertical motion. This equation we were able to solve analytically. We found that a smooth pulse travelling on a cable described by (4.8) underwent deformations and developed shocks, appearing as discontinuities in the slope. However, with the discontinuities in the slope of the cable, the assumption of negligible bending stiffness (neglected by putting it to zero) certainly was not valid any longer.

Including a term for the bending stiffness, (4.9) became the equation for the vertical motion of the cable. The propagation of the same smooth pulse as before, but with (4.9) as the cable equation, was

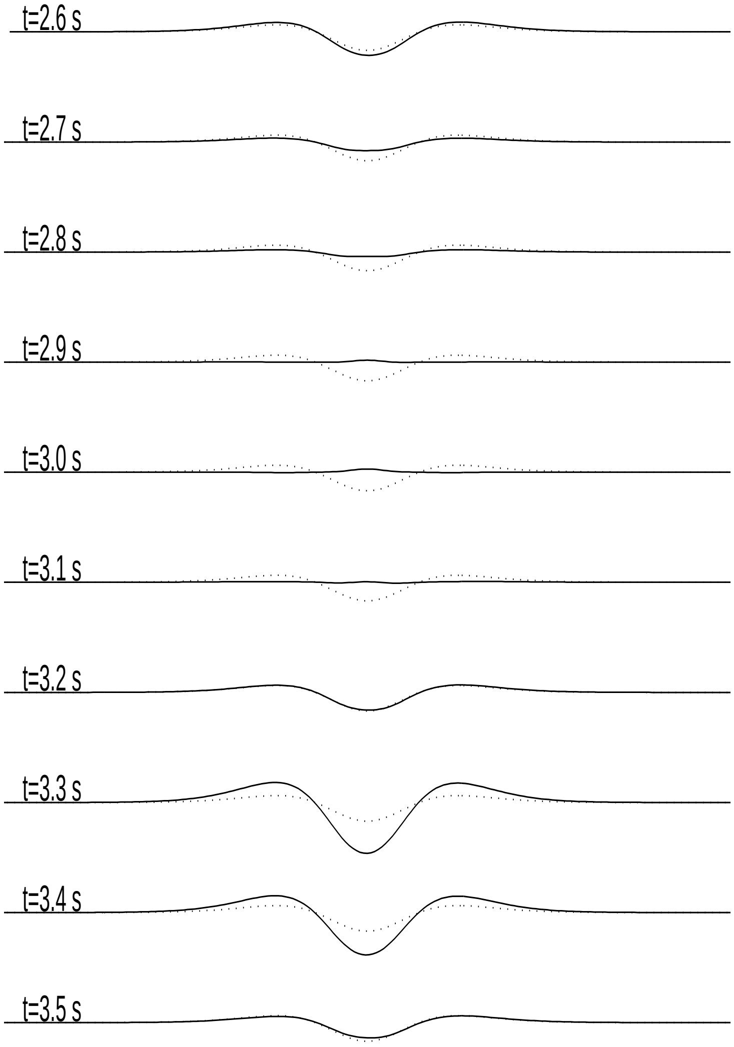

Figure 4.20: Cartoon with comparison of the sum of the nonlinear terms $nlt1 + nlt2 + nlt3$ (—) with $\frac{1}{2L}\int_0^L v_{x'}^2\, dx'\; v_{xx}$ (- -). It is seen that the sum of the nonlinear terms basically consists of an oscillating v_{xx} signal superponed with the bias-v_{xx} signal. Compare with figure 4.21.

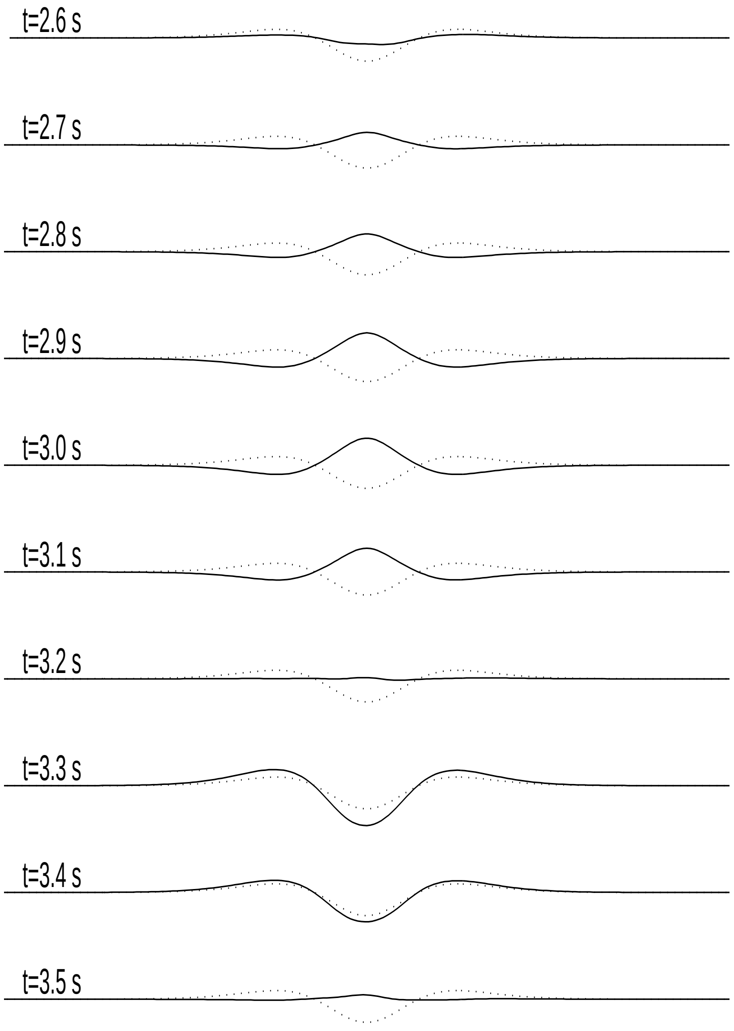

Figure 4.21: Cartoon with comparison of $nlt1 + nlt2 + nlt3 - \frac{1}{2L}\int_0^L v_{x'}^2\, dx'\ v_{xx}$ (—) with $\frac{1}{2L}\int_0^L v_{x'}^2\, dx'\ v_{xx}$ (- -). It is seen that $nlt1 + nlt2 + nlt3 - \frac{1}{2L}\int_0^L v_{x'}^2\, dx'\ v_{xx} \sim K_1(t) v_{xx}$. The period of the recurrence is in the interval $0.8\ s \leq T_{per} \leq 0.9\ s$ corresponding to the period of the first longitudinal mode, $T_0 \approx 0.85\ s$.

solved numerically. The discontinuities were smoothed out but the *overall* deformation of the pulse shape was the same. Thus, for the given investigations, the bending stiffness was found to have very little influence on the pulse propagation.

The propagation of the same pulse again but with the full cable equations, (4.7), was solved numerically. We found that the propagation of the pulse on a cable described by these equations were very close to the propagation of the pulse on a cable described by the linear string equation, (4.1), which is just propagation of the pulse without deforming. Comparisons of the different terms in the equations and investigating the energy distribution suggested that the longitudinal motion of the cable could be described by a relatively slow, local part, and a relatively fast, global part. Going through these considerations we found expressions for the slow and the fast parts, in the case of the travelling pulse. The expressions yielded the longitudinal motion, u as the sum of the solution for u under the assumption of no axial inertia forces, and the excited first linear mode of u. When this was plugged into the equation for the vertical motion, the sum of the nonlinear terms was found to basically consist of a term on the form $(K + K_1(t))v_{xx}$. See (4.34). The correspondence between these expressions and the results from the the numerical simulations with the full equations was remarkably good.

4.3 Overhead line systems

In this section we shall consider the designs of overhead line systems. We discuss the simple, sagged configuration, the stitched configuration (or Y-configuration), and the compound configuration. These are illustrated in figure 4.22.

An overhead line system is a compromise between quality and economy. The larger train speeds an overhead line system has to serve, the better quality the configuration must have — and the more expensive it is. The question now is, for some given wanted quality,

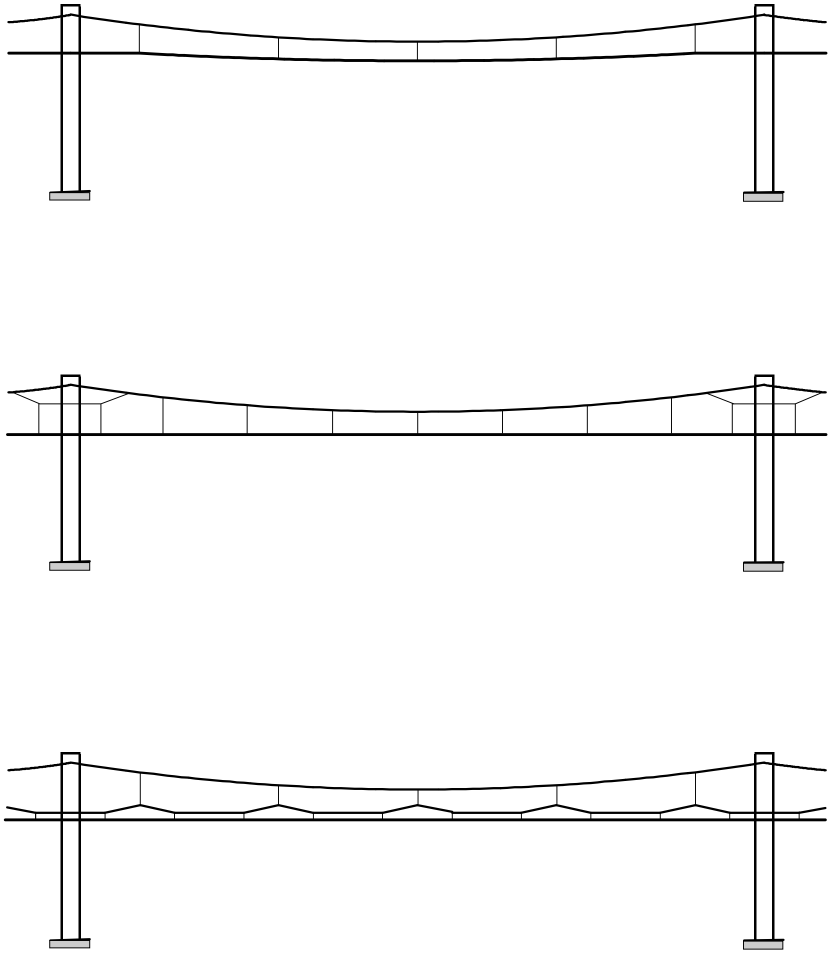

Figure 4.22: Overhead line system configurations: The simple, sagged configuration, the stitched configuration, and the compound configuration.

what is the cheapest configuration this quality can be obtained with. Such questions form the background of this part of the ph.d. project.

The cheapest possible overhead line configuration is the so called trolley configuration, which is just the supported contact cable. This configuration is used as overhead equipment for tramways and other types of vehicles with relatively low travel speeds, or in railway areas with only low speed traffic.

In the *simple* configuration, the contact cable is carried by a catenary cable via the hangers, which typically are cables. By purely statical considerations it is realized that the configuration is softer in the middle of a span than at the position of the masts. Thus, a pantograph travelling under the overhead line system will have a larger uplift at midspan than at support. This is compensated for by giving the contact cable a *presag* corresponding to the expected extra uplift. This is supposed to make the pantograph travel more smoothly and is a very widely used technique. In our section with results and investigations we shall discuss this presag.

Another way to compensate for the varying stiffness is by adopting the *stitched* configuration, see figure 4.22. Compared to the simple configuration, the stitched configuration has extra stitch wires, and around the masts, the contact cable is carried by the catenary cable via the stitch wires. This reduces the stiffness of the configuration around the masts and a more homogene elasticity experienced by the pantograph is obtained. The drawback is of course that the configuration is more expensive. The system height is increased, more materials go into the installation, it takes longer time to install — and not to forget, the maintenance costs are higher.

The *compound* configuration (see figure 4.22) has an even more homogene elasticity, seen from the pantograph, but is even more expensive. The contact cable is carried by an auxiliary cable, which is carried by the catenary cable.

Considering a specific type of configuration, there are still a number of parameters to vary: the system height, the number of droppers per span, the span length, the type of dropper, the type of support, the material of the cables, the mass per length of the cables, the prestress of the cables, etc. It would be beyond the scope of this thesis to discuss all these parameters. We will only consider a few of them and refer to what is being used.

Together with the choice of overhead line system configuration, the *prestress* of the contact cables, and to less degree of the catenary cables, are some of the most important design parameters. The larger the prestress is, the less flexible the overhead line system is, and the better properties it has for dynamic interactions with pantographs. Especially as the train speeds approach the propagation velocity of transversal waves — the so called critical speed — the problems worsen. The critical speed is given as $v_c = \sqrt{\frac{P_0}{\mu}}$. But the prestress is closely connected to the mass per length of the cables. The prestress is chosen as high as possible and the cables can not be prestressed stronger without compromising safety. Hence an increase of the prestress can only be obtained by increasing the cable diameters. I.e. the critical speed is independent of this manoeuvre. Unless new materials are used which allow higher prestress. The usual material for contact cables is a copper silver alloy. The silver is added to avoid long time creep of the cables; typically the silver content is 0.1 %. (Which doubles the price compared to pure copper cables. Earlier a copper cadmium alloy was used. For obvious reasons it isn't anymore!) In the newest German overhead line system, the Re330, a copper magnesium alloy is used for the contact cables. This material enables a lager prestress, such that the critical speed for this system is 565 km/h against the typical 410-440 km/h, [30].

According to our informations, the compound configuration is only still being used widely in Japan (for which informations are very hard to obtain). It was earlier used in France and lines with compound configuration of course still exist there. However, the french switched to the stitched configuration — and to our knowledge they have now skipped this one too, in favour of the simple, sagged configuration with rather strong prestress and corresponding large cable diameters.

In Germany, overhead line systems with a stitched configuration are the most common ones. Their standard configuration (at least until recently), the Re250, has 'medium' prestress and cable diameters.

Italy, which traditionally is among the leading countries when it comes to railway technology, is hard to compare with, since they only have DC overhead line systems. (France has some early DC systems, but switched a long time ago.) DC current systems have lower voltages and thus higher current intensities than AC current systems. In order to carry this current, rather heavy cables and pantographs are necessary. (The dynamics of DC overhead equipment/DC pantographs is inferior to the dynamics of AC overhead equipment/AC pantographs.) However, our informations are that the future high speed line between Rome and Neaples will have an AC overhead line system with simple configuration.

Thus, the 'battle' now apparently is between the stitched and the simple configuration. Measured in man-power, the stitched configuration is more expensive to install and maintain than the simple configuration. On the other hand, the simple configuration must have larger prestress to achieve the same performance, which makes the material cost larger. It shall be interesting to see which approach will be the cheaper over a 20 year period.

4.4 Catenary system model

All our numerical investigations in this project are based on the overhead line system in use in Denmark, which is a 25 kV AC current system, with a light weight, low tensioned simple, sagged configuration. The contact cable is made of a copper silver alloy, has a cross section of 100 mm^2, and is prestressed with $P_0 = 12000\ N$. The mass per length, the bending stiffness and the axial stiffness are $\mu = 0.91\ kg/m$, $EI = 98.6\ Nm^2$, and $EA = 1.24 \cdot 10^7\ N$. The catenary cable is made of bronze, has a cross section of 50 mm^2 and with the same prestress as the contact cable, $P_{02} = 12000\ N$.

The mass per length, the bending stiffness and the axial stiffness are $\mu_2 = 0.50\ kg/m$, $EI_2 = 50\ Nm^2$, and $EA_2 = 0.5 \cdot 10^7\ N$. Each span is 60 m and there are 5 droppers per span equally distanced, which leaves 12 m between the droppers. The presag is $\frac{1}{1000}$ of the span length, i.e. 0.06 m. We model a section of 20 spans, $L = 1200\ m$.

The equations of motion of the cables are based on the full nonlinear equations from section 4.1. There is a set of partial differential equations corresponding to (4.7) for each cable. Terms for dropper forces, influence of the registration arms, support forces, gravity and pantograph impact are added.

4.4.1 Droppers

The design of droppers varies. In the danish overhead line systems, they typically consist of a piece of bronze cable with suitable length, clamped to the catenary cable and the recess of the contact cable. In other designs the droppers are not clamped to the catenary cable but lying across it. See figure 4.23. We believe the actual design of the droppers is not very important. We model the droppers as bilinear springs with a very stiff spring coefficient given by the axial stiffness divided by the length of the dropper when loaded, $k_{drop} = \frac{EA_{drop}}{DL_0}$, and zero stiffness when slacking:

$$Fdrop_m = \begin{cases} \frac{EA_{drop}}{DL_{0,m}} (dist_m - DL_{0,m}) & , (dist_m - DL_{0,m}) \geq 0 \\ 0 & , (dist_m - DL_{0,m}) < 0 \end{cases} ,$$

see figure 4.24. In the figure we have indicated both the bilinear spring model and a more realistic dropper force relation.

4.4.2 Registation arms

To distribute the wear on the contact strips of the pantographs, due the friction between the contact cable and the contact strips, a stag-

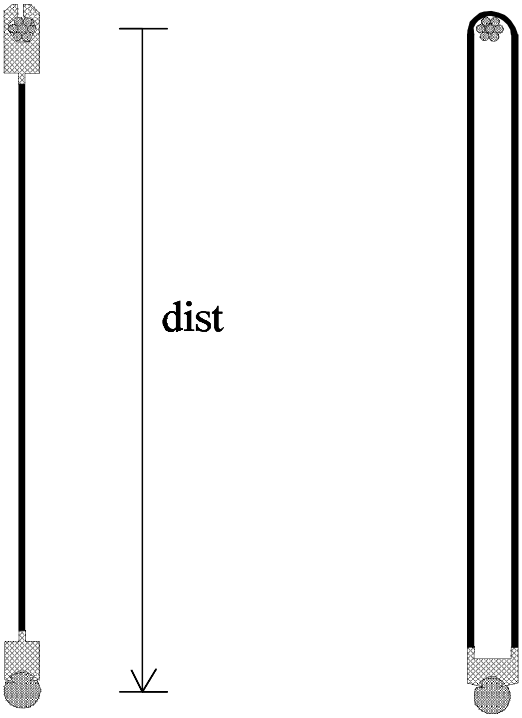

Figure 4.23: Two different dropper design. In Denmark the one on the left is most usual.

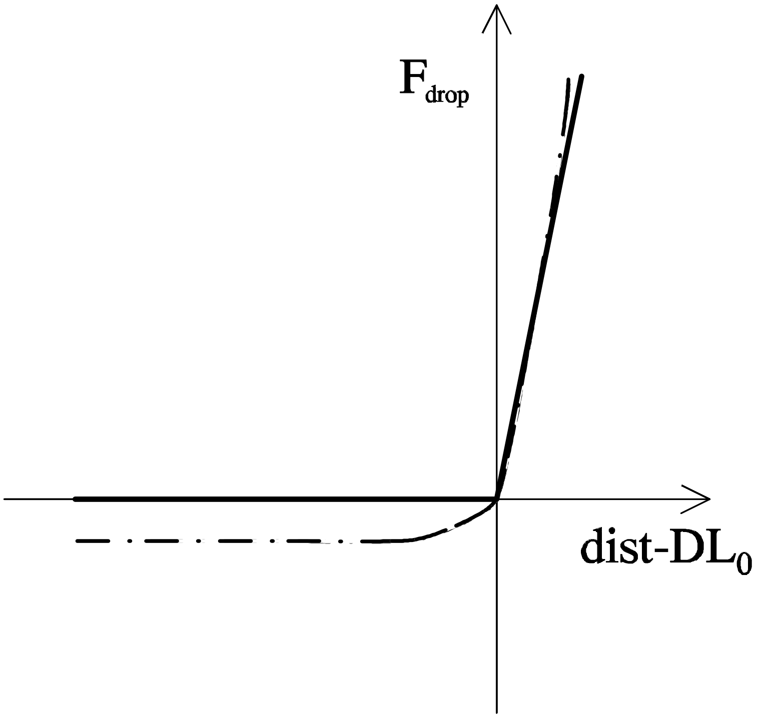

Figure 4.24: The nonlinear dropper force relation. The dropper force is modelled as a bilinear spring. *dist* is the actual distance between the catenary and the contact cable; DL_0 is the lenght of the unloaded dropper.

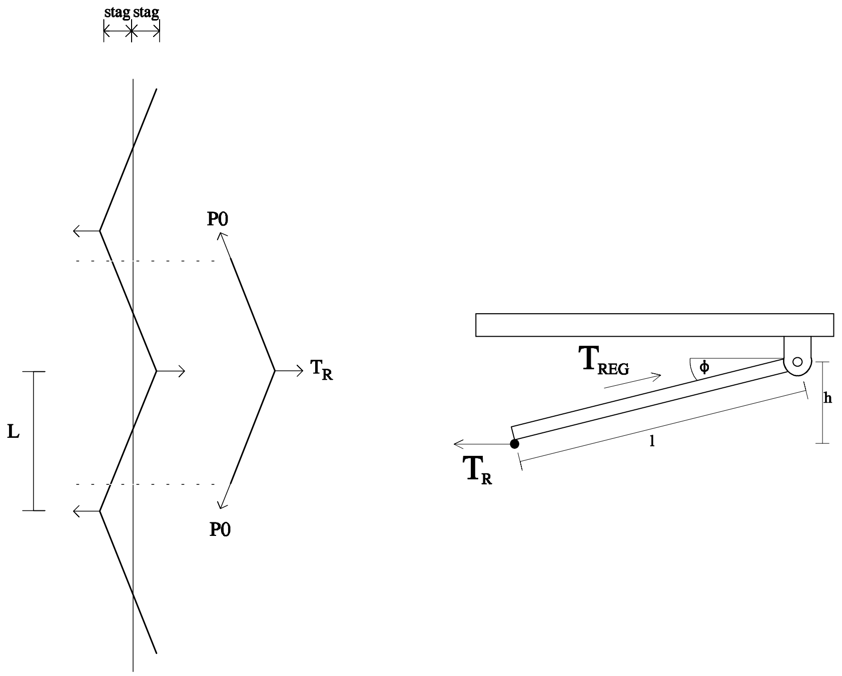

Figure 4.25: Stagger configuration; registration arm equipment.

ger of the overhead line systems is implemented. As mentioned earlier, a simple, sagged overhead line system has larger stiffness at the supports than at midspan. The *stagger* increases this phenomenon in that the presence of a registration arm gives rise to an extra localised stiffness and an extra point mass fixed on the contact cable at the position of the registration arm.

Apparent stiffness

Let us derive an expression for the extra apparent stiffness of the contact cable at the position of a registration arm. In figure 4.25 the stagger and the registration arm equipment is illustrated. T_R

is the horizontal reaction force between the contact cable and the registration arm, which implements the stagger. T_{REG} is then the axial force in the registration arm. l is the length of the registration arm and h is the heel setting. ϕ is the angle between the registration arm and horizontal. The prestress force in the contact cable is P_0. The length of each span is L and the size of the stagger is $\pm stag$.

For equilibrium of the registration arm, T_R must be balanced by $T_{REG}\cos\phi$. The vertical component of the force in the registration arm is then given as $T_{REG}\sin\phi$. In equilibrium this vertical force is balanced by a local deflection of the contact cable. Any displacement of the registration arm will result in unbalanced loading of the arm resulting in a restoring force on the contact wire. We neglect the lateral motion of the contact cable and derive T_R

$$T_R = 2\frac{2\cdot stag}{\sqrt{stag^2+L^2}}P_0 \approx \frac{4\cdot stag\cdot P_0}{L}. \tag{4.35}$$

With

$$\sin\phi = \frac{h}{l} \quad \text{and} \quad \cos\phi = \sqrt{1-\sin^2\phi} = \sqrt{1-\left(\frac{h}{l}\right)^2}$$

we find the axial force in the registration arm

$$T_{REG} = \frac{T_R}{\cos\phi} = \frac{4\cdot stag\cdot P_0}{L\sqrt{1-\left(\frac{h}{l}\right)^2}}, \tag{4.36}$$

and the vertical composant becomes

$$T_{REG}\sin\phi = \frac{4\cdot stag\cdot P_0\cdot h}{l\cdot L\sqrt{1-\left(\frac{h}{l}\right)^2}}. \tag{4.37}$$

The stiffness coefficient k_a of the apparent stiffness is then calculated

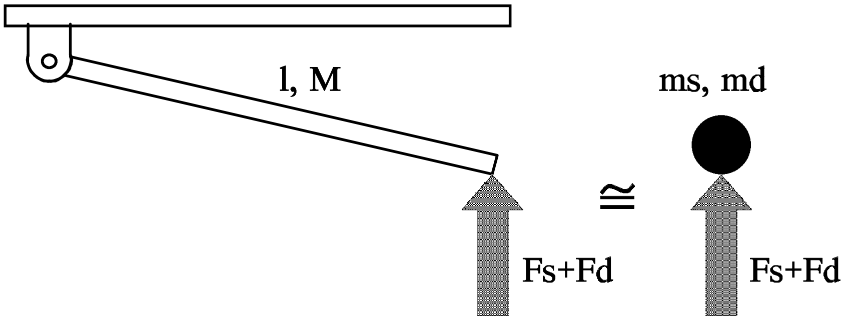

Figure 4.26: Registration arm and equivalent point mass system.

as

$$k_a = \frac{d(T_{REG}\sin\phi)}{dh} = \frac{4\cdot stag\cdot P_0}{l\cdot L\sqrt{1-\left(\frac{h}{l}\right)^2}} - \frac{4\cdot stag\cdot P_0\cdot h}{2\cdot l\cdot L\left(1-\left(\frac{h}{l}\right)^2\right)^{\frac{3}{2}}}\left(-\frac{2\cdot h}{l^2}\right) = \frac{4\cdot stag\cdot P_0}{l\cdot L\left(1-\left(\frac{h}{l}\right)^2\right)^{\frac{3}{2}}}. \tag{4.38}$$

With parameter values for the danish overhead line equipment: stagger $stag = \pm\ 0.2\ m$, pretension force $P_0 = 12\ kN$, (typical) length of registration arm $l = 1.1\ m$, heel setting $h = 0.15\ m$, and span length $L = 60\ m$, we find that the upwards pointing force on the contact cable $T_{REG}\sin\phi \approx 14.6\ N$, and the stiffness coefficient of the extra apparent stiffness as $k_a = 147\ N/m$.

Registration arm equivalent dynamic mass

The registration arm also gives rise to extra localised inertia and static load. Considering figure 4.26, with $F_d = 0$, we easily derive the static load of the registration arm

$$-Mg\frac{l}{2} + F_s l = 0 \ \Leftrightarrow\ F_s = \frac{Mg}{2},$$

which leaves the equivalent static point mass $m_s = \frac{M}{2}$. We then set $g = 0$ and write the equation of motion of the registration arm as:

$$\frac{1}{3}Ml^2\ddot{\phi} = F_d l.$$

$\frac{1}{3}M\,l^2$ is the inertial moment of the registration arm through the fixed endpoint. We call the vertical deflection of the non-fixed endpoint of the registration arm x and approximate this as $x = l\sin(\phi) \approx l\phi$ leaving the equation of motion of the registration arm as

$$\frac{1}{3}M\ddot{x} = F_d.$$

For the equivalent system the equation of motion is

$$m_d\ddot{x} = F_d,$$

and the equivalent dynamical point mass thus is

$$m_d = \frac{M}{3}. \tag{4.39}$$

A registration arm in Denmark typically has the physical weight $M = 1.54\ kg$. With these data the static load is $F_s \approx 7.6\ N$ and the dynamical point mass is $m_d \approx 0.51\ kg$.

4.4.3 Support

We are convinced that the error made by assuming infinitely rigid supports is of minor importance. Some authors have performed dynamic tests with the cantilever structure supporting the catenary cable at each mast, [7], and found that the support should be equivaleted with a sprung mass, mass and stiffness coefficient given by $M_{support} = 438\ kg$ and $k_{support} = 280000\ N/m$.

More for the sake of convenience than for the sake of accurate modelling, we model all the intermediate supports as preforced springs with the spring coefficients given as in [7]:

$$Fsup_m(t) = -280000 \cdot (v2(xsup_m, t) - v2(xsup_m, 0)) + Fsup_{0,m}, \tag{4.40}$$

where $Fsup_m$ is the m'th support force, $v2(x,t)$ is the vertical deflection of the catenary cable, $xsup_m$ is the position of the m'th support, and $Fsup_{0,m}$ is the preforce of the spring giving the right static equilibrium configuration.

4.4.4 Equations of motion

Finally the partial differential equations for the contact cable become:

$$\begin{aligned} \mu\, v_{tt} = \; & -\eta_1 v_t + P_0 v_{xx} - EI v_{xxxx} \\ & + EA\left(v_{xx}u_x + v_x u_{xx} + \tfrac{3}{2}v_x^2 v_{xx}\right) - \mu g \\ & + \textstyle\sum_{m=1}^{ndrop} Fdrop_m \delta(x - xdrop_m) \\ & + \textstyle\sum_{m=1}^{nsup} Freg_m \delta(x - xsup_m) \\ & + Fc(t)\, \delta(x - speed \cdot t) \\ \mu\, u_{tt} = \; & -\eta_2 u_t + EAu_{xx} + EAv_x v_{xx} \end{aligned} \tag{4.41}$$

with boundary conditions

$$v(0) = v(L) = v_{xx}(0) = v_{xx}(L) = u(0) = u(L) = 0,$$

and the partial differential equations describing the motion of the catenary cable read:

$$\begin{aligned}
\mu_2\, v2_{tt} = \; & -\eta_1 v2_t + P_{02}\, v2_{xx} - EI_2\, v2_{xxxx} \\
& + EA_2 \left(v2_{xx} u2_x + v2_x u2_{xx} + \tfrac{3}{2} v2_x^2 v2_{xx} \right) \\
& - \mu_2\, g - \textstyle\sum_{m=1}^{ndrop} Fdrop_m \delta(x - xdrop_m) \\
& + \textstyle\sum_{m=1}^{nsup} Fsup_m \delta(x - xsup_m) \\
\mu_2\, u2_{tt} = \; & -\eta_2 u2_t + EA_2\, u2_{xx} + EA_2\, v2_x v2_{xx}
\end{aligned} \tag{4.42}$$

with boundary conditions

$$v2(0) = v2(L) = 1, \;\; v2_{xx}(0) = v2_{xx}(L) = u2(0) = u2(L) = 0.$$

In the above equations v and u are the variables that describe the vertical and longitudinal motions respectively of the contact cable, $v2$ and $u2$ are the variables that describe the vertical and longitudinal motions respectively of the catenary cable. η_1 and η_2 are the damping coefficients for vertical and longitudinal motions (we simplify by assuming that the vertical damping is purely due to wind friction, whereas the longitudinal damping is purely due to material friction within the cables). The damping in overhead line systems is extremely low and we have only included it as small viscos damping in our modelling. $ndrop$ is the number of droppers, $Fdrop_m$ is the force in dropper number m, and $xdrop_m$ is the location of the m'th dropper. $nsup$ is the number of supports (exclusive the end supports), $Freg_m$ describes inertia forces and apparent stiffness forces of the registration arms, and $xsup_m$ is the location of the m'th support. Fc is the contact force between contact cable and pantograph. $Fsup_m$ is support force number m.

4.4.5 Discretisation

We shall discretise the partial differential equations by using a finite element method in space and a finite difference method in time. First we describe the spatial finite element approach.

finite element approach

In this subsection we shall in detail describe the finite element discretisation of the equations of motion of the contact cable, (4.41). The calculations for the catenary cable are similar, and we will therefore not go through these.

First we rewrite (4.41) in its weak formulation:

$$\begin{aligned}
&\textstyle\int_0^L (\mu\, v_{tt} + \eta_1 v_t)\, W1\, dx + \int_0^L EIv_{xx} W1_{xx}\, dx \\
&\qquad \textstyle + \int_0^L P_0 v_x W1_x\, dx + \int_0^L EA\left(v_x u_x + \frac{1}{2}v_x^3\right) W1_x\, dx = \\
&\qquad \textstyle - \int_0^L \mu g W1\, dx + \sum_{m=1}^{ndrop} Fdrop_m W1(xdrop_m) \\
&\qquad \textstyle + \sum_{m=1}^{nsup} Freg_m W1(xsup_m) \\
&\qquad + FcW1(speed \cdot t) \\
&\qquad - \left[EI\left(v_{xxx}W1 - v_{xx}W1_x\right)\right]_0^L + \left[P_0 v_x W1\right]_0^L \\
&\qquad \textstyle + \left[EA\left(v_x u_x r + \frac{1}{2}v_x^3\right) W1\right]_0^L \\
&\textstyle\int_0^L (\mu\, u_{tt} + \eta_2 u_t)\, W2\, dx + \int_0^L EAu_x W2_x\, dx + \\
&\qquad \textstyle\int_0^L \frac{EA}{2} v_x^2 W2_x = \left[EA\left(u_x W2 + \frac{1}{2}v_x^2 W2\right)\right]_0^L .
\end{aligned} \tag{4.43}$$

$W1$ and $W2$ are the test functions for the vertical and longitudinal equations respectively. By demanding $W1(0) = W1(L) = W2(0) =$

$W2(L) = 0$, the weak formulation finally becomes:

$$\begin{aligned}
&\textstyle\int_0^L (\mu\, v_{tt} + \eta_1 v_t)\, W1\, dx + \int_0^L EI v_{xx} W1_{xx}\, dx \\
&\qquad + \textstyle\int_0^L P_0 v_x W1_x\, dx + \int_0^L EA \left(v_x u_x + \frac{1}{2} v_x^3 \right) W1_x\, dx = \\
&\qquad - \textstyle\int_0^L \mu g W1\, dx + \sum_{m=1}^{ndrop} Fdrop_m W1(xdrop_m) \\
&\qquad + \textstyle\sum_{m=1}^{nsup} Freg_m W1(xsup_m) \qquad\qquad (4.44) \\
&\qquad + Fc W1(speed \cdot t) \\
&\textstyle\int_0^L (\mu\, u_{tt} + \eta_2 u_t)\, W2\, dx + \int_0^L EA u_x W2_x\, dx + \\
&\qquad \textstyle\int_0^L \frac{EA}{2} v_x^2 W2_x = 0.
\end{aligned}$$

Now we approximate $v(x,t)$ and $u(x,t)$ by $\hat{v}(x,t)$ and $\hat{u}(x,t)$:

$$\begin{aligned}
\hat{v}(x,t) &= \textstyle\sum_{i=0}^{nco} \left(b_i(t)\phi_i(x) + c_i(t)\psi_i(x) \right) \\
\hat{u}(x,t) &= \textstyle\sum_{i=0}^{nco}\ d_i(t)\theta_i(x),
\end{aligned} \qquad (4.45)$$

and we constraint ϕ_i and ψ_i to lie in the set of functions so that they posses the properties

$$\begin{array}{lll}
\phi_i(x\ ) & = 0 & ,\ x \leq x_{i-1} \\
\phi_i(x_i) & = 1 & \\
\phi_i(x\ ) & = 0 & ,\ x \geq x_{i+1} \\
\phi_i'(x\ ) & = 0 & ,\ x \leq x_{i-1} \\
\phi_i'(x_i) & = 0 & \\
\phi_i'(x\ ) & = 0 & ,\ x \geq x_{i+1}
\end{array} \qquad (4.46)$$

$$\begin{array}{lll}
\psi_i(x\ ) & = 0 & ,\ x \leq x_{i-1} \\
\psi_i(x_i) & = 0 & \\
\psi_i(x\ ) & = 0 & ,\ x \geq x_{i+1} \\
\psi_i'(x\ ) & = 0 & ,\ x \leq x_{i-1} \\
\psi_i'(x_i) & = 1 & \\
\psi_i'(x\ ) & = 0 & ,\ x \geq x_{i+1}
\end{array} \qquad (4.47)$$

and θ_i to lie in the set of functions so that it possesses the properties

$$\begin{array}{lll} \theta_i(x) & = 0 & , \ x \le x_{i-1} \\ \theta_i(x_i) & = 1 & \\ \theta_i(x) & = 0 & , \ x \ge x_{i+1}. \end{array} \tag{4.48}$$

The simplest choices then are ϕ_i, ψ_i, and θ_i, stated in chapter 2 for a uniform grid:

$$\phi_i(x) = \begin{cases} -\frac{2}{h_{i-1}^3}(x - x_i)^3 - \frac{3}{h_{i-1}^2}(x - x_i)^2 + 1 & , \ x_{i-1} \le x \le x_i \\ \frac{2}{h_i^3} \ (x - x_i)^3 - \frac{3}{h_i^2} \ (x - x_i)^2 + 1 & , \ x_i \le x \le x_{i+1} \\ 0 & , \ \text{otherwise} \end{cases} \tag{4.49}$$

$$\psi_i(x) = \begin{cases} \frac{1}{h_{i-1}^2}(x - x_i)^3 + \frac{2}{h_{i-1}}(x - x_i)^2 + (x - x_i), & x_{i-1} \le x \le x_i \\ \frac{1}{h_i^2} \ (x - x_i)^3 - \frac{2}{h_i} \ (x - x_i)^2 + (x - x_i), & x_i \le x \le x_{i+1} \\ 0 & , \ \text{otherwise} \end{cases} \tag{4.50}$$

$$\theta_i(x) = \begin{cases} \frac{1}{h_{i-1}}(x - x_i) + 1 & , \ x_{i-1} \le x \le x_i \\ -\frac{1}{h_i}(x - x_i) + 1 & , \ x_i \le x \le x_{i+1} \\ 0 & , \ \text{otherwise.} \end{cases} \tag{4.51}$$

The basis functions ϕ_i, ψ_i and θ_i are illustrated in figure 4.27.

Substituting (4.45) in (4.44) and skipping the 'hats' (that indicate that we are in the discrete system), we find the discretised equations

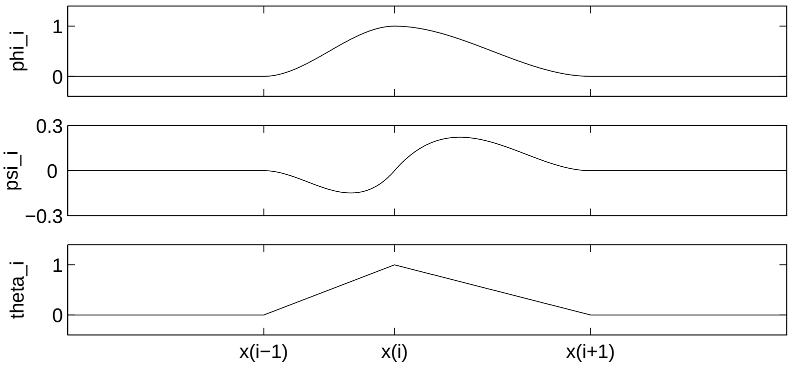

Figure 4.27: Basis functions ϕ_i, ψ_i and θ_i.

of motion as:

$$
\begin{aligned}
&\textstyle\int_0^L \sum_{i=0}^{nco} \Big((\mu \ddot{b}_i + \eta_1 \dot{b}_i)\phi_i + (\mu \ddot{c}_i + \eta_1 \dot{c}_i)\psi_i \Big)\, W1\, dx = \\
&\quad - \textstyle\int_0^L EI \sum_{i=0}^{nco} (b_i \phi_i'' + c_i \psi_i'')\, W1''\, dx \\
&\quad - \textstyle\int_0^L P_0 \sum_{i=0}^{nco} (b_i \phi_i' + c_i \psi_i')\, W1'\, dx \\
&\quad - \textstyle\int_0^L EA \sum_{i,k=0}^{nco} (b_i \phi_i' + c_i \psi_i')\, d_k \theta_k' W1'\, dx \\
&\quad - \textstyle\int_0^L \frac{EA}{2} \sum_{i,k,l=0}^{nco} (b_i \phi_i' + c_i \psi_i')\, (b_k \phi_k' + c_k \psi_k')\, (b_l \phi_l' + c_l \psi_l')\, W1'\, dx \\
&\quad - \textstyle\int_0^L \mu g W1\, dx + \sum_{m=1}^{ndrop} Fdrop_m W1(xdrop_m) \\
&\quad + \textstyle\sum_{m=1}^{nsup} Freg_m W1(xsup_m) \\
&\quad + Fc W1(speed \cdot t) \\
&\textstyle\int_0^L \sum_{i=0}^{nco} \Big((\mu \ddot{d}_i + \eta_2 \dot{d}_i)\theta_i \Big)\, W2\, dx = \\
&\quad - \textstyle\int_0^L EA \sum_{i=0}^{nco} (d_i \theta_i')\, W2'\, dx \\
&\quad - \textstyle\int_0^L \frac{EA}{2} \sum_{i,k=0}^{nco} (b_i \phi_i' + c_i \psi_i')\, (b_k \phi_k' + c_k \psi_k')\, W2'\, dx.
\end{aligned}
\tag{4.52}
$$

By successively letting the testfunction $W1$ run through ψ_0, ϕ_1, ψ_1,

ϕ_2, $\psi_2, \ldots$, ϕ_{nco-2}, ψ_{nco-2}, ϕ_{nco-1}, ψ_{nco-1}, and ψ_{nco} and successively letting the testfunction $W2$ run through θ_1, θ_2, $\theta_3, \ldots$, θ_{nco-2}, and θ_{nco-1} we obtain a system of $(2(nco+1)-2)+(nco+1-2) = (3nco-1)$ coupled, second order, ordinary differential equations in the $(3nco-1)$ variables c_0, b_1, c_1, b_2, c_2, b_3, $c_3, \ldots$, b_{nco-2}, c_{nco-2}, b_{nco-1}, c_{nco-1}, c_{nco} and d_1, d_2, $d_3, \ldots, d_{nco-2}$, d_{nco-1}, and we are done. (Note that b_0, b_{nco}, d_0, and d_{nco} are given by the boundary conditions).

Lets summarize: The equations of motion of the contact cable, given by the partial differential equations (4.41), was transformed to their weak formulation given by (4.44). With the approximation (4.45) and suitable basisfunctions (4.49),(4.50) and (4.51), the partial differential equations were transformed to a system of coupled ordinary differential equations. We then chose the testfunctions among those of the basisfunctions that satisfies the boundary conditions. The coefficients from the integrations are calculated once and for all. These integrations are performed in appendix B.

time discretisation

Modelling a complex system as a pantograph overhead line system involves a lot of approximations and uncertainties. In our opinion it is therefore not crucial to use very precise (and cpu expensive) time integration algorithms. We have chosen the simplest possible method, a so called forward Euler method which is just a finite difference method. This is characterized by the relation:

$$\ddot{x}(t = j \cdot dt) \approx \frac{\hat{x}_{j+1} - 2\hat{x}_j + \hat{x}_{j-1}}{dt^2},$$

where x is some variable, $\hat{x}_j$ is its discrete approximation at $t = j \cdot dt$, and dt is the time step size. For numerical stability there is an upper limit of the value of dt. Experiments have yielded $dt = hco/6500\ s$ to be suitable in our case, where hco is the numerical value of the length of the elements in the finite element discretisation of the contact cable. (Note: We use the same or a finer grid for the contact cable than for the catenary cable).

4.5 Pantograph modelling

Knowledge of the dynamical behaviour of the pantograph is quite important to be able to describe (and predict) the pantograph overhead line system dynamics in numerical simulations. This section considers the lumped mass models that are generally adopted for describing the dynamics of asymmetric and symmetric pantographs.

Pantographs are often designed and optimised for a specific overhead line system. A pantograph configured to operate on a railway line with one type of overhead line system does not necessarily operate satisfactorily with other types of overhead line systems. Especially the DC and the AC pantographs are fundamentally different, and operation of a DC pantograph on an AC overhead line system is liable to cause dangerous levels of contact wire displacements.

Setting up the exact nonlinear equations of motion of a pantograph is not only a pretty tough task in itself — it's also complicated by the fact that different parameters for describing some of the important details of the design of the pantograph, are very difficult to estimate. It is hard obtaining reliable data.

For investigations with an *existing* pantograph it is, in our opinion, much better to perform dynamic measurements with the pantograph, and then fit parameters of a relatively simple pantograph model with the results from the experiments. The disadvantages with this approach is that the process of parameter identification puts constraints on the complexity of the pantograph model. Besides the procedure is unsuitable for investigations of *nonexisting* pantographs (i.e. for instance in the design process of a pantograph). We would have preferred to achieve the pantograph model data for our simulations from such an experimental approach. However, due to mainly time

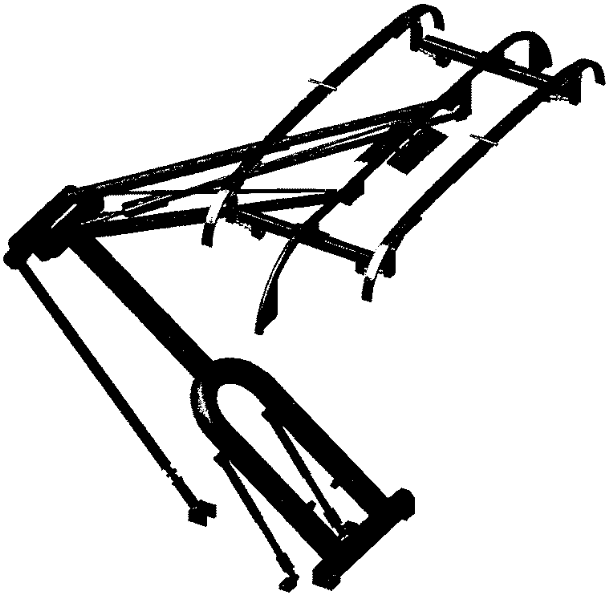

Figure 4.28: The SCHUNK WBL88 pantograph.

restriction reasons this has not been possible. Instead we have got the data for our simple pantograph models from reports, pantograph-vendors, railway engineers, and other researchers in this field, who have performed experiments; [7], [14], [31] and [6].

In figure 4.28 and 4.29 is seen the asymmetric SCHUNK WBL88 pantograph, which is used for the swedish X2 (X2000) train and the danish ER4 train. This would have been the most relevant pantograph to include in our simulations. Unfortunately we have not been able to get satisfactory data for this pantograph. Instead we have then experimented with data for other pantograph models, and chosen a model of the DSA350S pantograph for most of our numerical simulations. Of the different pantograph models we have tried, this is by far the one yielding the most favourable behaviour in our simulations.

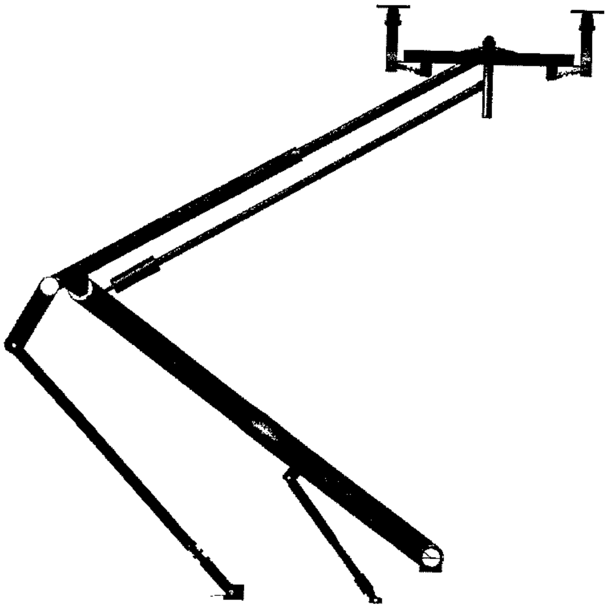

Figure 4.29: The SCHUNK WBL88 pantograph, side view.

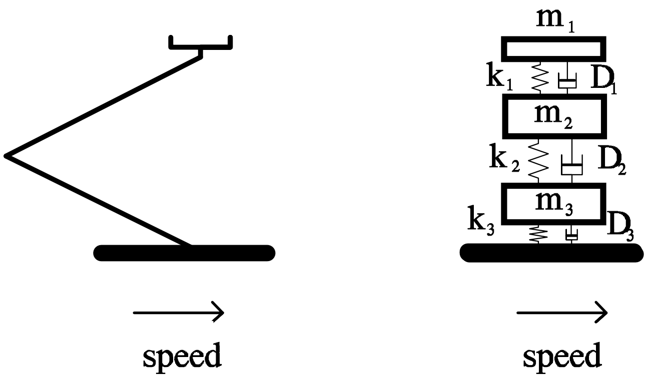

Figure 4.30: Lumped 3-mass model of asymmetric pantograph.

Our simple pantograph models only consider vertical motion. Obviously this is a simplification since the motion of the pantograph head will have composants in the directions of the contact cable (longitudinally) and perpendicular to the contact cable (horizontally). We believe it's reasonable to neglect the longitudinal composant. The horizontal composant is harder to ignore. Lesser et al [32] find that the rotational motion of the pantograph head in the direction transverse to the travel of the pantograph is superior to all the other motions, since the stagger of the contact cable excites this motion. Coupling between this motion and vertical motion is then important. In the end of this section we will show how the pantograph model can be modified to include this motion. It should be relatively simple; however we have not had the time for it. The simple pantograph models we adopt, only describe vertical motion.

We would like to stress that to model the vertical dynamics of an asymmetric pantograph this way, at *least* a lumped 3-mass model is necessary, whereas the vertical rigid body motion of a symmetric pantograph takes at least a lumped 2-mass model. In figure 4.30 we have indicated how the lumped masses in the discrete model should be associated with the physical pantograph as: head mass,

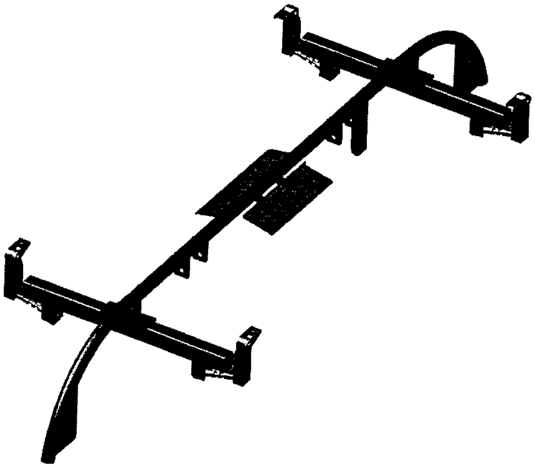

Figure 4.31: The pantograph head.

upper frame mass, and lower frame mass. In figure 4.31 the pantograph head is seen. Figure 4.32 shows the time response from experiments with the asymmetric Brecknell-Willis "high-speed" pantograph taken from [13]. The left graph corresponds to low-frequency excitation and the right graph corresponds to excitation above the first resonant frequency. Note that for low frequencies the upper and lower frame arms are in phase with the input signal while the pantograph head is out of phase. For frequencies above the first resonant frequency, the pantograph head and the upper frame arm are in phase with the input signal while the lower frame arm is out of phase. This means that a 2-mass model, which has only a single frame mass, will not even be able to describe the vertical *rigid body* motion of the asymmetric pantograph. This is the typical scenario. For symmetric pantographs, however, the situation is different since the upper and lower frame arms are more constrained to each other. In this case a single lumped mass is adequate to describe the vertical rigid body motion of the frame dynamics.

Taking a look at figure 4.28 and 4.29 again reveals that there is a

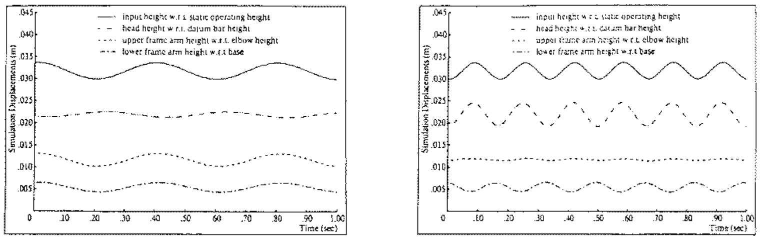

2.5 Hz Simulation Time Response

6.0 Hz Simulation Time Response

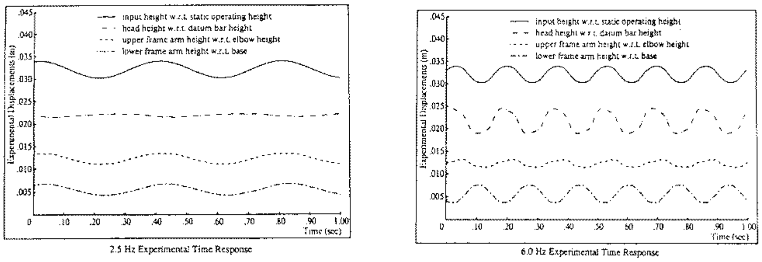

2.5 Hz Experimental Time Response

6.0 Hz Experimental Time Response

Figure 4.32: Time response of Brecknell-Willis "high-speed" pantograph. From [13].

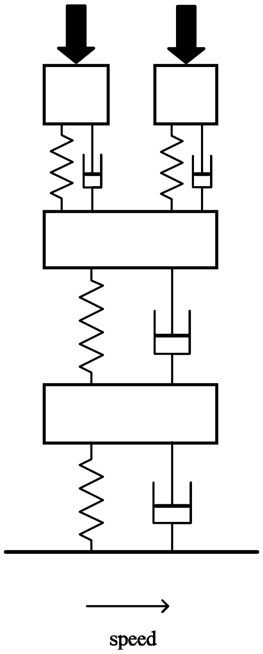

Figure 4.33: Lumped mass pantograph model where the head mass is divided into two masses to describe the separation of the contact strips.

certain distance between each contact strip. This can be important to include in the model since the unwishable contact slips between the pantograph and the contact cable tend to happen at certain points. Thus, the fact that there is this distance between the contact strips has a positive effect on the interactions (the two contact strips don't hit the critical points at the same time). To include the distance between the contact strips in the pantograph model, the head mass (and the corresponding spring and damper) is divided into two masses (and two springs and dampers) describing front and rear part of contact head. See figure 4.33.

As an extra detail we also include extra masses for the contact strips.

I.e. these are described by a spring and a dashpot connecting a little mass. The spring rate corresponds to the flexibility of the contact strips. The mass is not the physical mass but a 'numerical' mass, tuned so that spring and mass together model the first deformable mode of the contact strip. This is of course a very rough representation of the deformability of the contact strips. The spring rate, k_c, modelling the contactstrips of the DSA350S pantograph have been measured by Andrea Collina and colleagues at Politecnico di Milano in Italy. They found $k_c = 50.000\ N/m$. With a frequency of the first deformable mode at approximately $f_1 = 80\ Hz$ this leaves the numerical mass as $m_n = 0.2\ kg$. We use these data for all our pantograph models.

All together we end up with the pantograph model seen in figure 4.34. In table 4.1 is listed data for 4 lumped mass pantograph models: the SNFC GPU 25 kV pantograph, two different models of the Dorniers DSA350S pantograph, and a set of data for a lumped 2-mass model of the SCHUNK WBL88 pantograph (which is insufficient, as described above). The parameters correspond to figure 4.30.

4.5.1 Inclusion of rotation of pantograph head

We will here consider the modifications of the simple pantograph model, necessary to take into account the rotational motion of the pantograph head. The best approach would be first to identify the parameters of the 3-mass pantograph model — then to modify the model as described below.

Taking a look at figure 4.28 again, we see that the rotation of the contact head is connected with torsion of the upper frame linkage. The flexibility of the upper frame linkage can be estimated or, even better, measured. The simple pantograph model can then be modified as sketched in figure 4.35. On the left the pantograph is seen from

---

[1] $k_1(x) = 4400 + 2.364 \cdot 10^7 x^2 - 7.364 \cdot 10^1 0 x^4\ N/m$.

[2] ascending/descending; additional frame damping ±17 N.

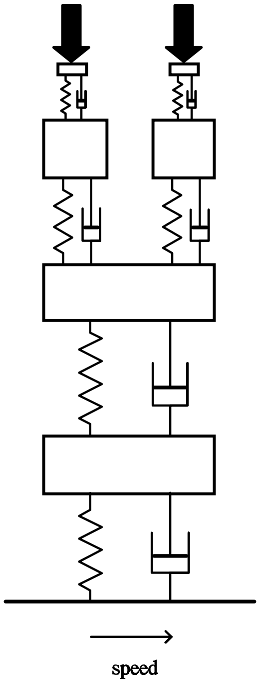

Figure 4.34: The final lumped mass pantograph model which also includes a very rough description of the contact strip deformability.

	GPU 25 kV	DSA350S	DSA350S	WBL88
		ORE	Milan	
m_1 $[kg]$	7.0	5.9	6.0	6.6
k_1 $[\frac{N}{m}]$	9000	2650	4500	4400-6800 [1]
D_1 $[\frac{Ns}{m}]$	0	0	20	75.6
m_2 $[kg]$	8.1	7.1	9	19.7
k_2 $[\frac{N}{m}]$	1200	10000	7000	10000
D_2 $[\frac{Ns}{m}]$	0	0	7	0/63.5 [2]
m_3 $[kg]$	23.0	11.8	5.0	-
k_3 $[\frac{N}{m}]$	0	80	500	-
D_3 $[\frac{Ns}{m}]$	140	70	70	-
k_{ae} $[\frac{Ns^2}{m^2}]$	0.018	0.0066	0.0066	0.00648
$Fstat$ $[N]$	70	80	80	70

Table 4.1: Data for lumped mass pantograph models.

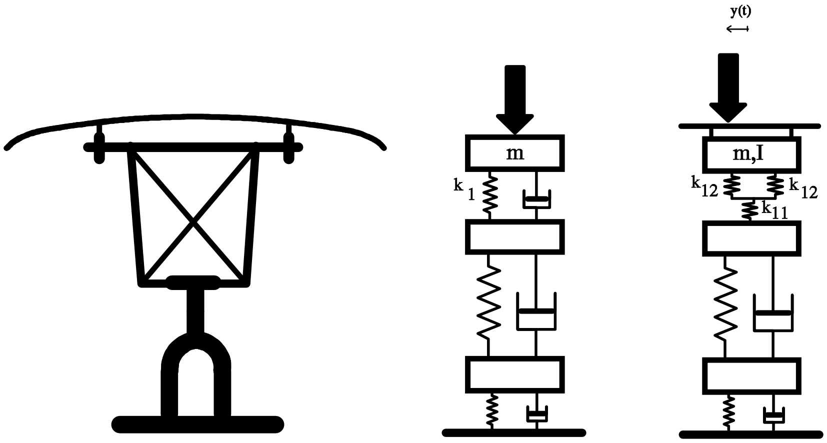

Figure 4.35: Left: front view of pantograph. Middle: The lumped 3-mass model. Right: The rigid body pantograph model with inclusion of a description of the rotational motion of pantograph head.

the front; in the middle the original discrete, lumped 3-mass model; and on the right is shown the discrete model when rotation of the pantograph head is included. The only function of the top bar in the model is to distribute the contact force to the pantograph head body right, according to the geometry of the pantograph. The top bar is infinitely rigid as well as the connections from it to the pantograph head body. Note that it is necessary to know the relevant moment of inertia of the pantograph head. k_{12} describes the flexibility of the upper frame linkage and k_{11} the flexibility of the connecting bar between the upper frame linkage and the contact head, see figure 4.28. The spring rate from the original discrete 3-mass pantograph model, k_1, is related to k_{11} and k_{12} as

$$k_1 = \frac{2k_{11}k_{12}}{k_{11} + 2k_{12}}.$$

It is also necessary to know the distance between the attachment points of the upper frame linkage to the pantograph head and between the attachment points of the contact strips to the pantograph head. Finally we have in figure 4.35 indicated the horizontal variation of the position of the contact point (the effect of the stagger).

4.6 Coupling of pantograph to catenary system

By far the most difficult part in the process of modelling the pantograph catenary system has been the coupling of the two dynamical systems. The discussion of the coupling of discrete and continuous systems in chapter 2 was mainly based on our experiences from the process of coupling the pantograph and the catenary system.

The coupling involves two tasks: Computation of the contact force and handling of the moving, localized forcing of the contact cable.

4.6.1 Contact force

In [35] and [37] theoretical considerations on the contact force and the coupling are made. One of the authors has later admitted that all these considerations failed when they were adopted in simulations.

In our opinion the correct contact force can be decided from two simple criterias (Newton's second law):

- The force from the contact cable to the pantograph should equal the force from the pantograph to the contact cable.
- The position of the contact point on the pantograph should equal the position of the contact point on the contact cable.

Decision of the contact force from these two criterias involves an iterative procedure between each time step to obtain convergence of the contact force on the pantograph and on the contact cable and of the contact point for the pantograph and for the contact cable.

An early version of our developed simulation program included a Newton-Raphson procedure, [2], for the decision of the contact force. This was rather cpu-time consuming and we therefore considered alternative approaches. We ended with an approach in which a very stiff spring between the pantograph and the cable describes the contact. This gives results in good harmony with the more correct iterative procedure — and it is *much* faster.

4.6.2 Discretisation of the dirac delta function

The dynamics of the pantograph is coupled to the motion of the contact cable and appears as a moving, discrete force in the partial differential equation for the motion of the contact cable (4.41). In this section we shall discuss the handling of this term when we discretise.

At first glance, compared to other discretisation methods, the finite element method seems very well suited to handle such localised

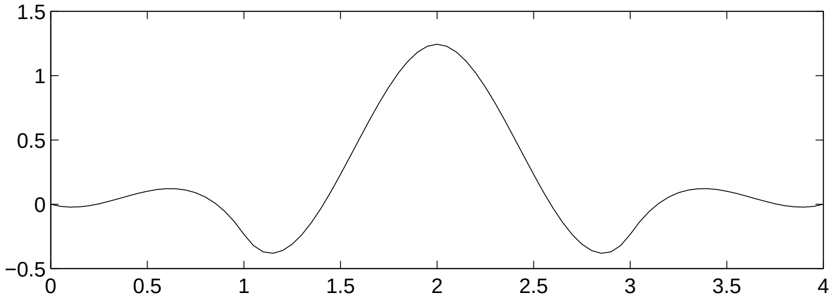

Figure 4.36: Expansion of Dirac delta function

forces, since dirac's delta function has the property:

$$\int_{-\infty}^{\infty} F(x)\delta(x-x_0)\,dx = F(x_0).$$

Thus, in principle no approximations of the dirac delta function has to be made to handle the term for the pantograph force. However, when simulating we observated some motion which clearly was dependent of the element lengths; i.e. a numerical, non-physical phenomenon. A more thorough investigation identified the delta function as the source of the trouble. We illustrate the problem by expanding a dirac delta function after our basis functions:

$$\delta(x-x0) \approx D(x-x0) = \sum_{i=0}^{n} (c_i\phi_i + d_i\psi_i)$$

In figure 4.36 we have depicted the expansion of $\delta(x-2)$ using (4.49) and (4.50) with $n = 4$ and $h_i = h = 1$. The troublesome oscillations near the singularity are clearly seen. In the equations of motion of the contact cable a dirac delta function appears. The poor representation of the dirac delta function gives rise to the high frequency, numerical oscillations destroying the overall picture in the pantograph overhead line simulations. The problem is somewhat reduced by refining the discretisation. Not quite to an extent that makes it acceptable if the cpu-time for each simulation is included in the considerations.

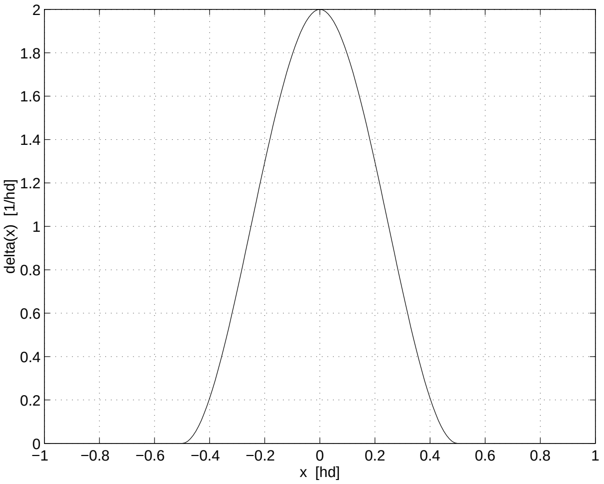

Figure 4.37: Approximation of the dirac's delta function.

Instead we approximated the dirac's delta function by smearing it out. We have chosen the approximation as

$$\delta(x) \approx \begin{cases} -\frac{32}{hd^4}(x)^3 - \frac{24}{hd^3}(x)^2 + \frac{2}{hd}, & -\frac{hd}{2} \le x \le 0 \\ \frac{32}{hd^4}(x)^3 - \frac{24}{hd^3}(x)^2 + \frac{2}{hd}, & 0 \le x \le \frac{hd}{2} \\ 0 \quad , & \text{otherwise} \end{cases} , \tag{4.53}$$

where hd is then a parameter for the width of the pulse shaped approximation of the delta function. See figure 4.37. The wider the pulse is, the more smooth is then the approximation and the better the pulse is expanded in the basis functions. On the contrary, too wide a pulse might of course make the discretised model unable to model physical phenomena due to the pantograph force, which in reality *is* very localised. Thus, we have to find a suitable compromise for this parameter, acceptable for both physics and numerics. We have experimented somewhat and have found $hd = 2.5hco$ to be suitable, where hco is the length of the elements in the finite element discretisation of the contact cable.

4.7 Results

We shall now present our numerical results. Where nothing else is stated, the pantograph model is given by the 'Milano' data for the DSA350S pantograph. The presentation of our results will be divided into 5 subsections. First we will discus the presag of the contact cable in the overhead line system. We shall then compare the importance for the pantograph overhead line system investigations of the 'small terms' in the cable equations. We have a short subsection on the (non)importance of the registration arm dynamic mass. The breaking sound barrier like phenomenon near the critical speed is investigated, and finally we consider the effect of the spatial discretisation versus the effect of filtering of the output signal.

4.7.1 Presag

In section 4.3 we mentioned that the simple configuration is softer in the middle of a span than at the ends. We illustrate that in figure 4.38, where we for one (arbitrary) span have depicted the quasistatic uplift of the contact cable relative to the static equilibrium configuration, at the position of a constant, upwards pointing force of 100 N. Or to put it another way, in the figure we have depicted the relative uplift of a 100 N biased pantograph, in the span given by 420 $m \leq x \leq$ 480 m, for an infinitely slow train speed. The grid in the figure indicates the position of the droppers.

The variation of the flexibility of the contact cable over the span is clearly seen. Note that the quasistatic uplift in the most soft place is more than twice as large as the quasistatic uplift the most stiff place. It is seen that there are local minima in the quasistatic uplift at the positions of the droppers. Especially the droppers near the masts give rise to very hard spots.

We will now derive a simplified model for the overhead line system. We search for a stiffness per length, $k(x)$, such that the motion of

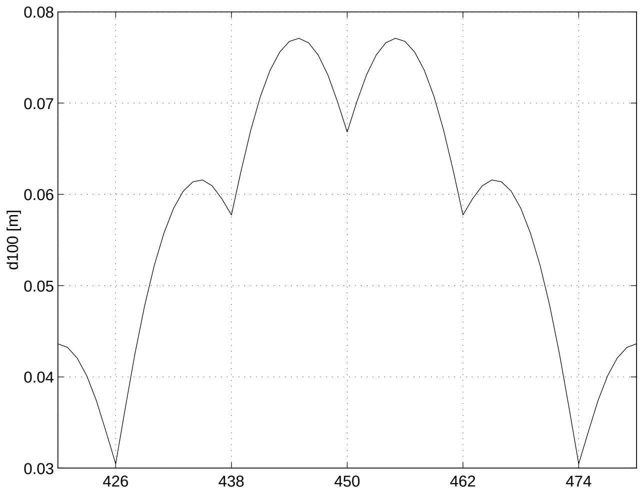

Figure 4.38: The quasistatic uplift of the contact cable relative to the static equilibrium position, for a upwards pointing force of 100 N.

the contact cable excited by a moving force can be approximated by the equation

$$\mu v_{tt} = P_0 v_{xx} - k(x)v + F_c \delta(x - vt). \tag{4.54}$$

This model is of course only justified for performing fast, *rough* investigations, since the model neglects inertia of catenary cable, bending stiffnesses, nonlinearities, etc. By experimenting with the numbers we have found the stiffness per length $k(x)$ for this purpose given as

$$\begin{aligned} k(x) = \quad & \textstyle\sum_{i=1}^{nspan} (2064\,\delta(x - (\ 6 + (i-1)\cdot 60))) \\ & + \textstyle\sum_{i=1}^{nspan} (\ \ 512\,\delta(x - (18 + (i-1)\cdot 60))) \\ & + \textstyle\sum_{i=1}^{nspan} (\ \ 390\,\delta(x - (30 + (i-1)\cdot 60))) \\ & + \textstyle\sum_{i=1}^{nspan} (\ \ 512\,\delta(x - (42 + (i-1)\cdot 60))) \\ & + \textstyle\sum_{i=1}^{nspan} (2064\,\delta(x - (54 + (i-1)\cdot 60)))\,, \end{aligned} \tag{4.55}$$

where *nspan* is the number of spans. and the constants are spring coefficients and have units N/m.

We have been using the simplified model given by (4.54) and (4.55) to investigate if advantages could be obtained with an *asymmetric* presag of the contact cable, compared to the usual *symmetric* presag. We have found that only small improvements could be obtained by making the presag asymmetric. Anyway this is most of theoretical interest, since today most railway lines must be equally runnable from both sides. An asymmetric presag giving better performance for trains running in one direction is likely to give worse performance for trains running in the other direction.

In figure 4.39 we have depicted the altitude of the contact point at the position of a moving constant force of 80 N, travelling with 190 km/h, relative to the static equilibrium position, as calculated with the simplified model. In figure 4.40 we illustrate the corresponding result calculated for an overhead line system without presag, and with the dynamic contact force given by the coupled overhead line system and a pantograph. The similarities and the differences of the two results are clear. The simplified model predicts the overall motion but misrepresents the influence of the singularities at the positions of the droppers. Most important, it is seen that there is a phase shift of the two models. This is due to inertia effects of the catenary cable and of the pantograph, which is neglected in the simplified model.

In the design parameters for the danish overhead line system, the size of the presag is prescribed as $\frac{1}{1000}$ of the span length, which yields 0.06 m. In figure 4.41 we have illustrated the altitude of the contact point at the position of the pantograph travelling with 190 km/h, calculated with a model of an overhead line system with a 0.06 m presag. It is seen that the amplitudes of the variations of the altitudes of the contact points are of same order in the system with the 6 cm presag and in the system with no presag.

In figure 4.42 is illustrated the altitude of the contact point over

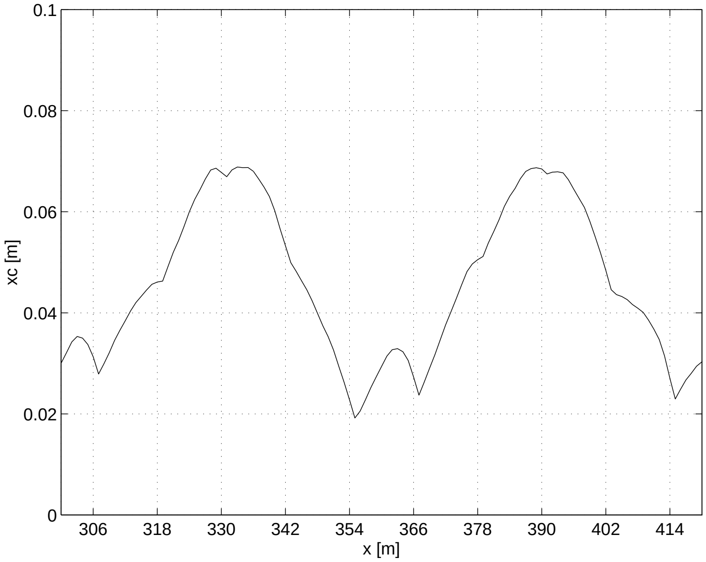

Figure 4.39: The uplift of the contact cable relative to its static equilibrium position at the position of the moving force of 80 N, calculated with the simplified model.

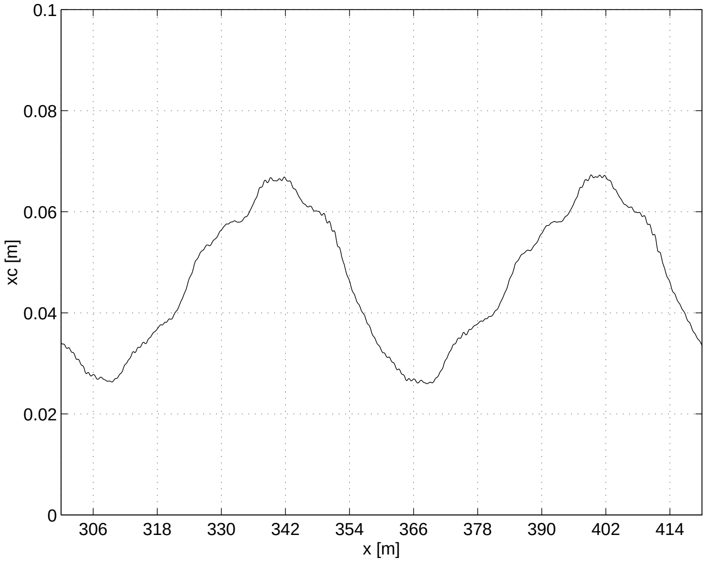

Figure 4.40: The altitude of the contact cable at the position of a moving pantograph, calculated with a full model of an overhead line system without presag.

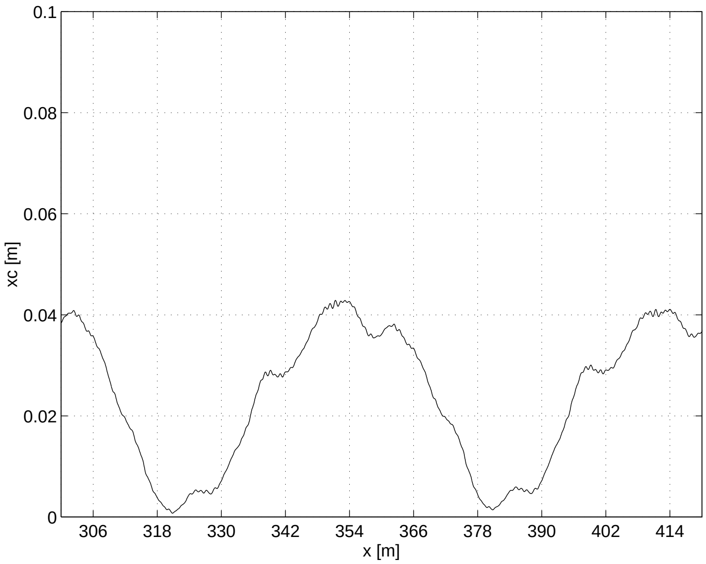

Figure 4.41: The altitude of the contact cable at the position of a moving pantograph, calculated with a full model of an overhead line system with a 6 *cm* presag.

3 spans, calculated with full models of overhead line systems with presags from top to bottom of 0 *cm*, 2 *cm*, 4 *cm*, and 6 *cm*, and the pantograph travelling with 190 *km/h*. The comparison of the 4 different signals reveals that

- The 0 *cm* presag configuration gives large amplitude, relatively low frequent variations of the altitude of the contact point.
- The 2 *cm* presag configuration gives lower amplitudes and still low frequent variations of the altitude of the contact point.
- The 4 *cm* presag configuration signal has same order of magnitude amplitude as the 2 *cm* presag configuration signal, but high frequent motion is introduced.
- The 6 *cm* presag configuration gives variations of the altitude of the contact point with large amplitudes *and* a high frequency content.

In figure 4.43 we have depicted the contact force signals corresponding to the contact point altitude signals in figure 4.42. We admit it is a bit difficult looking at this figure (it is easier seen with all signals depicted simultaneously with different colours, in one graph, which unfortunately was not possible for this thesis). It is, however, clear from the figure that the performance of the normal overhead line system with the 6 *cm* presag is inferior to the other ones.

One way of measuring the quality of an overhead line system is by studying the statistical occurrences of contact losses; another is by studying the mean value M and the standard deviation σ of the contact force signal. A measure for the contact quality is the relation $M - 3\sigma$. It is a necessary but not sufficient demand that $M - 3\sigma > 0$ to obtain a satisfactory contact quality. In tables 4.2 and 4.3 we have listed the mean values M_0, M_2, M_4, and M_6 and the standard deviations σ_0, σ_2, σ_4, and σ_6 of the contact force signals for the overhead line systems with the specified presag, for the train speeds 140 *km/h*, 180 *km/h*, 190 *km/h*, 200 *km/h*, 210 *km/h*, 220 *km/h*, 230 *km/h*, and 240 *km/h*. The contact force signals were obtained with simulations of the pantograph travelling the distance of the first 10 spans of the overhead line systems, i.e. 600 *m*. From the table it

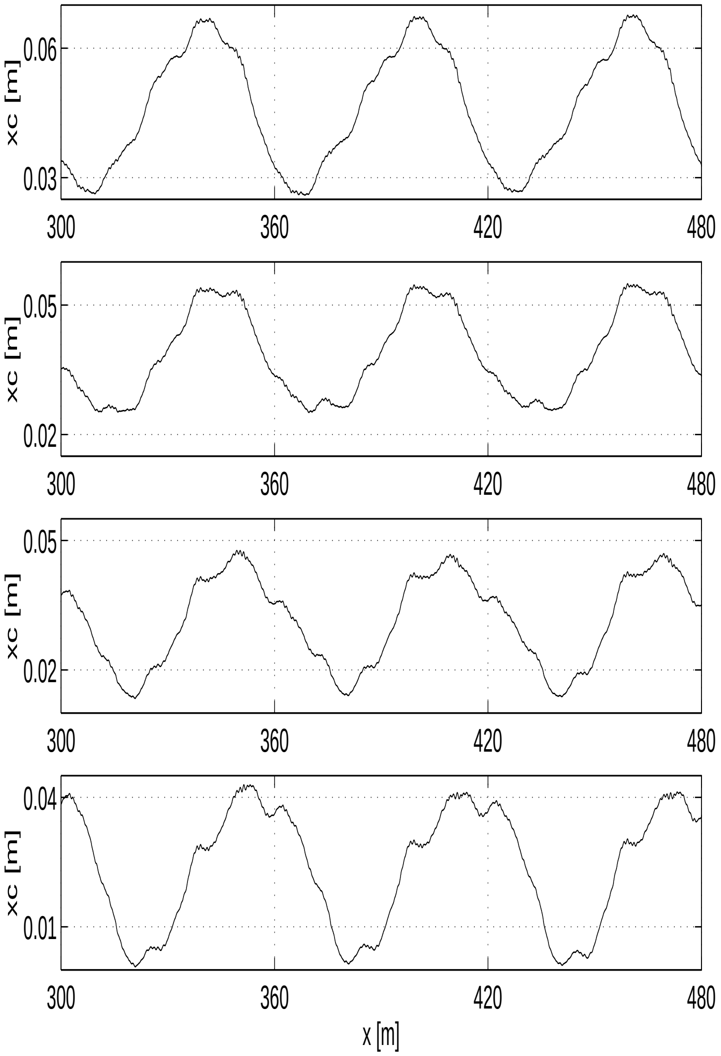

Figure 4.42: The altitude of the contact cable at the position of a moving pantograph, calculated with full models of overhead line systems with 1) no presag, 2) a 2 *cm* presag, 3) a 4 *cm* presag, and 4) the normal 6 *cm* presag.

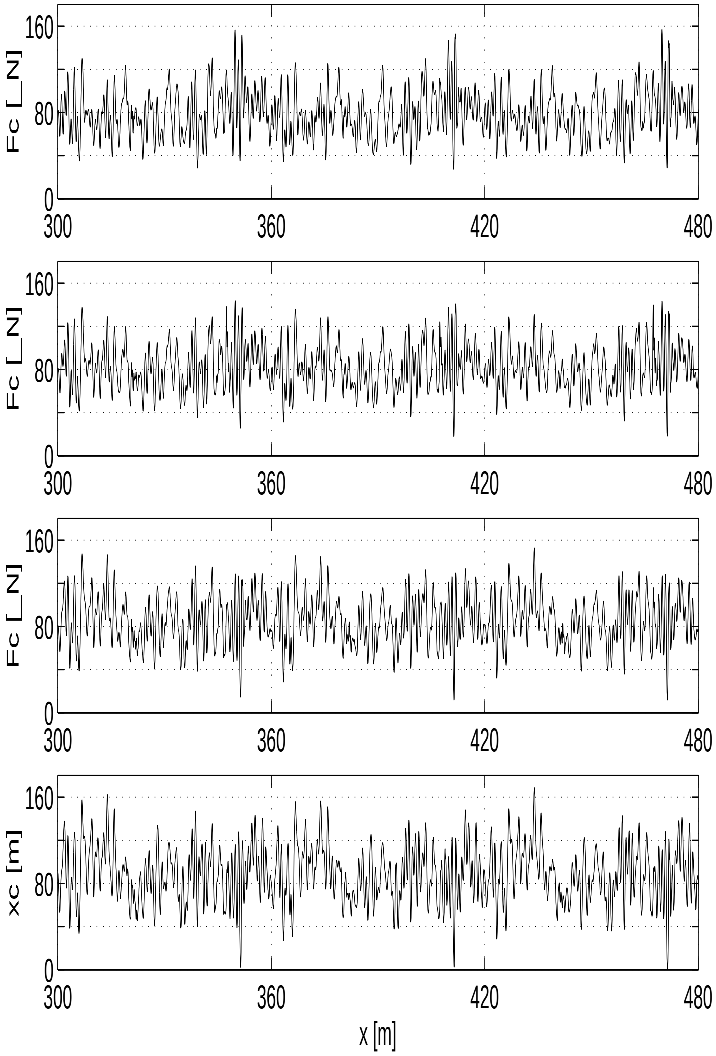

Figure 4.43: Contact force signals calculated with full models of an overhead line systems with 1) no presag, 2) a 2 *cm* presag, 3) a 4 *cm* presag, and 4) the normal 6 *cm* presag, corresponding to the variations of contact point altitudes seen in figure 4.42.

speed	M_0	M_2	M_4	M_6
km/h	$[N]$	$[N]$	$[N]$	$[N]$
140	73.10	76.38	79.94	82.58
180	77.48	80.67	83.69	86.90
190	78.89	82.13	85.18	85.44
200	80.09	83.33	86.40	89.70
210	81.37	84.53	87.52	90.74
220	83.72	86.81	89.78	93.35
230	85.36	88.32	91.34	94.67
240	86.94	89.95	92.81	95.94

Table 4.2: Mean values of contact force signals for different speeds and overhead line systems with no presag, a 2 cm presag, a 4 cm presag, and a 6 cm presag.

speed	σ_0	σ_2	σ_4	σ_6
km/h	$[N]$	$[N]$	$[N]$	$[N]$
140	15.70	14.42	14.31	15.22
180	24.03	23.73	25.16	27.81
190	21.65	21.42	23.58	27.41
200	21.99	20.40	22.50	26.96
210	22.34	22.70	26.44	31.29
220	32.06	32.16	33.50	35.11
230	33.06	32.70	34.35	36.23
240	36.70	36.46	35.26	35.96

Table 4.3: Standard deviations of contact force signals for different speeds and overhead line systems with no presag, a 2 cm presag, a 4 cm presag, and a 6 cm presag.

is seen that using the ratios of the mean values of the contact force signals over the standard deviations of the contact force signals as measure, the 2 *cm*-presag configuration is the preferable one of the above, slightly preferable to the configuration with no presag. Looking at the contact force signals, however, the configuration without presag is slightly preferable to the 2 *cm* configuration, since the latter at certain points is closer to experiencing contact losses.

Now, we *are* aware of the controversity of this result. Our remarks above concerning the amplitude and the frequency content of the contact point altitude signal heuristically explain the conclusion; with the introduction of the presag, the variation of the contact point altitude gets a high frequency content that makes contact losses more probable.

4.7.2 Importance of 'small terms'

We shall now study the importance for the pantograph overhead line system investigations of the 'small terms' in the equations for the cable motions. Our method of investigation is simply to switch on and off the different physical constants, performing some simulations, and compare the time series of the contact force.

Let us recall that the bending stiffness is the first small term that has traditionally been included in the modelling of the cables, thus changing the cable models from a linear string model to a linear beam model. The justification was that for investigations with train speeds approaching the *critical* speed (the propagation velocity of transversal waves, $\approx 413\ km/h$ for the considered overhead line systems), inclusion of the bending stiffness was important to satisfactorily describe the breaking sound barrier like phenomenon. We shall return to this in section 4.7.4. In this section we shall consider more realistic train speeds.

It turns out that in the speed range $140\ km/h - 240\ km/h$, which is relevant for the overhead line system used by the Danish State Railways, the inclusion of bending stiffness has very little significance. This corresponds to our expectations as referred to above, in our remarks about string models versus beam models. In figure 4.44 we have depicted the contact force signals over 2 spans, for the train speed equal to 280 km/h. The top graph shows the contact force obtained in the simulation with the full cable equations, and the bottom graph shows the contact force obtained in the simulation with the bending stiffness set to zero. It is seen that even at this high speed, the bending stiffness has very little significance for the appearance of the contact force signal.

However, we find that the *nonlinearities* do have some significance for the dynamics in the considered speed range. We illustrate it in figure 4.45, which shows times series of the contact force obtained from simulations with the train speed set to 230 km/h. In the upper graph we use the full equations for the cable motion, corresponding to (4.7). In the middle graph the axial stiffness is set to zero, $EA = 0$, corresponding to the linearised equation for the cable motion (4.3). In the bottom graph we have implied that the longitudinal motion can be neglected in the cable motion, corresponding to (4.9). It is seen that the contact force signal obtained with the linearised equation yields larger contact peaks and more contact losses than the contact force signal obtained with the full equation. The time series of the contact force from the simulation in which the geometrical nonlinearity term is included also differs from the time series solution of the full equations, but the differences are smaller. (Since we above have introduced mean value and standard deviation as mean of measure, we rattle off their values for the contact force signals in the figure: $M = 85.4\ N$ and $\sigma = 33.1\ N$ for the upper graph, $M_{EA=0} = 86.2\ N$ and $\sigma_{EA=0} = 33.0\ N$ for the middle graph where the nonlinearities are neglected, and $M_{u\equiv 0} = 87.0\ N$ and $\sigma_{u\equiv 0} = 34.2\ N$ for the bottom graph, where the longitudinal motion is assumed negligible. The corresponding values for the contact force signal found by setting the bending stiffness to zero are $M_{EI=0} = 85.5\ N$ and $\sigma_{EI=0} = 33.0\ N$ which is seen to be very close to those of the full ca-

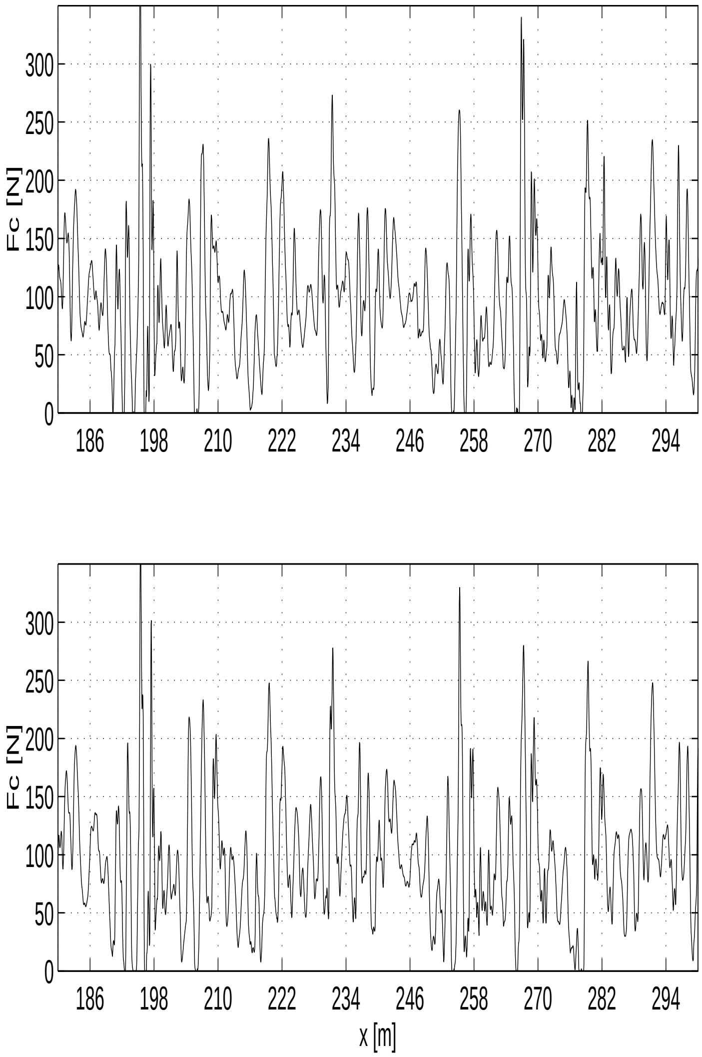

Figure 4.44: Comparison of contact force signals from simulations with the train speed 280 km/h. The top graph corresponds to the simulation with the full cable equations, and the bottom graph corresponds to the simulation with the bending stiffness set to zero.

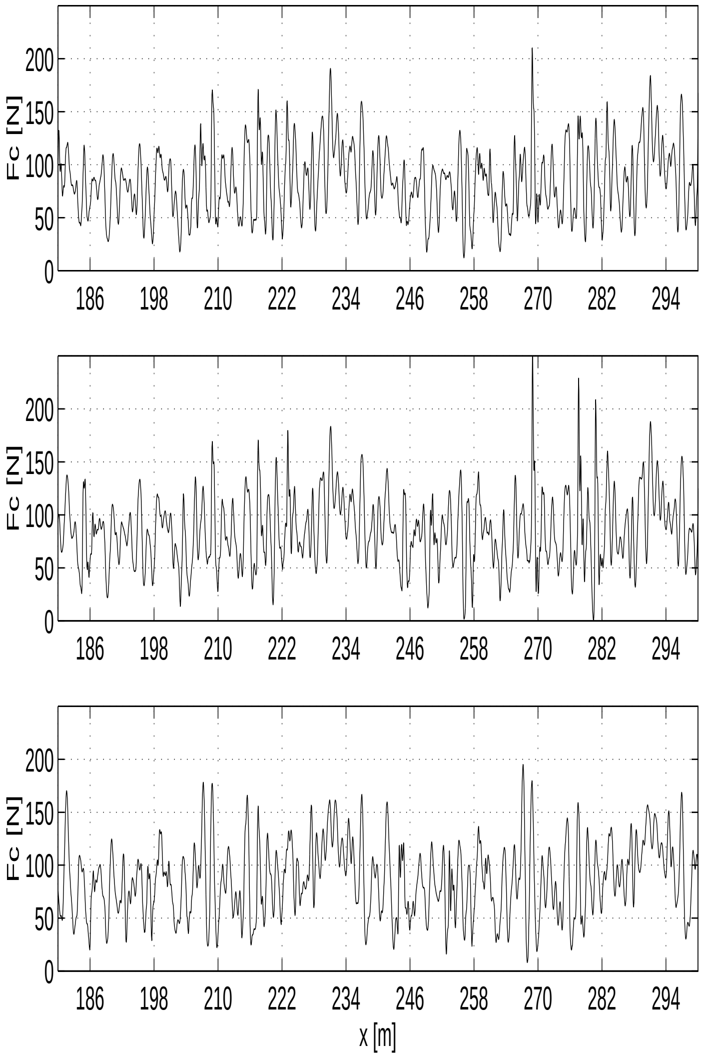

Figure 4.45: Contact forces. Cables modelled after (4.7) (top), (4.3) (middle), and (4.9) (bottom).

ble equations. The corresponding values for the contact force signal found by setting both the bending stiffness and the flexural stiffness equal to zero, and thus model the cables as linear strings, are found as $M_{EA=EI=0} = 86.3\ N$ and $\sigma_{EA=EI=0} = 32.3\ N$.)

We conclude that the nonlinearities have a positive effect on the dynamic interaction between the pantograph and the overhead line system. Our investigations have convinced us that in order to model the dynamic interaction between pantographs and overhead line systems, the cables should be modelled with the nonlinearities included. We find the bending stiffness to be less important.

However, the modelled overhead line system is designed for relatively low speeds. In systems where trains with higher speeds operate, the cables in the overhead line systems are thicker. Since the bending stiffness EI grows with the fourth power of the diameter of the cable, whereas the axial stiffness EA only grows with the second power of the diameter of the cable, the bending stiffness may be more important for these overhead line systems. We would suggest to include all the 'small terms', so that the cables in the overhead line systems are modelled by the equation (4.7).

Another argument for including the bending stiffness in the description is the choice of *numerical* method. If a finite element method is used for the spatial discretisation of the cable equations, the inclusion of the bending stiffness necessitates a choice of smooth basis functions. Referring to chapter 2 we have found that the convergence of the contact force signal is faster with smooth basis functions.

In section 4.2.2, where we considered the propagation of pulses on a single cable, we found that a very good approximation of the full cable equation could be obtained by describing the longitudinal motion by a 'quasistatic', local part plus the first few linear modes (possibly only *the* first linear mode). Unfortunately we have not had the time to test this approach for the pantograph overhead line system investigations. This should be investigated in the future since this would mean that the longitudinal motion could be included in the description in a very cheap way, in means of computer power.

4.7.3 Registration arm

We have found rather large discrepancies between our value for the dynamic mass modelling the inertia of the registration arms, and the values other researchers are using; discrepancies that are hard to explain by different designs. We also know that registration arms made of other materials, typically aluminium, are sometimes considered instead of the normal and heavier steel registration arms. We therefore investigate the importance of the size of the dynamics mass of the registration arm.

In figure 4.46 we compare the contact force signals obtained with our normal value for the dynamic mass of the registration arm, $mr = 0.51\ kg$, and obtained with a value of the dynamic mass we have found in [7] for an almost similar overhead line system, $mr = 1.12\ kg$. The speed for the simulations is 230 km/h. It is seen that at this speed the changed dynamic mass has some influence on the contact force signals near the supports (the positions of the registration arms are indicated by the grid). We have of course performed similar investigations for other speeds, and the conclusion is that the exact value for the dynamic mass is only of minor importance in the overall picture, but locally around the positions of the masts, a reduced mass of the registration arm can help significantly to improve the dynamics.

4.7.4 Behaviour near critical speed

In this section we shall investigate the breaking sound barrier like phenomenon, that is predicted for trains accelerating up to and past the critical velocity. The prediction of this phenomenon is illustrated in figure 4.47 in which the deflection of a linear string forced by a constant, moving force is depicted. The figure shows snapshots at

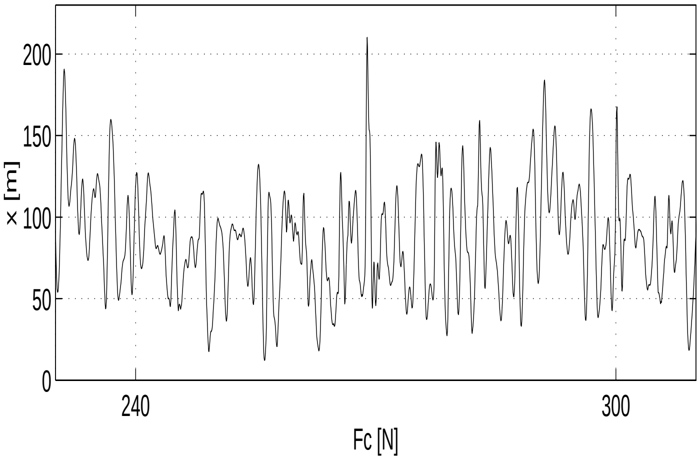

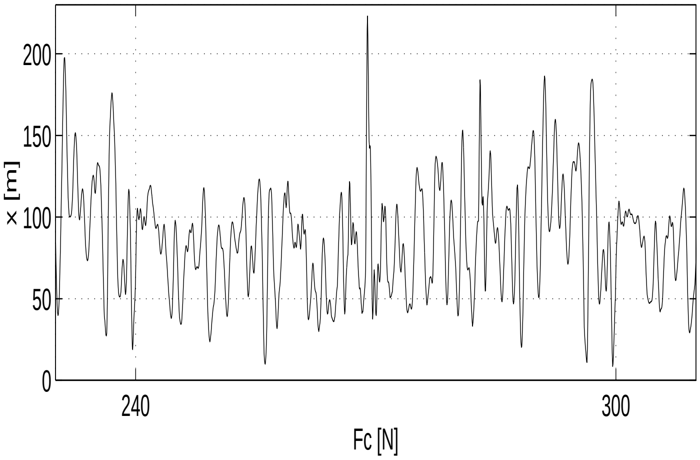

Figure 4.46: Contact forces. Top graph: Normal value of dynamic mass of registration arms, $mr = 0.51\ kg$. Bottom graph: dynamic mass of registration arms is set to $mr = 1.12\ kg$.

the same time $t = t_1$, for 4 different situations. In the top figure the force moves with a speed well below the wave propagation velocity of the string; this wave propagation velocity can in the figure be seen as the position of the front edge of the disturbed part of the string divided by the time t_1. In the second snapshot the force travels with a speed close to but lower than the wave propagation velocity. In the third snapshot the force moves with the speed equal to the wave propagation velocity; the position of the force and the front edge of the disturbed part of the string coincide. In the last snapshot the force moves with a speed larger than the wave propagation velocity. The disturbed part of the string is now behind the force. The change in situation from the second to the fourth snapshot is violent and the change takes place instantaneously when the speed goes from being subcritical to being supercritical. This is the so called breaking sound barrier like phenomenon, called this way since the situation corresponds to that of an aeroplane breaking the sound barrier.

With inclusion of the bending stiffness, i.e. switching from a linear string model to a linear beam model for the cables, the breaking sound barrier like phenomenon still appears, but the breaking is somewhat smoothed out, [4].

We will now study and compare the importance for the breaking sound barrier like phenomenon, of the inclusion of the bending stiffness and the nonlinearities in the cable motion equations. For this we have excited the overhead line system with a moving, constant force, instead of the dynamic contact force from a pantograph. We note (again) that the critical velocity is given by $v_c = \sqrt{\frac{P_0}{\mu}} \approx 114.8\ m/s \approx 413\ km/h$.

In figure 4.48 we have depicted the deflection of the contact cable relative to its static equilibrium configuration, as it appears when excited by a moving force with subcritical speed, $speed = 400\ km/h$. The position of the force is $speed \cdot t = 180\ m$ in all the snapshots, as indicated by the grid in the figure. The upper graph shows the deflection of the contact cable as found with the full cable equations (4.7);

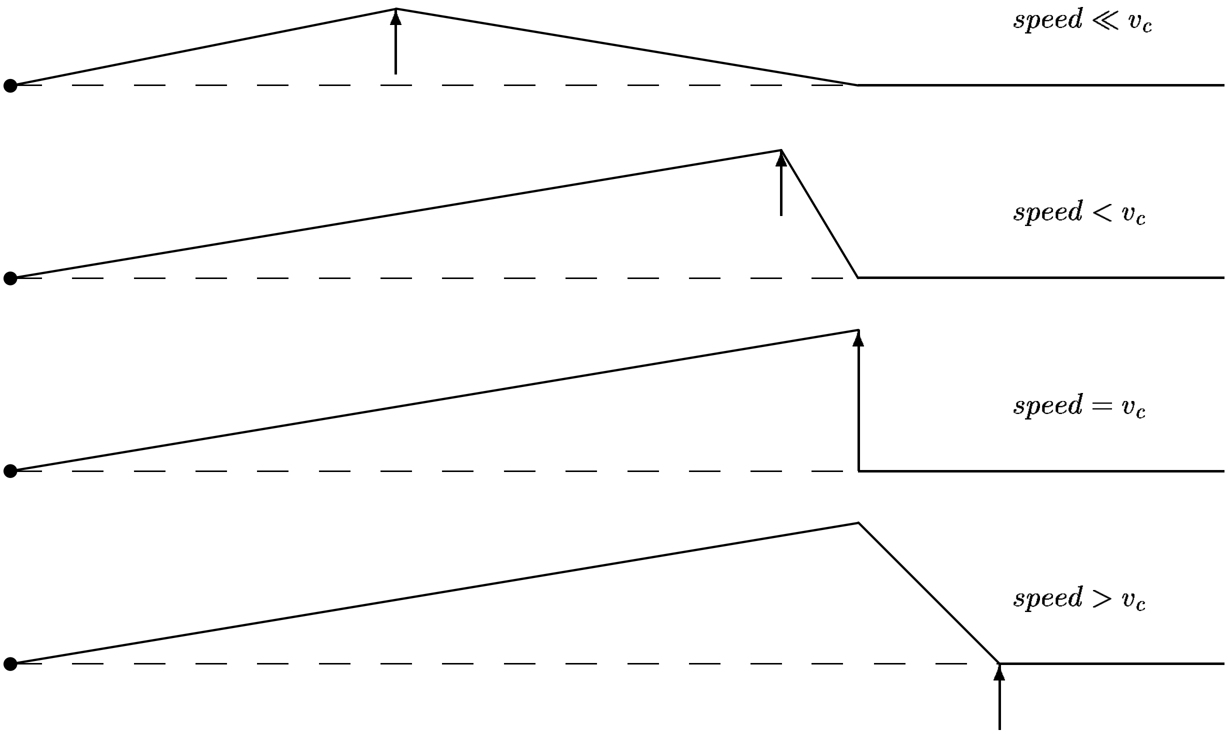

Figure 4.47: A string excited by a constant moving force with speed much lower than the critical speed, with the speed a little lower than the critical speed, with the speed equal to the critical speed and with the speed above the critical speed.

the second graph shows the deflection of the contact cable as found by modelling the cables as beams, i.e. with (4.3) as the cable equation; the third graph is the deflection of the contact cable as found by setting the bending stiffness equal to zero; and the bottom graph is the deflection of the contact cable as found by setting the bending stiffness *and* the flexural stiffness equal to zero and thus model the cables as strings. Remember that the speed of the force for the simulations was subcritical, and the appearance of the results correspond more or less to our expectations; the position of the force coincides with the position of the maximal cable deflection. Note that in the simulations where the nonlinearities were neglected, the deflection (nonsurprising) is larger than in the simulations where the nonlinear stiffening is included in the cable description. (Anyway, we are neglecting the unrealistic large cable deflections in these simulations. The overhead line system would probably have broken already).

In figure 4.49 we show the corresponding results, but now for a *supercritical* speed, $speed = 420\ km/h$. From this figure we have the following remarks:

- The deflection of the contact cable when this is modelled as a string (bottom graph) corresponds pretty well with our expectations from figure 4.47, except for a little discrepancy which we put down to numerical dispersion.
- The deflection of the contact cable when this is modelled as a beam (second graph) is rather similar to the deflection when this is modelled as a string (bottom graph). In both graphs the breaking sound barrier like phenomenon has taken place, and the pantograph is mainly travelling in front of the disturbed part of the contact cable.
- The deflection of the contact cable when this is modelled with the full cable equations (upper graph) and when the bending stiffness is set to zero are nearly identical. We conclude that the bending stiffness has very little influence on the result.
- In the cases which include the nonlinearities of the cables (first and third graphs), the deflection is, as expected, much smaller

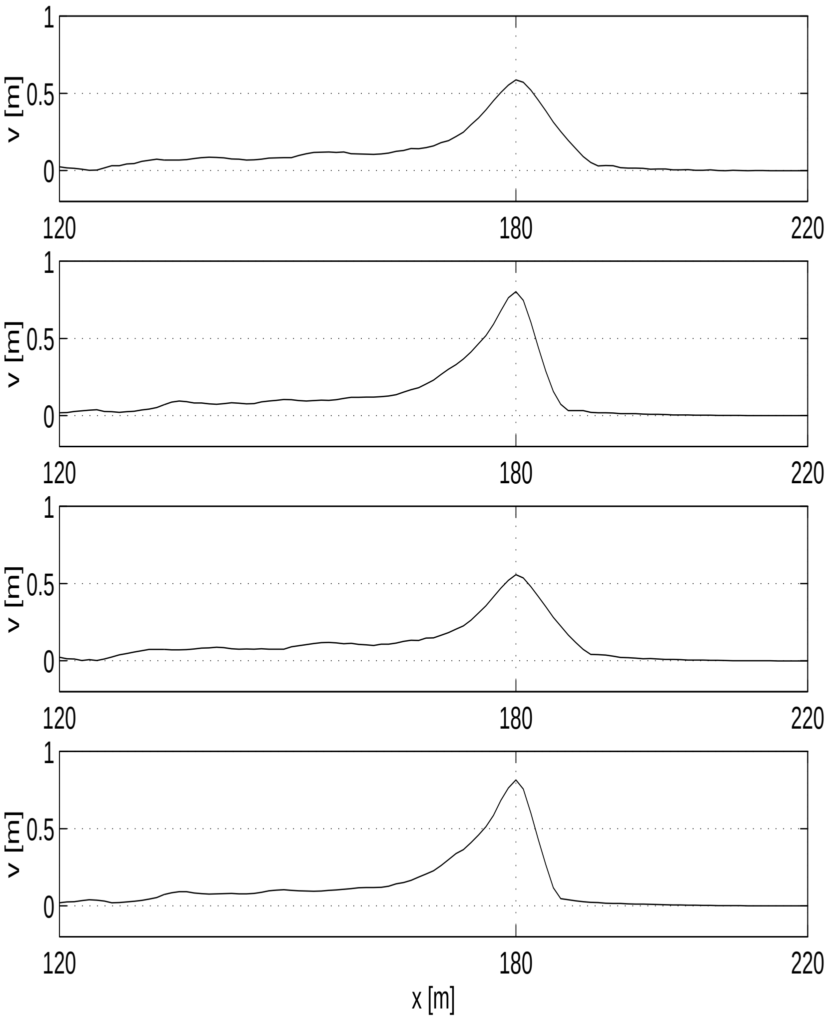

Figure 4.48: Deflection of the contact cable relative to its static equilibrium configuration, when excited by a constant, moving force with the *subcritical* speed, *speed* = 400 *km/h*. Upper graph: full cable equations (4.7). Second graph: cables modelled as beams, (4.3). Third graph: The bending stiffness set to zero. Bottom graph: cables modelled as strings, (4.1).

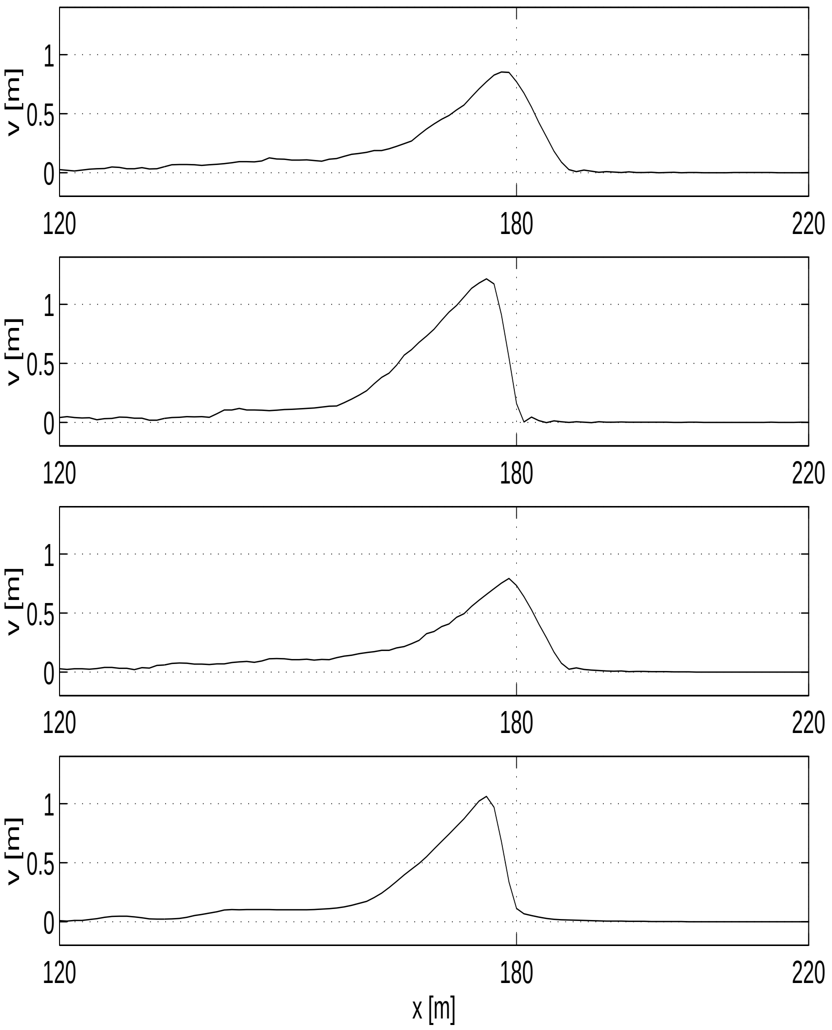

Figure 4.49: Deflection of the contact cable relative to its static equilibrium configuration, when excited by a constant, moving force with the *supercritical* speed, *speed* = 420 *km/h*. Upper graph: full cable equations (4.7). Second graph: cables modelled as beams, (4.3). Third graph: The bending stiffness set to zero. Bottom graph: cables modelled as strings, (4.1).

than in the cases where the nonlinearities of the cables are not included.
- In the cases which include the nonlinearities of the cables (first and third graphs), *the breaking sound barrier like phenomenon is only in its beginning state.* The position of the force is no longer coinciding with the position of the maximal contact cable deflection, as it was in case of the subcritical speed in figure 4.48, but is not mainly in front of the disturbed part of the contact cable either as it is in the second and fourth graphs, the *linear* cases. This indicates that the breaking sound barrier like phenomenon is smoothed out by the inclusion of the nonlinearities.

Inspired by the last remark above, we in figure 4.50 depict the deflection of the contact cable relative to its static equilibrium position, calculated with the full cable equations (thus including the nonlinearities) for 6 different speeds: $speed = 400\ km/h$, $speed = 410\ km/h$, $speed = 420\ km/h$, $speed = 430\ km/h$, $speed = 440\ km/h$, and $speed = 450\ km/h$.

From the figure we remark:

- The position of the force and the position of the maximum deflection of the contact cable coincide in the first two graphs, the two *subcritical* cases.
- In the last 4 graphs, the position of the force moves closer and closer to the front end of the disturbed part of the contact cable, the 'more supercritical' the speed is.
- We conclude that there *is* a breaking sound barrier like phenomenon for the overhead line system.
- We find that the breaking sound barrier like phenomenon is much smoother than predicted by the linear equations, and that there is *no way* this phenomenon can be described satisfactorily without including the nonlinearities of the cable motion.

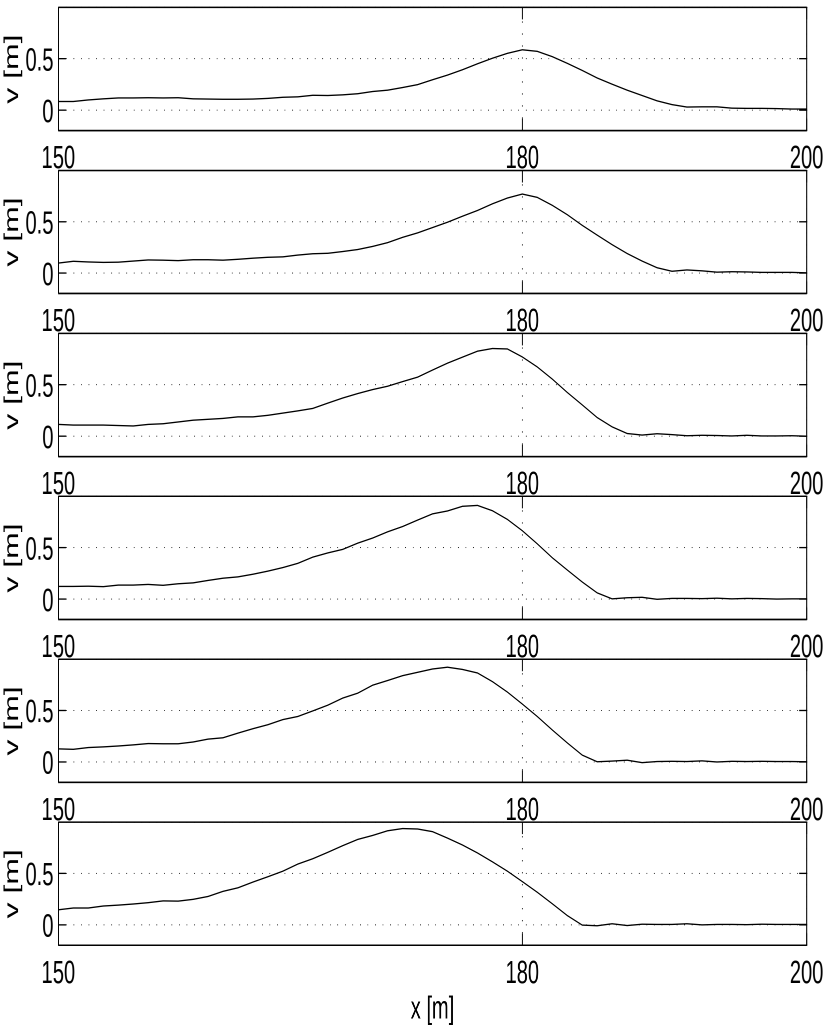

Figure 4.50: Deflection of the contact cable relative to its static equilibrium configuration, when excited by a constant, moving force with the speed 1) 400 *km/h*, 2) 410 *km/h*, 3) 420 *km/h*, 4) 430 *km/h*, 5) 440 *km/h*, and 6) 450 *km/h*. Note the smooth breaking sound barrier like phenomenon as a contrary to the case with linear cable models.

4.7.5 Filtering

In this section we shall treat the subject of filtering of output signals. The background for the investigations comes from our considerations on choice of spatial discretisation method, as we gave an account on in chapter 2. We know of other researchers who use a finite difference method for the spatial discretisation, and due to computer power reasons find it impracticable to use a sufficiently fine spatial discretisation to get converged output. Instead they use *some* spatial discretisation, and filter the output results to get rid of the large, numerical oscillations. As we mentioned in chapter 2 we feel very inconvenient with this approach.

We shall now illustrate the problem for the pantograph overhead line system with *our* choice of spatial discretisation, and show that great care should be taken when filtering an output signal.

Our method of filtering is rather primitive: We use the fast fourier transform (fft) device of MATLAB, [33], to transform the signal to the frequency domain. We choose a cut-off frequency and discard all the contribution to the signal which is content above this frequency. (Actually, due to the symmetry properties of a fast fourier transformation, we only discard the part of the signal given by the frequency range $f_{\text{cut-off}} \leq f \leq (f_{\max} - f_{\text{cut-off}})$, where $f_{\max}$ is the maximal frequency given by 1 over the time step size in the time series.)

In figure 4.51 we show the contact force signals over two spans, for a train speed of $speed = 220\ km/h$, and with 3 different spatial discretisation step sizes, $\Delta x = 2\ m$, $\Delta x = 1\ m$, and $\Delta x = 0.5\ m$.

It is seen that the contact force signals get lower amplitudes and become more high frequent as the discretisation step size decreases. In figure 4.52 we blow up the part of the signal given by $360 \leq x \leq 384$ for better being able to see the effect.

We must conjecture that the contact force signal given by the smallest spatial discretisation is 'closest' to being the true one.

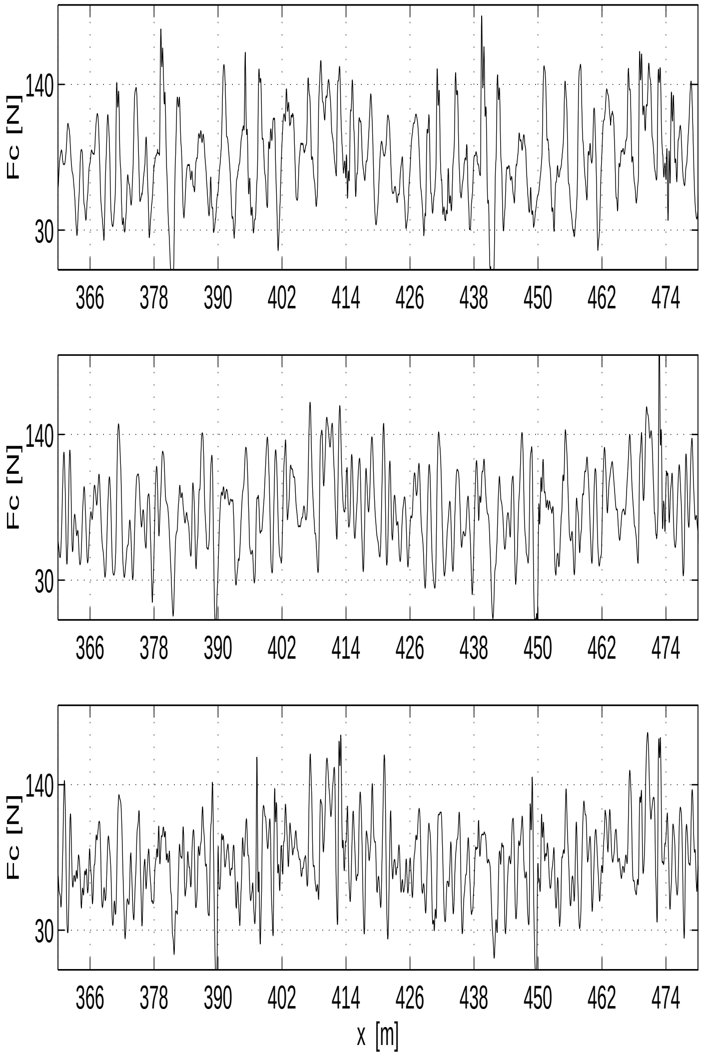

Figure 4.51: Contact force signals over 2 spans, for a train speed of $speed = 220\ km/h$, and spatial discretisation lengths of the cables of 1) $\Delta x = 2\ m$, $\Delta x = 1\ m$, and $\Delta x = 0.5\ m$.

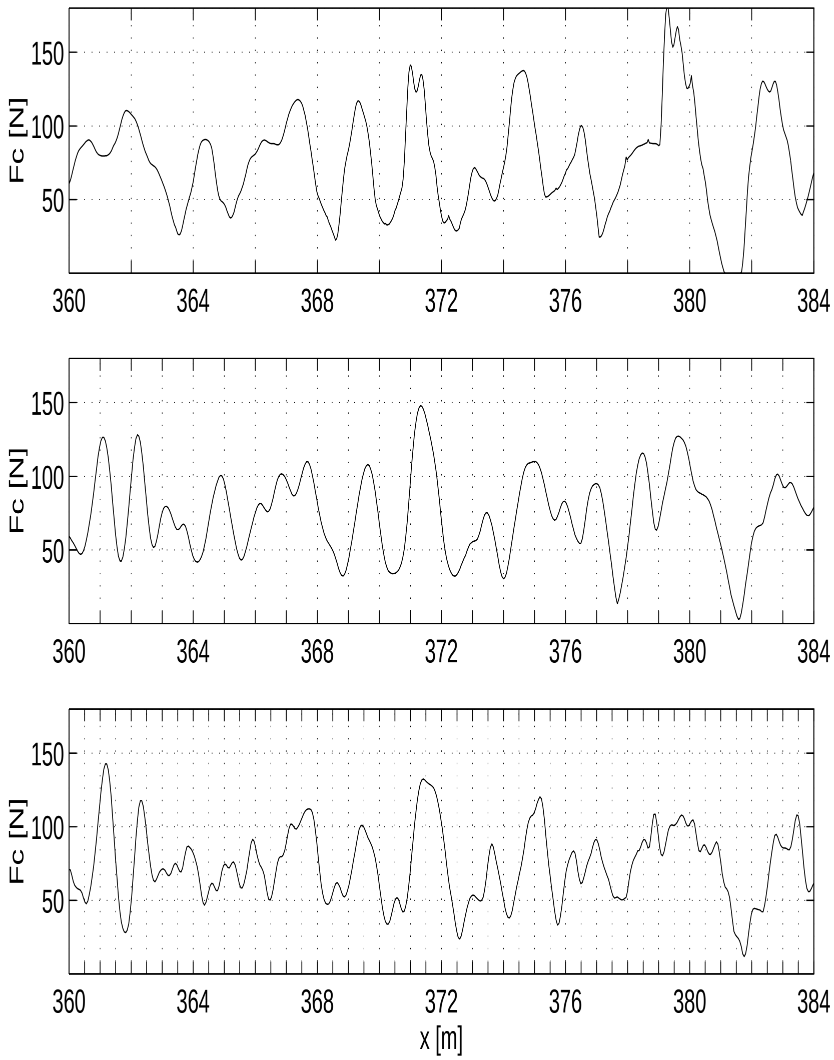

Figure 4.52: Blow up of figure 4.51.

In figure 4.53 we have filtered all the output signals with cut-off frequencies corresponding to the spatial step sizes; i.e. since $speed = 220/3.6 \approx 61.1\ m/s$, the output signals are filtered with cut-off frequencies 30.5 Hz, 61.1 Hz, and 122.2 Hz. Comparison with figure 4.52 yields that only very little of the signals are contained at frequencies corresponding to the spatial discretisation and above.

In figure 4.54 we compare the unfiltered signals (full lines), with the signals filtered with cut-off frequencies corresponding to twice the spatial step sizes (stabled lines), for the two contact force signals given by the spatial step sizes $\Delta x = 2\ m$ and $\Delta x = 0.5\ m$. I.e. the cut off frequencies are given by 15.2 Hz in the upper graph and 61.1 Hz in the bottom graph. We note that in the upper graph, the filtered and the unfiltered signals are very different, whereas the filtered and the unfiltered signals in the bottom graph are not very different. For the upper graph we must ask ourselves, *what* is being filtered away; numerical oscillations or physical oscillations? The upper graph suggests that the given spatial step size is too large to obtain sufficient convergence of the contact force signal. However, the *bottom* graph shows that a filtration of the output signal corresponding to *twice* the spatial step size,

$$f_{\text{cut-off}} = \frac{61.1\ m/s}{2 \cdot 0.5m} = 61.1\ Hz,$$

yields a filtered output signal very close to the unfiltered signal. This suggests that the oscillations in the output signal in the bottom graphs in figures 4.51, 4.52, 4.53, and 4.54 are *physical*, modelled oscillations rather than numerical oscillations.

Thus, one should be very careful when filtering an output signal. It may be relevant, but we think that the unfiltered output signals should also be studied, to be sure that the filtration does not destroy important informations about the physical system. We hope it is clear why we find it so important to chose a spatial discretisation method with fast convergence for these kind of systems, as we reflected on in chapter 2.

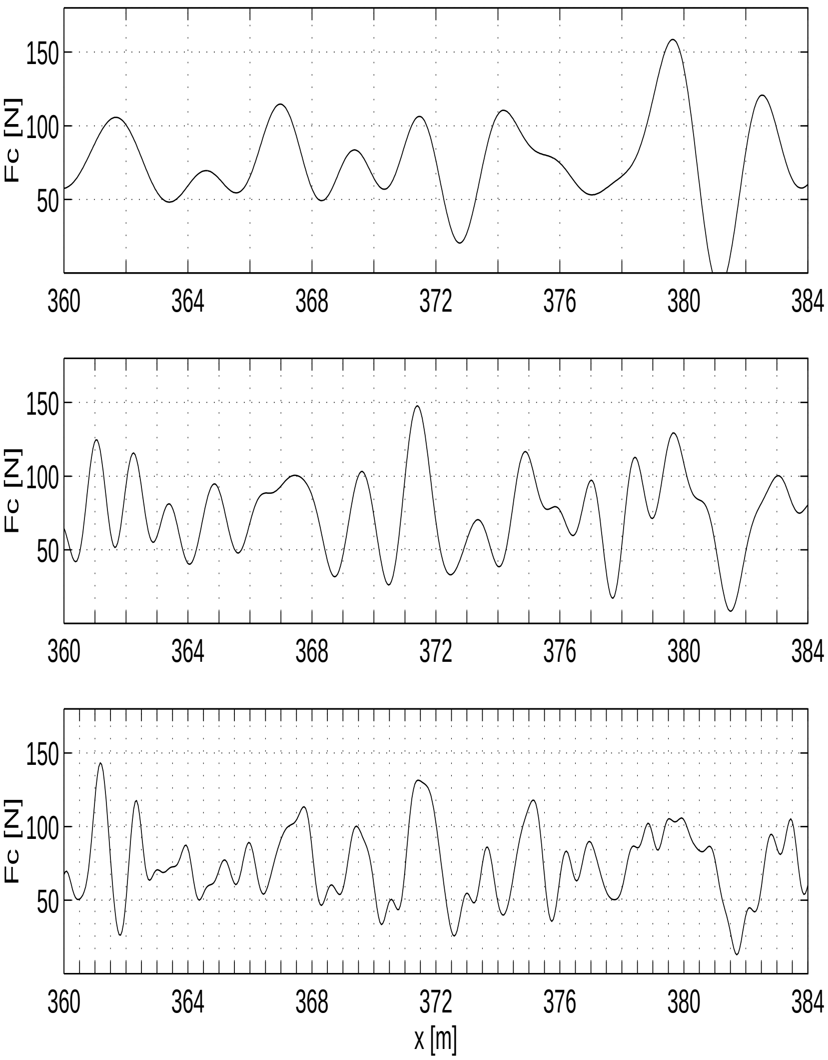

Figure 4.53: Filtered contact force signals corresponding to figure 4.52. The cut-off frequencies are 30.5 Hz in the upper graph, 61.1 Hz in the middle graph, and 122.2 Hz in the bottom graph, corresponding to the speed divided by the spatial discretisation step sizes.

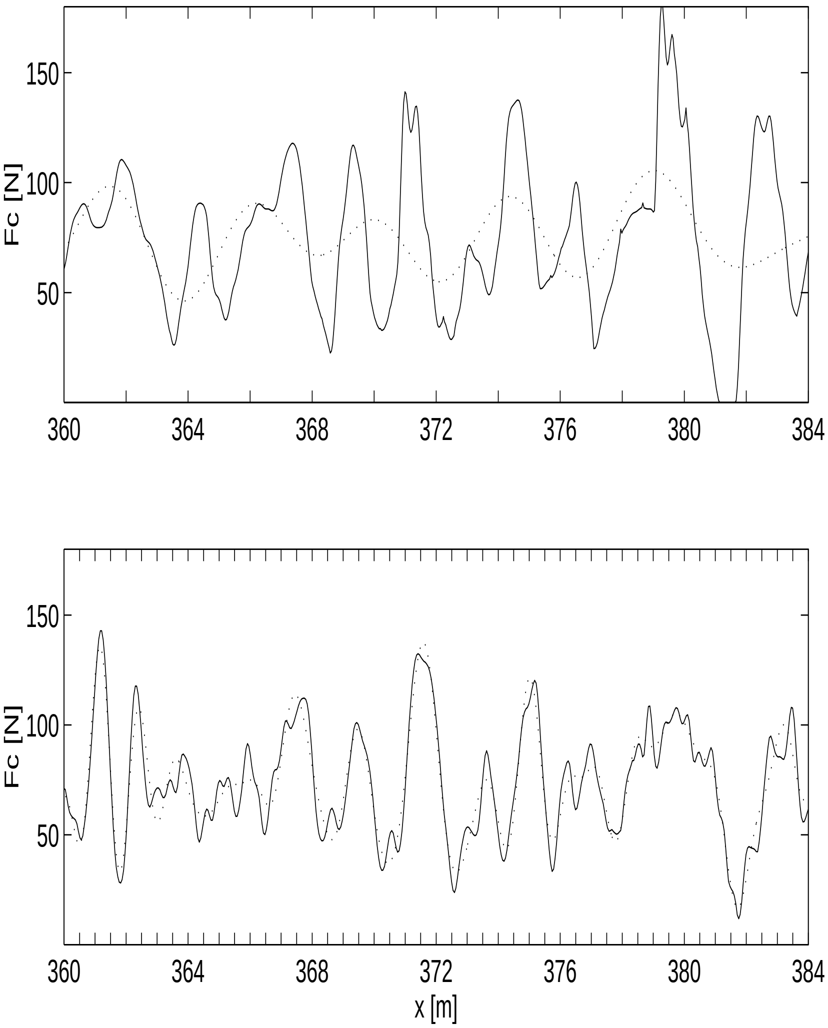

Figure 4.54: Comparison of unfiltered contact force signals (full lines) with contact force signals filtered with cut-off frequencies corresponding to twice the spatial discretisation step sizes. In the upper $f_{\text{cut-off}} = 15.2\ Hz$; in the bottom graph $f_{\text{cut-off}} = 61.1\ Hz$.

We illustrate the dangers of filtration with one of our results from a previous section. In figure 4.43 we showed the contact force signals, for a pantograph travelling with $speed = 190\ km/h$ under overhead line systems with no presag, a 2 cm presag, a 4 cm presag, and a 6 cm presag. We found the 6 cm presag configuration (which is the one corresponding to the danish overhead line systems) to have inferior performance to the other ones. In figure 4.55 we show this signal again in the upper graph, whereas the mid graph shows the contact force signal filtered with a cut-off frequency corresponding to the spatial discretisation step size, $f_{\text{cut-off}} = 52\ Hz$, and the bottom graph shows the contact force signal filtered with a cut-off frequency of $f_{\text{cut-off}} = 26\ Hz$. It is seen that any information about the 6 cm presag configuration having a problem at the end of each span is lost by the filtration.

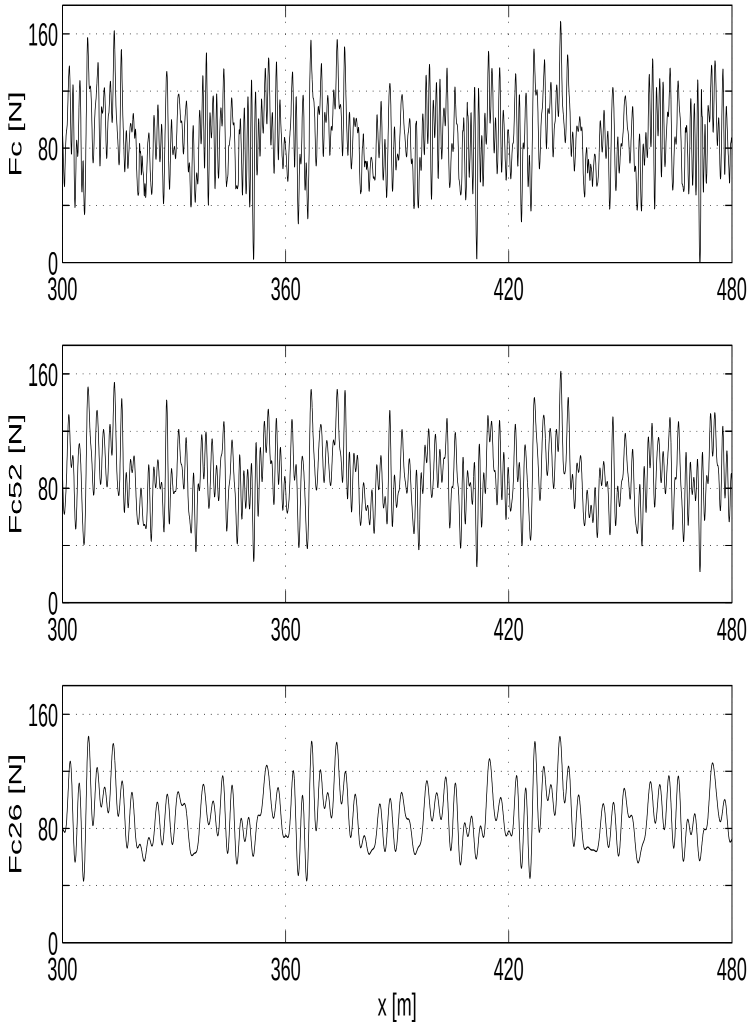

Figure 4.55: Upper graph: The unfiltered contact force signal of a pantograph travelling with *speed* = 190 *km*/*h* under an overhead line system with a 6 *cm* presag. Middle graph: The contact force signal filtered with $f_{\text{cut-off}} = 52\ Hz$. Bottom graph. The contact force signal filtered with $f_{\text{cut-off}} = 26\ Hz$.

Chapter 5

Conclusion

Let us conclude the thesis.

In chapter 2 we discussed in a general sense how to handle 'nonlinear systems with discrete and continuous elements'. Our discussion was based on our own experiences, mainly from the part of the ph.d. project about pantograph overhead line system interactions. With a simple example of the considered type of system, we illustrated some of the problems connected to the coupling of continuous and discrete subsystems. We found that performing the spatial discretisation with a finite element method with cubic basis functions is best suited, because it gives faster convergence in the coupling process of the two subsystems than other methods. We also mentioned the modal approach as a very strong alternative, if the continuous system can be described by linear equations, or if it is very rigid, not too complex, and/or only the first few modes are excited.

In chapter 3 we considered train bridge interactions. We found that this system is exactly of the type that can advantageously be handled with a modal approach. Our train bridge investigation differed from earlier investigations by the relatively complex train models, which included a description of some important nonlinearities. The background for these nonlinearities was described shortly. A few results were referred to. The most important conclusion of our train bridge investigations was that a very simple train model could be adopted with very good accuracy in investigations only considering vertical motion of the bridge.

The most important system we have analysed is that of pantograph overhead line system interactions in chapter 4. We first reflected on the traditional approaches for modelling the cables in such systems. We derived a set of partial differential equations for the cable motions that includes both a description of the bending stiffness and of the weak nonlinearities of the cables in such systems. We then divided our analysis into a part concerning investigations of the propagation of a pulse on single cable models, and the direct investigations of pantograph overhead line system interactions.

We found that none of the ‘small terms’ in the cable equations had much significance for the development of the propagating pulse, for the considered pulse and cable dimensions. The individual nonlinear terms were much larger in magnitude than the bending term, but their *sum* almost balanced. In fact we found that the longitudinal motion could be satisfactorily described by a slow, local part and a fast, global part, yielding the sum of the nonlinear terms as $(K + K_1(t))v_{xx}$, where $v(x,t)$ is the vertical motion of the cable.

In the direct pantograph overhead line system investigations, we found that the nonlinearities, as a contrary to the bending stiffness, did become important within the range of realistic train speeds. We found them to have a positive effect on the dynamics. We concluded that the nonlinearities should be included in the cable models. This means that, due to the characteristic time scale of the longitudinal motion, the cables in the overhead line systems will have to be modelled in their full lengths. This puts limitations on the spatial discretisation step size due to computer power reasons — which means that a spatial discretisation method with fast convergence must be chosen, as considered in chapter 2. Actually, our results indicate that an even faster converging method should be developed in the future; we suggest a finite element method with higher order basis functions than the piecewise cubic ones we have adopted.

For our investigations near the *critical* speed, we found that it was strictly necessary to include the nonlinearities in the model, to be able to satisfactorily describe the breaking sound barrier like phenomenon, that appears for pantographs accelerating up to and past the critical speed. We found that the breaking sound barrier like phenomenon is much smoother when the nonlinearities of the system are included. This is important because the critical speed thereby is not as *critical* as henceforth assumed.

We have also investigated the influence of a presag of the contact cable in overhead line systems with simple configurations. The presag is meant to compensate for the variation of the flexibility of the contact cable over a span. However, we think that the presag has been designed from purely statical considerations, and from our dynamical investigations we find that the presag should either not be there, or should be much smaller.

Finally we have considered the effect of filtering output signals. In this respect we are rather restricted in our conclusions, since we have not had access to measurements for comparisons with our numerical predictions. Filtering might be relevant! However, filtering should be used with caution and can by no means substitute the use of a sufficiently fine discretisation grid.

Bibliography

[1] ALGOR, INC. *Linear Mode Shape Analysis, Release Notes*, August 1995.

[2] V.A. Barker and O. Tingleff. *Numerisk løsning af ikke-linære ligninger*. Department of Mathematical Modelling, The Technical University of Denmark, 1991. In danish.

[3] S. Bartels. Versuchsstromabnehmer für ICE. *Elektrische Bahnen*, 9:290–296, 1988.

[4] K. Becker, A. König, U. Resch, and B.W. Zweig. Systematic development of a high-speed overhead contact line. *Railway Technical Review*, 3:47–55, 1995.

[5] F. Brancaleoni, F. Cheli, and G. Diana. Railway traffic on long suspension bridges. In *13th IABSE Congress, Helsinki*, pages 883–888, June 6-10 1988.

[6] A. Collina. Politecnico di Milano, Italy. personal correspondence.

[7] M. Cook. Pantograph/overhead dynamics calculations. Technical report, ORE Commitee A186, June 1991. Vehicle Dynamics Unit.

[8] G. Diana and F. Cheli. A numerical method to define the dynamic behaviour of a train running on a deformable structure. *Meccanica*, 23:27–42, 1988.

[9] G. Diana and F. Cheli. Dynamic interaction of railway systems with large bridges. *Vehicle System Dynamics*, 18:71–106, 1989.

[10] G. Diana, F. Cheli, S. Bruni, and A. Collina. Interaction be-

tween railroad superstructure and railway vehicles. In *Proceedings of 13th IAVSD Congress in Chengdu, China*, August 23-27 1993.

[11] G. Diana, F. Cheli, S. Bruni, and A. Collina. Super long suspension bridges: Railway runnability. In *15th IABSE Congress in Copenhagen*, June 16-20 1996.

[12] G. Diana, B. Pizzigoni, and F. Cheli. Dynamic interaction of railway system with large bridge. *VDI Berichte*, 635:293–325, 1987.

[13] S.D. Eppinger, D.N. O'Connor, W.P. Seering, and D.N. Wormley. Modelling and experimental evaluation of asymmetric pantograph dynamics. *Transactions of the ASME Journal of Dynamic Systems, Measurement, and Control*, 110:168–174, 1988.

[14] V. Eriksen and J. Outtrup. ScanRail Consult. personal correspondence.

[15] ES-Consult. Bridges: Wheel load relief during passage of an expansion joint. Internal report, September 1994.

[16] ES-Consult. Atr 95-5: Train passenger comfort on the øresund link, coast to coast. Internal report, Februar 1996.

[17] R.D. Fröhling. Measurement, interpretation and classification of south african track geometry. *Vehicle System Dynamics Supplement*, 24:133–145, 1995.

[18] G. Galeotti, M. Galanti, and S. Magrini. Servo acutated railway pantograph for high-speed running with constant contact force. *Journal of Rail and Rapid Transit*, Part F:37–49, 1993.

[19] H. Goldstein. *Classical Mechanics*. Addison-Wesley publishing Company, 1980.

[20] R.J. Gostling and A.E.W. Hobbs. The interaction of pantograph and overhead equipment: practical applications of a new theoretical method. In *Proceedings of the Institution of Mechanical Engineers*, volume 197, 1983.

[21] E. Hansen. *Variationsregning*. Polyteknisk forlag, Lyngy, 1976. In danish.

[22] W. Harprecth, F. Kiessling, and R. Seifert. 406.9 km/h - world

record on rails - power transmission in the record run of db's ice. *Translation of article from Elektrische Bahnen*, 86:1–23, 9 1988.

[23] W. Herbert. Entwicklung und betriebserfahrung mit dem hochgeschwindigkeits-stromabnehmer dsa 350 s für den ICE. *ETR*, 41:385–390, 1992.

[24] H. Hertz. Über die beruehrung fester elastischer körper. *Journal für die reine und angewandte Mathematik*, 92:156–171, 1882.

[25] A.E.W. Hobbs. Accurate prediction of overhead line behaviour. *Railway Gazette*, september:339–343, 1988.

[26] C.N. Jensen and H. True. Dynamics of an electrical overhead line system and moving pantographs. In *Proceedings of 15. IAVSD Symposium*, 1997.

[27] C.N. Jensen and H. True. On a new route to chaos in railway dynamics. *Nonlinear Dynamics*, 13:117–129, 1997.

[28] J. C. Jensen. *Teoretiske og Eksperimentelle Dynamiske Undersøgelser af Jernbanekøretøjer.* PhD thesis, The Technical University of Denmark, 1995. In danish.

[29] J.J. Kalker. *Three-dimensional elastic bodies in rolling contact.* Kluwer, 1990.

[30] F. Kiessling, M. Semrau, H. Tessun, and B.W. Zweig. Neue hochleistungsoberleitung bauart re 330 der deutschen bahn. *Elektrische Bahnen*, 92:234–240, 1994.

[31] T. Larsson and T. Söderberg. Strömavtagare till x2-tåg. Master's thesis, The Technical University in Luleå, 1996:164E. in swedish.

[32] M. Lesser, L. Karlsson, and L. Drugge. An interactive model of a pantograph-catenary system. *Vehicle System Dynamics Supplement*, 25:397–412, 1996.

[33] The Math Works Inc. *MATLAB: User's Guide and Reference Guide*, 1992.

[34] A.H. Nayfeh. *Nonlinear Oscillations.* John Wiley & Sons, 1979.

[35] K. Petri and J. Wallaschek. Modelling the dynamic behaviour of catenary-pantograph systems for high speed trains. In *Pro-*

ceedings of International Symposium on Cable Dynamics, 1995.

[36] G. Poetsch, J. Evans, R. Meisinger, W. Kortüm, W. Baldauf, A. Veitl, and J. Wallaschek. Pantograph/catenary dynamics and control. *Vehicle System Dynamics*, 28:159–195, 1997.

[37] G. Poetsch and J. Wallaschek. Simulating the dynamic behaviour of electrical lines for high-speed trains on parallel computers. In *Proceedings of International Symposium on Cable Dynamics*, 1995.

[38] P.R. Scott and M. Rothman. Computer evaluation of overhead equipment for electric railroad traction. *IEEE Transactions on industry applications*, 1A-10:573–579, 1974.

[39] Z.Y. Shen, J.K. Hedrick, and J.A. Elkins. A comparison of alternative creepforce models for rail vehicle dynamical analysis. In *Proceedings of 8. IAVSD Symposium*, 1983.

[40] A. Simpson, A. Beadr, and J. Young. Design evolution of the Tsing Ma bridge. In *IABSE Symposium, Vol. 64*, 1991.

[41] E.C. Slivsgaard. *On the Interaction between Wheels and Rails in Railway Dynamics.* PhD thesis, The Technical University of Denmark, 1995.

[42] V. Tvergaard, P.T. Pedersen, and F. Niordson. *Svingningslære.* The Department of solid mechanics, The Technical University of Denmark, 1980. In danish.

[43] UMTRI, The University of Michigan Transportation Research Institute. *Introductory guide to AUTOSIM*, 1992.

[44] G.B. Whitham. *Linear and Nonlinear Waves.* John Wiley & Sons, 1974.

[45] S. Wolfram. *MATHEMATICA: A system for Doing Mathematics by Computer.* Addison-Wesley Publishing Company, Inc., 1988.

[46] W.M. Zhai and C.B. Cai. Effect of locomotive vibrations on pantograph-catenary system dynamics. In *Proceedings of 15. IAVSD Symposium*, 1997.

Appendix A

Nonlinear dispersion relation

We now want to use a variational approach to achieve a nonlinear dispersion relation following the technique in [44]. We first illustrate the method on the Bernoulli Euler beam equation (which of course is linear):

$$\mu v_{tt} = P_0 v_{xx} - EI v_{xxxx} \tag{A.1}$$

It is not a surprise that the dispersion relation for this equation is

$$\mu\omega^2 - P_0 k^2 - EIk^4 = 0 \tag{A.2}$$

found simply by substituting $v \sim e^{ikx - i\omega t}$ in (A.1).

We will derive this result using a variational approach. We study slowly varying wavetrains

$$v \sim a(x,t)\cos(\theta(x,t) + \eta(x,t)). \tag{A.3}$$

Because a and η are assumed to be slowly varying, these can be considered as constants when integrating over a period in θ (averaging). Further, we can approximate

$$v_t \sim a_t(x,t)\cos(\theta(x,t)+\eta(x,t)) - a(x,t)\theta_t(x,t)\sin(\theta(x,t)+\eta(x,t)) -$$

$$
\begin{aligned}
&a(x,t)\eta_t(x,t)\sin(\theta(x,t)+\eta(x,t)) \simeq \\
&-a(x,t)\theta_t(x,t)\sin(\theta(x,t)+\eta(x,t))
\end{aligned}
$$

$$
\begin{aligned}
v_x \sim a_x(x,t)\cos(\theta(x,t)+\eta(x,t)) - a(x,t)\theta_x(x,t)\sin(\theta(x,t)+\eta(x,t)) - \\
a(x,t)\eta_x(x,t)\sin(\theta(x,t)+\eta(x,t)) \simeq \\
-a(x,t)\theta_x(x,t)\sin(\theta(x,t)+\eta(x,t)),
\end{aligned}
$$

thus, terms involving a_t, a_x, η_t or η_x are neglected.
$\theta(x,t)$ is called the phase, and we finally define the local wave number and frequency by

$$k = \theta_x \qquad \textit{and} \qquad \omega = -\theta_t. \tag{A.4}$$

To use a variational approach we need the Lagrangian for the system. This is

$$L = \frac{1}{2}\left(\mu v_t^2 - P_0 v_x^2 - EI v_{xx}^2\right). \tag{A.5}$$

(Note: (A.1) is refound by computing $-\frac{\partial}{\partial t}L_{v_t} - \frac{\partial}{\partial x}L_{v_x} + -\frac{\partial^2}{\partial x^2}L_{v_{xx}}$.)

We now substitute (A.3) in (A.5), neglect all derivatives of a, η, ω, and k, and average over one period in θ to achieve the function

$$\mathcal{L} = \frac{1}{4}\left(\mu\omega^2 - P_0 k^2 - EIk^4\right)a^2. \tag{A.6}$$

We propose the 'average variational principle'

$$\delta \int\int \mathcal{L}(\omega, k, a)\,dt\,dx = 0 \tag{A.7}$$

for the functions $a(x,t)$ and $\theta(x,t)$.
The variational equation for variations in a becomes

$$\delta a : \quad \mathcal{L}_a = 0. \tag{A.8}$$

The variational equation for θ is

$$\delta\theta : \quad -\frac{\partial}{\partial t}\mathcal{L}_{\theta_t} - \frac{\partial}{\partial x}\mathcal{L}_{\theta_x} = \frac{\partial}{\partial t}\mathcal{L}_\omega - \frac{\partial}{\partial x}\mathcal{L}_k = 0. \tag{A.9}$$

At last, from (A.4) we have the consistency relation for θ

$$\frac{\partial k}{\partial t}+\frac{\partial \omega}{\partial x}=0. \tag{A.10}$$

Substituting (A.6) in (A.8) yields

$$\frac{1}{2}\left(\mu\omega^2-P_0k^2-EIk^4\right)a=0 \iff \mu\omega^2-P_0k^2-EIk^4 \iff$$

$$\omega=\pm\sqrt{\frac{P_0}{\mu}k^2+\frac{EI}{\mu}k^4} \tag{A.11}$$

which we recognize as the dispersion relation for the Bernoulli Euler beam equation. We calculate the linear group velocity as

$$C_g=\frac{\partial\omega}{\partial k}=\pm\frac{\frac{P_0}{\mu}k+2\frac{EI}{\mu}k^3}{\sqrt{\frac{P_0}{\mu}k^2+\frac{EI}{\mu}k^4}}=\frac{P_0k+2EIk^3}{\mu\omega}. \tag{A.12}$$

Substituting (A.6) in (A.9), taking advantage of (A.10) and (A.12) yields

$$\frac{\partial}{\partial t}\mathcal{L}_\omega-\frac{\partial}{\partial x}\mathcal{L}_k=0 \quad \Leftrightarrow$$

$$\frac{\partial}{\partial t}\left(\frac{1}{2}\mu\omega a^2\right)-\frac{\partial}{\partial x}\left(-\frac{1}{2}P_0ka^2-EIk^3a^2\right)=$$

$$\frac{\partial}{\partial t}\left(\frac{1}{2}\mu\omega a^2\right)+\frac{\partial}{\partial x}\left(\frac{1}{2}\mu\omega\frac{P_0k+2EIk^3}{\mu\omega}a^2\right)=$$

$$\frac{\partial}{\partial t}\left(\frac{1}{2}\mu\omega a^2\right)+\frac{\partial}{\partial x}\left(\frac{1}{2}\mu\omega C_ga^2\right)=$$

$$\frac{1}{2}\mu\omega\left(\frac{\partial a^2}{\partial t}+\frac{\partial}{\partial x}\left(C_ga^2\right)\right)+\frac{1}{2}\mu a^2\frac{\partial\omega}{\partial t}+\frac{1}{2}\mu a^2C_g\frac{\partial\omega}{\partial x}=$$

$$\frac{1}{2}\mu\omega\left(\frac{\partial a^2}{\partial t}+\frac{\partial}{\partial x}\left(C_ga^2\right)\right)+\frac{1}{2}\mu a^2C_g\left(\frac{\partial k}{\partial t}+\frac{\partial\omega}{\partial x}\right)=$$

$$\frac{1}{2}\mu\omega\left(\frac{\partial a^2}{\partial t}+\frac{\partial}{\partial x}\left(C_g a^2\right)\right)=0 \Leftrightarrow$$

$$\frac{\partial a^2}{\partial t}+\frac{\partial}{\partial x}\left(C_g a^2\right)=0 \tag{A.13}$$

which is an equation for the amplitude.

Haven developed the technique we will now derive a dispersion relation for the cable equation (4.8). The equation is repeated here:

$$\mu v_{tt}=P_0 v_{xx}-EIv_{xxxx}+\frac{3}{2}v_x^2 v_{xx}, \tag{A.14}$$

thus, the Lagrangian is

$$L=\frac{1}{2}\left(\mu v_t^2-P_0 v_x^2-EIv_{xx}^2-\frac{1}{4}EAv_x^4\right). \tag{A.15}$$

We search for a slowly varying wavetrain solution. In our case it will suffice to apply a near-linearity-technique; thus, we assume

$$v(x,t)=v(\theta)=a\cos(\theta)+a_2\cos(2\theta)+a_3\cos(3\theta)+a_4\cos(4\theta)+\ldots \tag{A.16}$$

where θ still has the property given by (A.10), and where we assume $a_2=\mathcal{O}(a^2), a_3=\mathcal{O}(a^3), a_4=\mathcal{O}(a^4)$ and so on. We then substitute (A.16) in (A.15) and average over one period in θ; this is done keeping ω, k, a_i constant:

$$\overline{L}=\frac{1}{2\pi}\int_0^{2\pi}L(v_t,v_x,v_{xx})d\theta=$$

$$\frac{1}{2\pi}\int_0^{2\pi}\left(\frac{1}{2}(\mu\omega^2-P_0k^2)v_\theta^2-\frac{1}{2}EIk^4v_{\theta\theta}^2-\frac{1}{8}EAk^4v_\theta^4\right)d\theta=$$

$$\begin{gathered}\frac{1}{4}\left(\mu\omega^2 - P_0k^2 - EIk^4\right)a^2 + \\ \left(\left(\mu\omega^2 - P_0k^2 - 4EIk^4\right)a_2^2 - \frac{3}{64}EAk^4a^4\right) + \\ \left(\frac{9}{4}\left(\mu\omega^2 - P_0k^2 - 9EIk^4\right)a_3^2 - \frac{3}{4}EAk^4a_2^2a^2 + \frac{3}{16}a_3a^3\right) + \mathcal{O}(a^8).\end{gathered} \tag{A.17}$$

Defining then

$$\begin{gathered}\mathcal{L} = \frac{1}{4}\left(\mu\omega^2 - P_0k^2 - EIk^4\right)a^2 + \\ \left(\left(\mu\omega^2 - P_0k^2 - 4EIk^4\right)a_2^2 - \frac{3}{64}EAk^4a^4\right)\end{gathered} \tag{A.18}$$

we have

$$\overline{L} = \mathcal{L} + \mathcal{O}(a^6).$$

We propose the variational principle

$$\delta\int\!\!\int \mathcal{L}(\omega, k, a, a_2)\,dx\,dt = 0. \tag{A.19}$$

Variation with respect to a_2 shows that $a_2 = 0$. Thus

$$\mathcal{L} = \frac{1}{4}\left(\mu\omega^2 - P_0k^2 - EIk^4 - \frac{3}{16}EAk^4a^2\right)a^2. \tag{A.20}$$

Substituting (A.20) in (A.8) yields

$$\begin{gathered}\delta a : \ \frac{1}{2}\left(\mu\omega^2 - P_0k^2 - EIk^4 - \frac{3}{8}EAk^4a^2\right)a = 0 \Leftrightarrow \\ \mu\omega^2 - P_0k^2 - EIk^4 - \frac{3}{8}EAk^4a^2 = 0.\end{gathered} \tag{A.21}$$

This is the *nonlinear dispersion relation*!

We also find the nonlinear group velocity

$$C_g^n = \frac{\partial\omega}{\partial k} = \frac{P_0k + 2EIk^3 + \frac{3}{4}EAk^3a^2}{\mu\omega}. \tag{A.22}$$

Substituting (A.20) in (A.9) and taking advantage of (A.10) and (A.22) yields the amplitude equation:

$$\frac{\partial}{\partial t}\left(\frac{1}{2}\mu\omega a^2\right) - \frac{\partial}{\partial x}\left(-\frac{1}{2}P_0 k a^2 - EIk^3a^2 - \frac{3}{16}EAk^3a^4\right) =$$

$$\frac{\partial}{\partial t}\left(\frac{1}{2}\mu\omega a^2\right) + \frac{\partial}{\partial x}\left(\frac{1}{2}\mu\omega\frac{P_0k + 2EIk^3 + \frac{3}{4}EAk^3a^2 - \frac{3}{8}EAk^3a^2}{\mu\omega}a^2\right) =$$

$$\frac{\partial}{\partial t}\left(\frac{1}{2}\mu\omega a^2\right) + \frac{\partial}{\partial x}\left(\frac{1}{2}\mu\omega C_g^n a^2\right) - \frac{\partial}{\partial x}\left(\frac{3}{16}EAk^3a^4\right) =$$

$$\frac{1}{2}\mu\omega\left(\frac{\partial a^2}{\partial t} + \frac{\partial}{\partial x}\left(C_g^n a^2\right)\right) +$$

$$\frac{1}{2}\mu a^2\frac{\partial\omega}{\partial t} + \frac{1}{2}\mu C_g^n a^2\frac{\partial\omega}{\partial x} - \frac{\partial}{\partial x}\left(\frac{3}{16}EAk^3a^4\right) =$$

$$\frac{1}{2}\mu\omega\left(\frac{\partial a^2}{\partial t} + \frac{\partial}{\partial x}\left(C_g^n a^2\right)\right) +$$

$$\frac{1}{2}\mu C_g^n a^2\left(\frac{\partial k}{\partial t} + \frac{\partial\omega}{\partial x}\right) - \frac{\partial}{\partial x}\left(\frac{3}{16}EAk^3a^4\right) =$$

$$\frac{1}{2}\mu\omega\left(\frac{\partial a^2}{\partial t} + \frac{\partial}{\partial x}\left(C_g^n a^2\right)\right) - \frac{\partial}{\partial x}\left(\frac{3}{16}EAk^3a^4\right) = 0 \qquad \text{(A.23)}$$

Note that the important new feature *not* is the correction of the amplitude equation but *the dependence of the amplitude in the dispersion relation*, (A.21).

Appendix B

Finite element integrations

In this appendix we shall calculate the integration coefficients from the finite element discretisation of the contact cable. Similar calculations go for the catenary cable and the results for these integrations are found by interchanging variables. The integrations have been performed with the commercial software for performing symbolic mathematics on computers, MATHEMATICA, [45].

We shall calculate the coefficients term by term and we shall indicate the combination of variables that belong to the coefficients. The titles of the sections refer to subroutine names from the numerical implementation.

B.1 phi

With $W1 = \phi_j$ the first term in (4.52) becomes:

$$\begin{aligned}
&\int_0^L \sum_{i=0}^{nco} \Big((\mu \ddot{b}_i + \eta_1 \dot{b}_i)\phi_i + (\mu \ddot{c}_i + \eta_1 \dot{c}_i)\psi_i \Big)\, \phi_j \, dx = \\
&(\mu \ddot{b}_{j-1} + \eta_1 \dot{b}_{j-1}) \textstyle\int_{x_{j-1}}^{x_j} \phi_{j-1}\phi_j \, dx + (\mu \ddot{b}_j + \eta_1 \dot{b}_j) \textstyle\int_{x_{j-1}}^{x_{j+1}} \phi_j \phi_j \, dx + \\
&(\mu \ddot{b}_{j+1} + \eta_1 \dot{b}_{j+1}) \textstyle\int_{x_j}^{x_{j+1}} \phi_{j+1}\phi_j \, dx + \\
&(\mu \ddot{c}_{j-1} + \eta_1 \dot{c}_{j-1}) \textstyle\int_{x_{j-1}}^{x_j} \psi_{j-1}\phi_j \, dx + (\mu \ddot{c}_j + \eta_1 \dot{c}_j) \textstyle\int_{x_{j-1}}^{x_{j+1}} \psi_j \phi_j \, dx + \\
&(\mu \ddot{c}_{j+1} + \eta_1 \dot{c}_{j+1}) \textstyle\int_{x_j}^{x_{j+1}} \psi_{j+1}\phi_j \, dx.
\end{aligned}$$

We therefore calculate the following coefficients and indicate the variables to which they maid.

1	: $\ddot{b}_{j-1}, \dot{b}_{j-1}$	: $\int_{x_{j-1}}^{x_j} \phi_{j-1}\phi_j dx$	$= \frac{9\, h_{j-1}}{70}$
2a	: $\ddot{b}_j, \dot{b}_j$	: $\int_{x_{j-1}}^{x_j} \phi_j \phi_j dx$	$= \frac{13\, h_{j-1}}{35}$
2b	: $\ddot{b}_j, \dot{b}_j$	: $\int_{x_j}^{x_{j+1}} \phi_j \phi_j dx$	$= \frac{13\, h_j}{35}$
3	: $\ddot{b}_{j+1}, \dot{b}_{j+1}$	: $\int_{x_j}^{x_{j+1}} \phi_{j+1}\phi_j dx$	$= \frac{9\, h_j}{70}$
4	: $\ddot{c}_{j-1}, \dot{c}_{j-1}$	: $\int_{x_{j-1}}^{x_j} \psi_{j-1}\phi_j dx$	$= \frac{13\, {h_{j-1}}^2}{420}$
5a	: $\ddot{c}_j, \dot{c}_j$	: $\int_{x_{j-1}}^{x_j} \psi_j \phi_j dx$	$= \frac{-11\, {h_{j-1}}^2}{210}$
5b	: $\ddot{c}_j, \dot{c}_j$	: $\int_{x_j}^{x_{j+1}} \psi_j \phi_j dx$	$= \frac{11\, {h_j}^2}{210}$
6	: $\ddot{c}_{j+1}, \dot{c}_{j+1}$	: $\int_{x_j}^{x_{j+1}} \psi_{j+1}\phi_j dx$	$= \frac{-13\, {h_j}^2}{420}$

B.2 ddphi

By substituting $W1 = \phi_j$ in (4.52) the second term becomes:

$$\begin{aligned}
&\int_0^L EI \sum_{i=0}^{nco} (b_i \phi_i'' + c_i \psi_i'')\, \phi_j'' \, dx = \\
&EI b_{j-1} \textstyle\int_{x_{j-1}}^{x_j} \phi_{j-1}'' \phi_j'' \, dx + EI b_j \textstyle\int_{x_{j-1}}^{x_{j+1}} \phi_j'' \phi_j'' \, dx + \\
&EI b_{j+1} \textstyle\int_{x_j}^{x_{j+1}} \phi_{j+1}'' \phi_j'' \, dx + EI c_{j-1} \textstyle\int_{x_{j-1}}^{x_j} \psi_{j-1}'' \phi_j'' \, dx + \\
&EI c_j \textstyle\int_{x_{j-1}}^{x_{j+1}} \psi_j'' \phi_j'' \, dx + EI c_{j+1} \textstyle\int_{x_j}^{x_{j+1}} \psi_{j+1}'' \phi_j'' \, dx,
\end{aligned}$$

why we calculate the following coefficients:

$$\begin{array}{llll}
1 & : b_{j-1} & : \int_{x_{j-1}}^{x_j} \phi''_{j-1}\phi''_j \, dx & = \frac{-12}{{h_{j-1}}^3} \\
2a & : b_j & : \int_{x_{j-1}}^{x_j} \phi''_j\phi''_j \, dx & = \frac{12}{{h_{j-1}}^3} \\
2b & : b_j & : \int_{x_j}^{x_{j+1}} \phi''_j\phi''_j \, dx & = \frac{12}{{h_j}^3} \\
3 & : b_{j+1} & : \int_{x_j}^{x_{j+1}} \phi''_{j+1}\phi''_j \, dx & = \frac{-12}{{h_j}^3} \\
4 & : c_{j-1} & : \int_{x_{j-1}}^{x_j} \psi''_{j-1}\phi''_j \, dx & = \frac{-6}{{h_{j-1}}^2} \\
5a & : c_j & : \int_{x_{j-1}}^{x_j} \psi''_j\phi''_j \, dx & = \frac{-6}{{h_{j-1}}^2} \\
5b & : c_j & : \int_{x_j}^{x_{j+1}} \psi''_j\phi''_j \, dx & = \frac{6}{{h_j}^2} \\
6 & : c_{j+1} & : \int_{x_j}^{x_{j+1}} \psi''_{j+1}\phi''_j \, dx & = \frac{6}{{h_j}^2}
\end{array}$$

B.3 dphi

By substituting $W1 = \phi_j$ in (4.52) the third term becomes:

$$\begin{array}{l}
\displaystyle\int_0^L P0 \sum_{i=0}^{nco} \left(b_i\phi'_i + c_i\psi'_i\right) \phi'_j \, dx = \\
P0b_{j-1} \int_{x_{j-1}}^{x_j} \phi'_{j-1}\phi'_j \, dx + P0b_j \int_{x_{j-1}}^{x_{j+1}} \phi'_j\phi'_j \, dx + \\
P0b_{j+1} \int_{x_j}^{x_{j+1}} \phi'_{j+1}\phi'_j \, dx + P0c_{j-1} \int_{x_{j-1}}^{x_j} \psi'_{j-1}\phi'_j \, dx + \\
P0c_j \int_{x_{j-1}}^{x_{j+1}} \psi'_j\phi'_j \, dx + P0c_{j+1} \int_{x_j}^{x_{j+1}} \psi'_{j+1}\phi'_j \, dx,
\end{array}$$

and we calculate

$$\begin{array}{llll}
1 & : b_{j-1} & : \int_{x_{j-1}}^{x_j} \phi'_{j-1}\phi'_j \, dx & = \frac{-6}{5\,h_{j-1}} \\
2a & : b_j & : \int_{x_{j-1}}^{x_j} \phi'_j\phi'_j \, dx & = \frac{6}{5\,h_{j-1}} \\
2b & : b_j & : \int_{x_j}^{x_{j+1}} \phi'_j\phi'_j \, dx & = \frac{6}{5\,h_j} \\
3 & : b_{j+1} & : \int_{x_j}^{x_{j+1}} \phi'_{j+1}\phi'_j \, dx & = \frac{-6}{5\,h_j} \\
4 & : c_{j-1} & : \int_{x_{j-1}}^{x_j} \psi'_{j-1}\phi'_j \, dx & = -\frac{1}{10} \\
5a & : c_j & : \int_{x_{j-1}}^{x_j} \psi'_j\phi'_j \, dx & = -\frac{1}{10} \\
5b & : c_j & : \int_{x_j}^{x_{j+1}} \psi'_j\phi'_j \, dx & = \frac{1}{10} \\
6 & : c_{j+1} & : \int_{x_j}^{x_{j+1}} \psi'_{j+1}\phi''_j \, dx & = \frac{1}{10}
\end{array}$$

B.4 dvuphi

By substituting $W1 = \phi_j$ in (4.52) the first nonlinear term becomes:

$$\int_0^L EA \sum_{i,k=0}^{nco} \left(b_i \phi_i' + c_i \psi_i'\right) \left(d_k \theta_k'\right) \phi_j' \, dx$$

why we calculate the coefficients

1	$: b_{j-1} d_{j-1}$	$: \int_{x_{j-1}}^{x_j} \phi_{j-1}' \theta_{j-1}' \phi_j' \, dx$	$= \frac{6}{5 \, h_{j-1}{}^2}$
2	$: b_{j-1} d_j$	$: \int_{x_{j-1}}^{x_j} \phi_{j-1}' \theta_j' \phi_j' \, dx$	$= \frac{-6}{5 \, h_{j-1}{}^2}$
3	$: b_j d_{j-1}$	$: \int_{x_{j-1}}^{x_j} \phi_j' \theta_{j-1}' \phi_j' \, dx$	$= \frac{-6}{5 \, h_{j-1}{}^2}$
4a	$: b_j d_j$	$: \int_{x_{j-1}}^{x_j} \phi_j' \theta_j' \phi_j' \, dx$	$= \frac{6}{5 \, h_{j-1}{}^2}$
4b	$: b_j d_j$	$: \int_{x_j}^{x_{j+1}} \phi_j' \theta_j' \phi_j' \, dx$	$= \frac{-6}{5 \, h_j{}^2}$
5	$: b_j d_{j+1}$	$: \int_{x_j}^{x_{j+1}} \phi_j' \theta_{j+1}' \phi_j' \, dx$	$= \frac{6}{5 \, h_j{}^2}$
6	$: b_{j+1} d_j$	$: \int_{x_j}^{x_{j+1}} \phi_{j+1}' \theta_j' \phi_j' \, dx$	$= \frac{6}{5 \, h_j{}^2}$
7	$: b_{j+1} d_{j+1}$	$: \int_{x_j}^{x_{j+1}} \phi_{j+1}' \theta_{j+1}' \phi_j' \, dx$	$= \frac{-6}{5 \, h_j{}^2}$
8	$: c_{j-1} d_{j-1}$	$: \int_{x_{j-1}}^{x_j} \psi_{j-1}' \theta_{j-1}' \phi_j' \, dx$	$= \frac{1}{10 \, h_{j-1}}$
9	$: c_{j-1} d_j$	$: \int_{x_{j-1}}^{x_j} \psi_{j-1}' \theta_j' \phi_j' \, dx$	$= \frac{-1}{10 \, h_{j-1}}$
10	$: c_j d_{j-1}$	$: \int_{x_{j-1}}^{x_j} \psi_j' \theta_{j-1}' \phi_j' \, dx$	$= \frac{1}{10 \, h_{j-1}}$
11a	$: c_j d_j$	$: \int_{x_{j-1}}^{x_j} \psi_j' \theta_j' \phi_j' \, dx$	$= \frac{-1}{10 \, h_{j-1}}$
11b	$: c_j d_j$	$: \int_{x_j}^{x_{j+1}} \psi_j' \theta_j' \phi_j' \, dx$	$= \frac{-1}{10 \, h_j}$
12	$: c_j d_{j+1}$	$: \int_{x_j}^{x_{j+1}} \psi_j' \theta_{j+1}' \phi_j' \, dx$	$= \frac{1}{10 \, h_j}$
13	$: c_{j+1} d_j$	$: \int_{x_j}^{x_{j+1}} \psi_{j+1}' \theta_j' \phi_j' \, dx$	$= \frac{-1}{10 \, h_j}$
14	$: c_{j+1} d_{j+1}$	$: \int_{x_j}^{x_{j+1}} \psi_{j+1}' \theta_{j+1}' \phi_j' \, dx$	$= \frac{1}{10 \, h_j}$

B.5 d3dphi

By substituting $W1 = \phi_j$ in (4.52) the second nonlinear term becomes:

$$\int_0^L \frac{EA}{2} \sum_{i,k,l=0}^{nco} \left(b_i \phi_i' + c_i \psi_i'\right) \left(b_k \phi_k' + c_k \psi_k'\right) \left(b_l \phi_l' + c_l \psi_l'\right) \phi_j' \, dx$$

1 : $b_{j-1}b_{j-1}b_{j-1}$: $\int_{x_{j-1}}^{x_j} \phi'_{j-1}\phi'_{j-1}\phi'_{j-1}\phi'_j \, dx = \frac{-72}{35\, h_{j-1}{}^3}$
2 : $3b_{j-1}b_{j-1}b_j$: $\int_{x_{j-1}}^{x_j} \phi'_{j-1}\phi'_{j-1}\phi'_j\phi'_j \, dx = \frac{72}{35\, h_{j-1}{}^3}$
3 : $3b_{j-1}b_{j-1}c_{j-1}$: $\int_{x_{j-1}}^{x_j} \phi'_{j-1}\phi'_{j-1}\psi'_{j-1}\phi'_j \, dx = \frac{-9}{35\, h_{j-1}{}^2}$
4 : $3b_{j-1}b_{j-1}c_j$: $\int_{x_{j-1}}^{x_j} \phi'_{j-1}\phi'_{j-1}\psi'_j\phi'_j \, dx = \frac{-9}{35\, h_{j-1}{}^2}$
5 : $3b_{j-1}b_jb_j$: $\int_{x_{j-1}}^{x_j} \phi'_{j-1}\phi'_j\phi'_j\phi'_j \, dx = \frac{-72}{35\, h_{j-1}{}^3}$
6 : $6b_{j-1}b_jc_{j-1}$: $\int_{x_{j-1}}^{x_j} \phi'_{j-1}\phi'_j\psi'_{j-1}\phi'_j \, dx = \frac{9}{35\, h_{j-1}{}^2}$
7 : $6b_{j-1}b_jc_j$: $\int_{x_{j-1}}^{x_j} \phi'_{j-1}\phi'_j\psi'_j\phi'_j \, dx = \frac{9}{35\, h_{j-1}{}^2}$
8 : $3b_{j-1}c_{j-1}c_{j-1}$: $\int_{x_{j-1}}^{x_j} \phi'_{j-1}\psi'_{j-1}\psi'_{j-1}\phi'_j \, dx = \frac{-3}{35\, h_{j-1}}$
9 : $6b_{j-1}c_{j-1}c_j$: $\int_{x_{j-1}}^{x_j} \phi'_{j-1}\psi'_{j-1}\psi'_j\phi'_j \, dx = 0$
10 : $3b_{j-1}c_jc_j$: $\int_{x_{j-1}}^{x_j} \phi'_{j-1}\psi'_j\psi'_j\phi'_j \, dx = \frac{-3}{35\, h_{j-1}}$
11a : $b_jb_jb_j$: $\int_{x_{j-1}}^{x_j} \phi'_j\phi'_j\phi'_j\phi'_j \, dx = \frac{72}{35\, h_{j-1}{}^3}$
11b : $b_jb_jb_j$: $\int_{x_j}^{x_{j+1}} \phi'_j\phi'_j\phi'_j\phi'_j \, dx = \frac{72}{35\, h_j{}^3}$
12 : $3b_jb_jb_{j+1}$: $\int_{x_j}^{x_{j+1}} \phi'_j\phi'_j\phi'_{j+1}\phi'_j \, dx = \frac{-72}{35\, h_j{}^3}$
13 : $3b_jb_jc_{j-1}$: $\int_{x_{j-1}}^{x_j} \phi'_j\phi'_j\psi'_{j-1}\phi'_j \, dx = \frac{-9}{35\, h_{j-1}{}^2}$
14a : $3b_jb_jc_j$: $\int_{x_{j-1}}^{x_j} \phi'_j\phi'_j\psi'_j\phi'_j \, dx = \frac{-9}{35\, h_{j-1}{}^2}$
14b : $3b_jb_jc_j$: $\int_{x_j}^{x_{j+1}} \phi'_j\phi'_j\psi'_j\phi'_j \, dx = \frac{9}{35\, h_j{}^2}$
15 : $3b_jb_jc_{j+1}$: $\int_{x_j}^{x_{j+1}} \phi'_j\phi'_j\psi'_{j+1}\phi'_j \, dx = \frac{9}{35\, h_j{}^2}$
16 : $3b_jb_{j+1}b_{j+1}$: $\int_{x_j}^{x_{j+1}} \phi'_j\phi'_{j+1}\phi'_{j+1}\phi'_j \, dx = \frac{72}{35\, h_j{}^3}$
17 : $6b_jb_{j+1}c_j$: $\int_{x_j}^{x_{j+1}} \phi'_j\phi'_{j+1}\psi'_j\phi'_j \, dx = \frac{-9}{35\, h_j{}^2}$
18 : $6b_jb_{j+1}c_{j+1}$: $\int_{x_j}^{x_{j+1}} \phi'_j\phi'_{j+1}\psi'_{j+1}\phi'_j \, dx = \frac{-9}{35\, h_j{}^2}$
19 : $3b_jc_{j-1}c_{j-1}$: $\int_{x_{j-1}}^{x_j} \phi'_j\psi'_{j-1}\psi'_{j-1}\phi'_j \, dx = \frac{3}{35\, h_{j-1}}$
20 : $6b_jc_{j-1}c_j$: $\int_{x_{j-1}}^{x_j} \phi'_j\psi'_{j-1}\psi'_j\phi'_j \, dx = 0$
21a : $3b_jc_jc_j$: $\int_{x_{j-1}}^{x_j} \phi'_j\psi'_j\psi'_j\phi'_j \, dx = \frac{3}{35\, h_{j-1}}$
21b : $3b_jc_jc_j$: $\int_{x_j}^{x_{j+1}} \phi'_j\psi'_j\psi'_j\phi'_j \, dx = \frac{3}{35\, h_j}$
22 : $6b_jc_jc_{j+1}$: $\int_{x_j}^{x_{j+1}} \phi'_j\psi'_j\psi'_{j+1}\phi'_j \, dx = 0$
23 : $3b_jc_{j+1}c_{j+1}$: $\int_{x_j}^{x_{j+1}} \phi'_j\psi'_{j+1}\psi'_{j+1}\phi'_j \, dx = \frac{3}{35\, h_j}$
24 : $b_{j+1}b_{j+1}b_{j+1}$: $\int_{x_j}^{x_{j+1}} \phi'_{j+1}\phi'_{j+1}\phi'_{j+1}\phi'_j \, dx = \frac{-72}{35\, h_j{}^3}$
25 : $3b_{j+1}b_{j+1}c_j$: $\int_{x_j}^{x_{j+1}} \phi'_{j+1}\phi'_{j+1}\psi'_j\phi'_j \, dx = \frac{9}{35\, h_j{}^2}$
26 : $3b_{j+1}b_{j+1}c_{j+1}$: $\int_{x_j}^{x_{j+1}} \phi'_{j+1}\phi'_{j+1}\psi'_{j+1}\phi'_j \, dx = \frac{9}{35\, h_j{}^2}$

27	: $3b_{j+1}c_jc_j$	: $\int_{x_j}^{x_{j+1}} \phi'_{j+1}\psi'_j\psi'_j\phi'_j\,dx$	$= \frac{-3}{35\,h_j}$
28	: $6b_{j+1}c_jc_{j+1}$	: $\int_{x_j}^{x_{j+1}} \phi'_{j+1}\psi'_j\psi'_{j+1}\phi'_j\,dx$	$= 0$
29	: $3b_{j+1}c_{j+1}c_{j+1}$	: $\int_{x_j}^{x_{j+1}} \phi'_{j+1}\psi'_{j+1}\psi'_{j+1}\phi'_j\,dx$	$= \frac{-3}{35\,h_j}$
30	: $c_{j-1}c_{j-1}c_{j-1}$	: $\int_{x_{j-1}}^{x_j} \psi'_{j-1}\psi'_{j-1}\psi'_{j-1}\phi'_j\,dx$	$= \frac{1}{140}$
31	: $3c_{j-1}c_{j-1}c_j$	: $\int_{x_{j-1}}^{x_j} \psi'_{j-1}\psi'_{j-1}\psi'_j\phi'_j\,dx$	$= -\frac{1}{140}$
32	: $3c_{j-1}c_jc_j$	: $\int_{x_{j-1}}^{x_j} \psi'_{j-1}\psi'_j\psi'_j\phi'_j\,dx$	$= -\frac{1}{140}$
33a	: $c_jc_jc_j$	: $\int_{x_{j-1}}^{x_j} \psi'_j\psi'_j\psi'_j\phi'_j\,dx$	$= \frac{1}{140}$
33b	: $c_jc_jc_j$	: $\int_{x_j}^{x_{j+1}} \psi'_j\psi'_j\psi'_j\phi'_j\,dx$	$= -\frac{1}{140}$
34	: $3c_jc_jc_{j+1}$	: $\int_{x_j}^{x_{j+1}} \psi'_j\psi'_j\psi'_{j+1}\phi'_j\,dx$	$= \frac{1}{140}$
35	: $3c_jc_{j+1}c_{j+1}$	: $\int_{x_j}^{x_{j+1}} \psi'_j\psi'_{j+1}\psi'_{j+1}\phi'_j\,dx$	$= \frac{1}{140}$
36	: $c_{j+1}c_{j+1}c_{j+1}$	: $\int_{x_j}^{x_{j+1}} \psi'_{j+1}\psi'_{j+1}\psi'_{j+1}\phi'_j\,dx$	$= -\frac{1}{140}$

B.6 phic

We now substitute $W1 = \phi_j$ in (4.52). The constant term

$$\int_0^L \mu g \phi_j \, dx$$

appears and we calculate the coefficients

$$\begin{aligned} \int_{x_{j-1}}^{x_j} \phi_j dx &= \frac{h_{j-1}}{2} \\ \int_{x_j}^{x_{j+1}} \phi_j dx &= \frac{h_j}{2} \end{aligned}$$

B.7 psi

We now substitute $W1 = \psi_j$ in (4.52). The first term then becomes:

$$
\begin{aligned}
&\int_0^L \sum_{i=0}^{nco} \Big((\mu \ddot{b}_i + \eta_1 \dot{b}_i)\phi_i + (\mu \ddot{c}_i + \eta_1 \dot{c}_i)\psi_i \Big)\, \psi_j \, dx = \\
&(\mu \ddot{b}_{j-1} + \eta_1 \dot{b}_{j-1}) \textstyle\int_{x_{j-1}}^{x_j} \phi_{j-1}\psi_j \, dx + (\mu \ddot{b}_j + \eta_1 \dot{b}_j) \int_{x_{j-1}}^{x_{j+1}} \phi_j \psi_j \, dx + \\
&(\mu \ddot{b}_{j+1} + \eta_1 \dot{b}_{j+1}) \textstyle\int_{x_j}^{x_{j+1}} \phi_{j+1}\psi_j \, dx + \\
&(\mu \ddot{c}_{j-1} + \eta_1 \dot{c}_{j-1}) \textstyle\int_{x_{j-1}}^{x_j} \psi_{j-1}\psi_j \, dx + (\mu \ddot{c}_j + \eta_1 \dot{c}_j) \int_{x_{j-1}}^{x_{j+1}} \psi_j \psi_j \, dx + \\
&(\mu \ddot{c}_{j+1} + \eta_1 \dot{c}_{j+1}) \textstyle\int_{x_j}^{x_{j+1}} \psi_{j+1}\psi_j \, dx,
\end{aligned}
$$

and we calculate the coefficients

$$
\begin{array}{llll}
1 & : \ddot{b}_{j-1}, \dot{b}_{j-1} & : \int_{x_{j-1}}^{x_j} \phi_{j-1}\psi_j dx & = \frac{-13\, {h_{j-1}}^2}{420} \\
2a & : \ddot{b}_j, \dot{b}_j & : \int_{x_{j-1}}^{x_j} \phi_j\psi_j dx & = \frac{-11\, {h_{j-1}}^2}{210} \\
2b & : \ddot{b}_j, \dot{b}_j & : \int_{x_j}^{x_{j+1}} \phi_j\psi_j dx & = \frac{11\, {h_j}^2}{210} \\
3 & : \ddot{b}_{j+1}, \dot{b}_{j+1} & : \int_{x_j}^{x_{j+1}} \phi_{j+1}\psi_j dx & = \frac{13\, {h_j}^2}{420} \\
4 & : \ddot{c}_{j-1}, \dot{c}_{j-1} & : \int_{x_{j-1}}^{x_j} \psi_{j-1}\psi_j dx & = \frac{-{h_{j-1}}^3}{140} \\
5a & : \ddot{c}_j, \dot{c}_j & : \int_{x_{j-1}}^{x_j} \psi_j\psi_j dx & = \frac{{h_{j-1}}^3}{105} \\
5b & : \ddot{c}_j, \dot{c}_j & : \int_{x_j}^{x_{j+1}} \psi_j\psi_j dx & = \frac{{h_j}^3}{105} \\
6 & : \ddot{c}_{j+1}, \dot{c}_{j+1} & : \int_{x_j}^{x_{j+1}} \psi_{j+1}\psi_j dx & = \frac{-{h_j}^3}{140}
\end{array}
$$

B.8 ddpsi

By substituting $W1 = \psi_j$ in (4.52) the second term becomes

$$
\begin{aligned}
&\int_0^L EI \sum_{i=0}^{nco} (b_i \phi_i'' + c_i \psi_i'')\, \psi_j'' \, dx = \\
&EIb_{j-1} \textstyle\int_{x_{j-1}}^{x_j} \phi_{j-1}''\psi_j'' \, dx + EIb_j \int_{x_{j-1}}^{x_{j+1}} \phi_j''\psi_j'' \, dx + \\
&EIb_{j+1} \textstyle\int_{x_j}^{x_{j+1}} \phi_{j+1}''\psi_j'' \, dx + EIc_{j-1} \int_{x_{j-1}}^{x_j} \psi_{j-1}''\psi_j'' \, dx + \\
&EIc_j \textstyle\int_{x_{j-1}}^{x_{j+1}} \psi_j''\psi_j'' \, dx + EIc_{j+1} \int_{x_j}^{x_{j+1}} \psi_{j+1}''\psi_j'' \, dx
\end{aligned}
$$

and we calculate the coefficients

$$\begin{array}{llll}
1 & : b_{j-1} & : \int_{x_{j-1}}^{x_j} \phi''_{j-1}\psi''_j \, dx & = \frac{6}{{h_{j-1}}^2} \\
2a & : b_j & : \int_{x_{j-1}}^{x_j} \phi''_j\psi''_j \, dx & = \frac{-6}{{h_{j-1}}^2} \\
2b & : b_j & : \int_{x_j}^{x_{j+1}} \phi''_j\psi''_j \, dx & = \frac{6}{{h_j}^2} \\
3 & : b_{j+1} & : \int_{x_j}^{x_{j+1}} \phi''_{j+1}\psi''_j \, dx & = \frac{-6}{{h_j}^2} \\
4 & : c_{j-1} & : \int_{x_{j-1}}^{x_j} \psi''_{j-1}\psi''_j \, dx & = \frac{2}{h_{j-1}} \\
5a & : c_j & : \int_{x_{j-1}}^{x_j} \psi''_j\psi''_j \, dx & = \frac{4}{h_{j-1}} \\
5b & : c_j & : \int_{x_j}^{x_{j+1}} \psi''_j\psi''_j \, dx & = \frac{4}{h_j} \\
6 & : c_{j+1} & : \int_{x_j}^{x_{j+1}} \psi''_{j+1}\psi''_j \, dx & = \frac{2}{h_j}
\end{array}$$

B.9 dpsi

By substituting $W1 = \psi_j$ in (4.52) the third term becomes

$$\begin{array}{l}
\int_0^L P0 \sum_{i=0}^{nco} \left(b_i\phi'_i + c_i\psi'_i\right)\psi'_j \, dx = \\
P0b_{j-1} \int_{x_{j-1}}^{x_j} \phi'_{j-1}\psi'_j \, dx + P0b_j \int_{x_{j-1}}^{x_{j+1}} \phi'_j\psi'_j \, dx + \\
P0b_{j+1} \int_{x_j}^{x_{j+1}} \phi'_{j+1}\psi'_j \, dx + P0c_{j-1} \int_{x_{j-1}}^{x_j} \psi'_{j-1}\psi'_j \, dx + \\
P0c_j \int_{x_{j-1}}^{x_{j+1}} \psi'_j\psi'_j \, dx + P0c_{j+1} \int_{x_j}^{x_{j+1}} \psi'_{j+1}\psi'_j \, dx
\end{array}$$

and the coefficients become

$$\begin{array}{llll}
1 & : b_{j-1} & : \int_{x_{j-1}}^{x_j} \phi'_{j-1}\psi'_j \, dx & = \frac{1}{10} \\
2a & : b_j & : \int_{x_{j-1}}^{x_j} \phi'_j\psi'_j \, dx & = -\frac{1}{10} \\
2b & : b_j & : \int_{x_j}^{x_{j+1}} \phi'_j\psi'_j \, dx & = \frac{1}{10} \\
3 & : b_{j+1} & : \int_{x_j}^{x_{j+1}} \phi'_{j+1}\psi'_j \, dx & = -\frac{1}{10} \\
4 & : c_{j-1} & : \int_{x_{j-1}}^{x_j} \psi'_{j-1}\psi'_j \, dx & = \frac{-h_{j-1}}{30} \\
5a & : c_j & : \int_{x_{j-1}}^{x_j} \psi'_j\psi'_j \, dx & = \frac{2\,h_{j-1}}{15} \\
5b & : c_j & : \int_{x_j}^{x_{j+1}} \psi'_j\psi'_j \, dx & = \frac{2\,h_j}{15} \\
6 & : c_{j+1} & : \int_{x_j}^{x_{j+1}} \psi'_{j+1}\psi'_j \, dx & = \frac{-h_j}{30}
\end{array}$$

B.10 dvupsi

When we substitute $W1 = \psi_j$ in (4.52) the first nonlinear term becomes

$$\int_0^L EA \sum_{i,k=0}^{nco} \left(b_i\phi_i' + c_i\psi_i'\right)\left(d_k\theta_k'\right)\psi_j'\,dx$$

for which we calculate the coefficients

1	: $b_{j-1}d_{j-1}$	: $\int_{x_{j-1}}^{x_j} \phi_{j-1}'\theta_{j-1}'\psi_j'\,dx$	$= \frac{-1}{10\,h_{j-1}}$
2	: $b_{j-1}d_j$	: $\int_{x_{j-1}}^{x_j} \phi_{j-1}'\theta_j'\psi_j'\,dx$	$= \frac{1}{10\,h_{j-1}}$
3	: b_jd_{j-1}	: $\int_{x_{j-1}}^{x_j} \phi_j'\theta_{j-1}'\psi_j'\,dx$	$= \frac{1}{10\,h_{j-1}}$
$4a$	: b_jd_j	: $\int_{x_{j-1}}^{x_j} \phi_j'\theta_j'\psi_j'\,dx$	$= \frac{-1}{10\,h_{j-1}}$
$4b$	: b_jd_j	: $\int_{x_j}^{x_{j+1}} \phi_j'\theta_j'\psi_j'\,dx$	$= \frac{-1}{10\,h_j}$
5	: b_jd_{j+1}	: $\int_{x_j}^{x_{j+1}} \phi_j'\theta_{j+1}'\psi_j'\,dx$	$= \frac{1}{10\,h_j}$
6	: $b_{j+1}d_j$	: $\int_{x_j}^{x_{j+1}} \phi_{j+1}'\theta_j'\psi_j'\,dx$	$= \frac{1}{10\,h_j}$
7	: $b_{j+1}d_{j+1}$	: $\int_{x_j}^{x_{j+1}} \phi_{j+1}'\theta_{j+1}'\psi_j'\,dx$	$= \frac{-1}{10\,h_j}$
8	: $c_{j-1}d_{j-1}$	: $\int_{x_{j-1}}^{x_j} \psi_{j-1}'\theta_{j-1}'\psi_j'\,dx$	$= \frac{1}{30}$
9	: $c_{j-1}d_j$	: $\int_{x_{j-1}}^{x_j} \psi_{j-1}'\theta_j'\psi_j'\,dx$	$= -\frac{1}{30}$
10	: c_jd_{j-1}	: $\int_{x_{j-1}}^{x_j} \psi_j'\theta_{j-1}'\psi_j'\,dx$	$= -\frac{2}{15}$
$11a$	: c_jd_j	: $\int_{x_{j-1}}^{x_j} \psi_j'\theta_j'\psi_j'\,dx$	$= \frac{2}{15}$
$11b$	: c_jd_j	: $\int_{x_j}^{x_{j+1}} \psi_j'\theta_j'\psi_j'\,dx$	$= -\frac{2}{15}$
12	: c_jd_{j+1}	: $\int_{x_j}^{x_{j+1}} \psi_j'\theta_{j+1}'\psi_j'\,dx$	$= \frac{2}{15}$
13	: $c_{j+1}d_j$	: $\int_{x_j}^{x_{j+1}} \psi_{j+1}'\theta_j'\psi_j'\,dx$	$= \frac{1}{30}$
14	: $c_{j+1}d_{j+1}$	: $\int_{x_j}^{x_{j+1}} \psi_{j+1}'\theta_{j+1}'\psi_j'\,dx$	$= -\frac{1}{30}$

B.11 d3dpsi

By substituting $W1 = \psi_j$ in (4.52) the second nonlinear term becomes:

$$\int_0^L \frac{EA}{2} \sum_{i,k,l=0}^{nco} \left(b_i\phi_i' + c_i\psi_i'\right)\left(b_k\phi_k' + c_k\psi_k'\right)\left(b_l\phi_l' + c_l\psi_l'\right)\psi_j'\,dx$$

and we therefore calculate the coefficients

1 : $b_{j-1}b_{j-1}b_{j-1}$: $\int_{x_{j-1}}^{x_j} \phi'_{j-1}\phi'_{j-1}\phi'_{j-1}\psi'_j \, dx = \frac{9}{35\, h_{j-1}{}^2}$

2 : $3b_{j-1}b_{j-1}b_j$: $\int_{x_{j-1}}^{x_j} \phi'_{j-1}\phi'_{j-1}\phi'_j\psi'_j \, dx = \frac{-9}{35\, h_{j-1}{}^2}$

3 : $3b_{j-1}b_{j-1}c_{j-1}$: $\int_{x_{j-1}}^{x_j} \phi'_{j-1}\phi'_{j-1}\psi'_{j-1}\psi'_j \, dx = 0$

4 : $3b_{j-1}b_{j-1}c_j$: $\int_{x_{j-1}}^{x_j} \phi'_{j-1}\phi'_{j-1}\psi'_j\psi'_j \, dx = \frac{3}{35\, h_{j-1}}$

5 : $3b_{j-1}b_jb_j$: $\int_{x_{j-1}}^{x_j} \phi'_{j-1}\phi'_j\phi'_j\psi'_j \, dx = \frac{9}{35\, h_{j-1}{}^2}$

6 : $6b_{j-1}b_jc_{j-1}$: $\int_{x_{j-1}}^{x_j} \phi'_{j-1}\phi'_j\psi'_{j-1}\psi'_j \, dx = 0$

7 : $6b_{j-1}b_jc_j$: $\int_{x_{j-1}}^{x_j} \phi'_{j-1}\phi'_j\psi'_j\psi'_j \, dx = \frac{-3}{35\, h_{j-1}}$

8 : $3b_{j-1}c_{j-1}c_{j-1}$: $\int_{x_{j-1}}^{x_j} \phi'_{j-1}\psi'_{j-1}\psi'_{j-1}\psi'_j \, dx = \frac{1}{140}$

9 : $6b_{j-1}c_{j-1}c_j$: $\int_{x_{j-1}}^{x_j} \phi'_{j-1}\psi'_{j-1}\psi'_j\psi'_j \, dx = \frac{1}{140}$

10 : $3b_{j-1}c_jc_j$: $\int_{x_{j-1}}^{x_j} \phi'_{j-1}\psi'_j\psi'_j\psi'_j \, dx = -\frac{1}{140}$

11*a* : $b_jb_jb_j$: $\int_{x_{j-1}}^{x_j} \phi'_j\phi'_j\phi'_j\psi'_j \, dx = \frac{-9}{35\, h_{j-1}{}^2}$

11*b* : $b_jb_jb_j$: $\int_{x_j}^{x_{j+1}} \phi'_j\phi'_j\phi'_j\psi'_j \, dx = \frac{9}{35\, h_j{}^2}$

12 : $3b_jb_jb_{j+1}$: $\int_{x_j}^{x_{j+1}} \phi'_j\phi'_j\phi'_{j+1}\psi'_j \, dx = \frac{-9}{35\, h_j{}^2}$

13 : $3b_jb_jc_{j-1}$: $\int_{x_{j-1}}^{x_j} \phi'_j\phi'_j\psi'_{j-1}\psi'_j \, dx = 0$

14*a* : $3b_jb_jc_j$: $\int_{x_{j-1}}^{x_j} \phi'_j\phi'_j\psi'_j\psi'_j \, dx = \frac{3}{35\, h_{j-1}}$

14*b* : $3b_jb_jc_j$: $\int_{x_j}^{x_{j+1}} \phi'_j\phi'_j\psi'_j\psi'_j \, dx = \frac{3}{35\, h_j}$

15 : $3b_jb_jc_{j+1}$: $\int_{x_j}^{x_{j+1}} \phi'_j\phi'_j\psi'_{j+1}\psi'_j \, dx = 0$

16 : $3b_jb_{j+1}b_{j+1}$: $\int_{x_j}^{x_{j+1}} \phi'_j\phi'_{j+1}\phi'_{j+1}\psi'_j \, dx = \frac{9}{35\, h_j{}^2}$

17 : $6b_jb_{j+1}c_j$: $\int_{x_j}^{x_{j+1}} \phi'_j\phi'_{j+1}\psi'_j\psi'_j \, dx = \frac{-3}{35\, h_j}$

18 : $6b_jb_{j+1}c_{j+1}$: $\int_{x_j}^{x_{j+1}} \phi'_j\phi'_{j+1}\psi'_{j+1}\psi'_j \, dx = 0$

19 : $3b_jc_{j-1}c_{j-1}$: $\int_{x_{j-1}}^{x_j} \phi'_j\psi'_{j-1}\psi'_{j-1}\psi'_j \, dx = -\frac{1}{140}$

20 : $6b_jc_{j-1}c_j$: $\int_{x_{j-1}}^{x_j} \phi'_j\psi'_{j-1}\psi'_j\psi'_j \, dx = -\frac{1}{140}$

21*a* : $3b_jc_jc_j$: $\int_{x_{j-1}}^{x_j} \phi'_j\psi'_j\psi'_j\psi'_j \, dx = \frac{1}{140}$

21*b* : $3b_jc_jc_j$: $\int_{x_j}^{x_{j+1}} \phi'_j\psi'_j\psi'_j\psi'_j \, dx = -\frac{1}{140}$

22 : $6b_jc_jc_{j+1}$: $\int_{x_j}^{x_{j+1}} \phi'_j\psi'_j\psi'_{j+1}\psi'_j \, dx = \frac{1}{140}$

23 : $3b_jc_{j+1}c_{j+1}$: $\int_{x_j}^{x_{j+1}} \phi'_j\psi'_{j+1}\psi'_{j+1}\psi'_j \, dx = \frac{1}{140}$

24 : $b_{j+1}b_{j+1}b_{j+1}$: $\int_{x_j}^{x_{j+1}} \phi'_{j+1}\phi'_{j+1}\phi'_{j+1}\psi'_j \, dx = \frac{-9}{35\, h_j{}^2}$

25 : $3b_{j+1}b_{j+1}c_j$: $\int_{x_j}^{x_{j+1}} \phi'_{j+1}\phi'_{j+1}\psi'_j\psi'_j \, dx = \frac{3}{35\, h_j}$

26 : $3b_{j+1}b_{j+1}c_{j+1}$: $\int_{x_j}^{x_{j+1}} \phi'_{j+1}\phi'_{j+1}\psi'_{j+1}\psi'_j \, dx = 0$

27	$: 3b_{j+1}c_jc_j$	$: \int_{x_j}^{x_{j+1}} \phi'_{j+1}\psi'_j\psi'_j\psi'_j\, dx$	$= \frac{1}{140}$
28	$: 6b_{j+1}c_jc_{j+1}$	$: \int_{x_j}^{x_{j+1}} \phi'_{j+1}\psi'_j\psi'_{j+1}\psi'_j\, dx$	$= -\frac{1}{140}$
29	$: 3b_{j+1}c_{j+1}c_{j+1}$	$: \int_{x_j}^{x_{j+1}} \phi'_{j+1}\psi'_{j+1}\psi'_{j+1}\psi'_j\, dx$	$= -\frac{1}{140}$
30	$: c_{j-1}c_{j-1}c_{j-1}$	$: \int_{x_{j-1}}^{x_j} \psi'_{j-1}\psi'_{j-1}\psi'_{j-1}\psi'_j\, dx$	$= \frac{-h_{j-1}}{140}$
31	$: 3c_{j-1}c_{j-1}c_j$	$: \int_{x_{j-1}}^{x_j} \psi'_{j-1}\psi'_{j-1}\psi'_j\psi'_j\, dx$	$= \frac{h_{j-1}}{210}$
32	$: 3c_{j-1}c_jc_j$	$: \int_{x_{j-1}}^{x_j} \psi'_{j-1}\psi'_j\psi'_j\psi'_j\, dx$	$= \frac{-h_{j-1}}{140}$
33a	$: c_jc_jc_j$	$: \int_{x_{j-1}}^{x_j} \psi'_j\psi'_j\psi'_j\psi'_j\, dx$	$= \frac{2\,h_{j-1}}{35}$
33b	$: c_jc_jc_j$	$: \int_{x_j}^{x_{j+1}} \psi'_j\psi'_j\psi'_j\psi'_j\, dx$	$= \frac{2\,h_j}{35}$
34	$: 3c_jc_jc_{j+1}$	$: \int_{x_j}^{x_{j+1}} \psi'_j\psi'_j\psi'_{j+1}\psi'_j\, dx$	$= \frac{-h_j}{140}$
35	$: 3c_jc_{j+1}c_{j+1}$	$: \int_{x_j}^{x_{j+1}} \psi'_j\psi'_{j+1}\psi'_{j+1}\psi'_j\, dx$	$= \frac{h_j}{210}$
36	$: c_{j+1}c_{j+1}c_{j+1}$	$: \int_{x_j}^{x_{j+1}} \psi'_{j+1}\psi'_{j+1}\psi'_{j+1}\psi'_j\, dx$	$= \frac{-h_j}{140}$

B.12 psic

We now substitute $W1 = \psi_j$ in (4.52). The constant term

$$\int_0^L \mu g \psi_j \, dx$$

appears and we calculate the coefficients

$$\begin{aligned} \int_{x_{j-1}}^{x_j} \psi_j dx &= \frac{-{h_{j-1}}^2}{12} \\ \int_{x_j}^{x_{j+1}} \psi_j dx &= \frac{{h_j}^2}{12} \end{aligned}$$

B.13 theta

Substituting $W2 = \theta_j$ in the second equation in (4.52) first yields the term:

$$\begin{aligned} &\int_0^L \sum_{i=0}^{nco} \left((\mu\ddot{d}_i + \eta_2\dot{d}_i)\theta_i \right) \theta_j \, dx = \\ &(\mu\ddot{d}_{j-1} + \eta_2\dot{d}_{j-1}) \int_{x_{j-1}}^{x_j} \theta_{j-1}\theta_j \, dx + (\mu\ddot{d}_j + \eta_2\dot{d}_j) \int_{x_{j-1}}^{x_{j+1}} \theta_j\theta_j \, dx + \\ &(\mu\ddot{d}_{j+1} + \eta_2\dot{d}_{j+1}) \int_{x_j}^{x_{j+1}} \theta_{j+1}\theta_j \, dx \end{aligned}$$

$$\begin{array}{llll}
1 & : \ddot{d}_{j-1}, \dot{d}_{j-1} & : \int_{x_{j-1}}^{x_j} \theta_{j-1}\theta_j dx & = \frac{h_{j-1}}{6} \\
2a & : \ddot{d}_j, \dot{d}_j & : \int_{x_{j-1}}^{x_j} \theta_j\theta_j dx & = \frac{h_{j-1}}{3} \\
2b & : \ddot{d}_j, \dot{d}_j & : \int_{x_j}^{x_{j+1}} \theta_j\theta_j dx & = \frac{h_j}{3} \\
3 & : \ddot{d}_{j+1}, \dot{d}_{j+1} & : \int_{x_j}^{x_{j+1}} \theta_{j+1}\theta_j dx & = \frac{h_j}{6}
\end{array}$$

B.14 dtheta

The second term in (4.52) by the substituting $W2 = \theta_j$ yields the term

$$\begin{array}{l}
\int_0^L EA \sum_{i=0}^{nco} d_i \theta_i' \theta_j' \, dx = \\
EAb_{j-1} \int_{x_{j-1}}^{x_j} \theta_{j-1}' \theta_j' \, dx + EAb_j \int_{x_{j-1}}^{x_{j+1}} \theta_j' \theta_j' \, dx + \\
EAb_{j+1} \int_{x_j}^{x_{j+1}} \theta_{j+1}' \theta_j' \, dx
\end{array}$$

and we calculate the coefficients

$$\begin{array}{llll}
1 & : d_{j-1} & : \int_{x_{j-1}}^{x_j} \theta_{j-1}' \theta_j' \, dx & = -\frac{1}{h_{j-1}} \\
2a & : d_j & : \int_{x_{j-1}}^{x_j} \theta_j' \theta_j' \, dx & = \frac{1}{h_{j-1}} \\
2b & : d_j & : \int_{x_j}^{x_{j+1}} \theta_j' \theta_j' \, dx & = \frac{1}{h_j} \\
3 & : d_{j+1} & : \int_{x_j}^{x_{j+1}} \theta_{j+1}' \theta_j' \, dx & = -\frac{1}{h_j}
\end{array}$$

B.15 dv2theta

Finally the last term (the nonlinear term) in the second equation in (4.52) by the substitution $W2 = \theta_j$ becomes

$$\int_0^L \frac{EA}{2} \sum_{i,k=0}^{nco} \left(b_i \phi_i' + c_i \psi_i'\right) \left(b_k \phi_k' + c_k \psi_k'\right) \theta_j' \, dx$$

and we calculate the coefficients

$$\begin{array}{llll}
1 & : b_{j-1}b_{j-1} & : \int_{x_{j-1}}^{x_j} \phi'_{j-1}\phi'_{j-1}\theta'_j\,dx & = \frac{6}{5\,{h_{j-1}}^2} \\
2 & : 2b_{j-1}b_j & : \int_{x_{j-1}}^{x_j} \phi'_{j-1}\phi'_j\theta'_j\,dx & = \frac{-6}{5\,{h_{j-1}}^2} \\
3 & : 2b_{j-1}c_{j-1} & : \int_{x_{j-1}}^{x_j} \phi'_{j-1}\psi'_{j-1}\theta'_j\,dx & = \frac{1}{10\,h_{j-1}} \\
4 & : 2b_{j-1}c_j & : \int_{x_{j-1}}^{x_j} \phi'_{j-1}\psi'_j\theta'_j\,dx & = \frac{1}{10\,h_{j-1}} \\
5a & : b_jb_j & : \int_{x_{j-1}}^{x_j} \phi'_j\phi'_j\theta'_j\,dx & = \frac{6}{5\,{h_{j-1}}^2} \\
5b & : b_jb_j & : \int_{x_j}^{x_{j+1}} \phi'_j\phi'_j\theta'_j\,dx & = \frac{-6}{5\,{h_j}^2} \\
6 & : 2b_jb_{j+1} & : \int_{x_j}^{x_{j+1}} \phi'_j\phi'_{j+1}\theta'_j\,dx & = \frac{6}{5\,{h_j}^2} \\
7 & : 2b_jc_{j-1} & : \int_{x_{j-1}}^{x_j} \phi'_j\psi'_{j-1}\theta'_j\,dx & = \frac{-1}{10\,h_{j-1}} \\
8a & : 2b_jc_j & : \int_{x_{j-1}}^{x_j} \phi'_j\psi'_j\theta'_j\,dx & = \frac{-1}{10\,h_{j-1}} \\
8b & : 2b_jc_j & : \int_{x_j}^{x_{j+1}} \phi'_j\psi'_j\theta'_j\,dx & = \frac{-1}{10\,h_j} \\
9 & : 2b_jc_{j+1} & : \int_{x_j}^{x_{j+1}} \phi'_j\psi'_{j+1}\theta'_j\,dx & = \frac{-1}{10\,h_j} \\
10 & : b_{j+1}b_{j+1} & : \int_{x_j}^{x_{j+1}} \phi'_{j+1}\phi'_{j+1}\theta'_j\,dx & = \frac{-6}{5\,{h_j}^2} \\
11 & : 2b_{j+1}c_j & : \int_{x_j}^{x_{j+1}} \phi'_{j+1}\psi'_j\theta'_j\,dx & = \frac{1}{10\,h_j} \\
12 & : 2b_{j+1}c_{j+1} & : \int_{x_j}^{x_{j+1}} \phi'_{j+1}\psi'_{j+1}\theta'_j\,dx & = \frac{1}{10\,h_j} \\
13 & : c_{j-1}c_{j-1} & : \int_{x_{j-1}}^{x_j} \psi'_{j-1}\psi'_{j-1}\theta'_j\,dx & = \frac{2}{15} \\
14 & : 2c_{j-1}c_j & : \int_{x_{j-1}}^{x_j} \psi'_{j-1}\psi'_j\theta'_j\,dx & = -\frac{1}{30} \\
15a & : c_jc_j & : \int_{x_{j-1}}^{x_j} \psi'_j\psi'_j\theta'_j\,dx & = \frac{2}{15} \\
15b & : c_jc_j & : \int_{x_j}^{x_{j+1}} \psi'_j\psi'_j\theta'_j\,dx & = -\frac{2}{15} \\
16 & : 2c_jc_{j+1} & : \int_{x_j}^{x_{j+1}} \psi'_j\psi'_{j+1}\theta'_j\,dx & = \frac{1}{30} \\
17 & : c_{j+1}c_{j+1} & : \int_{x_j}^{x_{j+1}} \psi'_{j+1}\psi'_{j+1}\theta'_j\,dx & = -\frac{2}{15}
\end{array}$$